



University of Kentucky
UKnowledge

Theses and Dissertations--Chemical and
Materials Engineering

Chemical and Materials Engineering

2015

INHALABLE NANOCOMPOSITES AND ANTICANCER AGENTS FOR CANCER THERAPY

Nathanael A. Stocke
University of Kentucky, Nas587@gmail.com

[Right click to open a feedback form in a new tab to let us know how this document benefits you.](#)

Recommended Citation

Stocke, Nathanael A., "INHALABLE NANOCOMPOSITES AND ANTICANCER AGENTS FOR CANCER THERAPY" (2015). *Theses and Dissertations--Chemical and Materials Engineering*. 55.
https://uknowledge.uky.edu/cme_etds/55

This Doctoral Dissertation is brought to you for free and open access by the Chemical and Materials Engineering at UKnowledge. It has been accepted for inclusion in Theses and Dissertations--Chemical and Materials Engineering by an authorized administrator of UKnowledge. For more information, please contact UKnowledge@lsv.uky.edu.

STUDENT AGREEMENT:

I represent that my thesis or dissertation and abstract are my original work. Proper attribution has been given to all outside sources. I understand that I am solely responsible for obtaining any needed copyright permissions. I have obtained needed written permission statement(s) from the owner(s) of each third-party copyrighted matter to be included in my work, allowing electronic distribution (if such use is not permitted by the fair use doctrine) which will be submitted to UKnowledge as Additional File.

I hereby grant to The University of Kentucky and its agents the irrevocable, non-exclusive, and royalty-free license to archive and make accessible my work in whole or in part in all forms of media, now or hereafter known. I agree that the document mentioned above may be made available immediately for worldwide access unless an embargo applies.

I retain all other ownership rights to the copyright of my work. I also retain the right to use in future works (such as articles or books) all or part of my work. I understand that I am free to register the copyright to my work.

REVIEW, APPROVAL AND ACCEPTANCE

The document mentioned above has been reviewed and accepted by the student's advisor, on behalf of the advisory committee, and by the Director of Graduate Studies (DGS), on behalf of the program; we verify that this is the final, approved version of the student's thesis including all changes required by the advisory committee. The undersigned agree to abide by the statements above.

Nathanael A. Stocke, Student

Dr. J. Zach Hilt, Major Professor

Dr. Thomas Dziubla, Director of Graduate Studies

INHALABLE NANOCOMPOSITES AND ANTICANCER AGENTS FOR CANCER
THERAPY

DISSERTATION

A dissertation submitted in partial fulfillment of the
requirements for the degree of Doctor of Philosophy in the
College of Engineering
at the University of Kentucky

By
Nathanael Aaron Stocke

Lexington, Kentucky

Director: Dr. J. Zach Hilt, Associate Professor of Chemical & Materials Engineering

Lexington, Kentucky

2015

Copyright © Nathanael Aaron Stocke 2015

ABSTRACT OF DISSERTATION

INHALABLE NANOCOMPOSITES AND ANTICANCER AGENTS FOR CANCER THERAPY

Cancer is designated as the leading cause of mortality worldwide and lung cancer is responsible for nearly 30% of all cancer related deaths. Over the last few decades mortality rates have only marginally increased and rates of recurrence remain high. These factors, among others, suggest the need for more innovative treatment modalities in lung cancer therapy. Targeted pulmonary delivery is well established for treating pulmonary diseases such as asthma and provides a promising platform for lung cancer therapy. Increasing local deposition of anticancer agents (ACAs) and reducing systemic exposure of these toxic moieties could lead to better therapeutic outcomes and higher quality of life for lung cancer patients receiving such harsh chemotherapy regimens. In this work, a novel lung cancer treatment modality is presented wherein ACAs are incorporated into inhalable dry powder composites for targeted delivery to the pulmonary tract. Additionally, nanoparticles were added to inhalable composites to increase the therapeutic potential of these unique materials.

A variety of dry powder composites were formulated via spray drying and the physicochemical properties of the resulting systems were characterized. Additionally, the performance of the cargo incorporated into these composites was evaluated in order to insure the activity of the components after release from the inhalable dry powders. The aerodynamic performance of the dry powder systems was evaluated with the Next Generation Impactor® to determine if these materials were suitable for inhalation purposes.

Iron oxide (Fe_3O_4) magnetic nanoparticles were synthesized and incorporated into dry powders to examine the feasibility of administering these materials to the lungs for remotely actuated hyperthermia. Remote heating studies were performed on the nanoparticles released from these composites using a custom Taylor Winfield® alternating magnetic field source, and *in vitro* hyperthermia studies were performed using advanced multicellular spheroid cell culture models. These studies elicited the

effectiveness of these systems on physiologically relevant models. In addition to the iron oxide composites, dry powders were formulated with two common ACAs, cisplatin and erlotinib, for inhalable chemotherapy. The activity of the drugs released from these composites was evaluated on the human pulmonary lung cancer cell lines A549 and H358 and compared with the free form of the drugs in order to evaluate the effectiveness of these therapies. Finally, responsive hydrogel nanoparticles (HNPs) that contain the ability to respond to environmental changes in pH were synthesized and evaluated as responsive drug carriers. The response of these particles to pH was evaluated and their stability was examined before and after inclusion into dry powder composites. Overall, inhalable dry powder nanocomposites are promising materials for innovative lung cancer treatment modalities and have the potential to provide a safer and more effective option for addressing this devastating disease.

KEYWORDS: Lung cancer, pulmonary delivery, nanoparticles, hyperthermia, anticancer agents

Nathanael Aaron Stocke
Student's Signature

April 30, 2015
Date

INHALABLE NANOCOMPOSITES FOR THE TREATMENT OF LUNG
CANCER

By

Nathanael Aaron Stocke

Dr. J. Zach Hilt
Director of Dissertation

Dr. Thomas Dziubla
Director of Graduate Studies

April, 2015

Dedicated to my loving grandparents, John and Agnus Mitchell

ACKNOWLEDGEMENTS

This dissertation would not have been possible without guidance and encouragement from multiple individuals in my life and I am beyond thankful for those who have been a part of this journey. To start, I would like to thank my advisor, Dr. J. Zach Hilt for all of his continuous support. Throughout my time spent here at the University of Kentucky, I have sought Dr. Hilt's counsel countless times. While most of these encounters have revolved around science, his influence has reached far beyond simply molding my scientific intellect; his character and integrity have inspired me to pursue professionalism at the highest level, while showing me that it is possible to be a committed husband and loving father though it all. Truthfully, I would not be where I am today if not for the invaluable teaching, mentoring, and advising I received from Dr. Hilt.

Secondly, I would like to express gratitude to my clinical advisor Dr. Susanne Arnold, MD. During my first year as a graduate student, I reached out to Dr. Arnold to obtain her advice regarding the direction of my research project. She generously gave her time and counsel that proved to be invaluable in years to come. Thereafter, Dr. Arnold accepted my invitation to become the clinical advisor for my project with the National Cancer Institute. Her contributions shaped many fundamental aspects of my projects, and I am grateful for her expert advice and unapologetic candidness during our encounters.

To the other members of my committee, Dr. Dziubla, Dr. Anderson, and Dr. Upreti, I am grateful for their input over the past few years. I have approached each of

these individuals at varying times throughout my graduate work. Each of them responded as if I am one of their own graduate students, with a willing and supportive approach.

Additionally, I would like to express appreciation to my fellow graduate students and lab mates, without whom this work would have been impossible. Specifically, I would like to thank members of the Hilt lab group, both past and present: Ashley Lewis, Samantha Meenach, Robert Wydra, Anastasia Hauser, Angela Gutierrez, Shuo Tang, Rohit Bhandari, Trang Mai. Additionally, I would like to thank the following graduate students from other lab groups: Daniel Schlipfghd, Jenn Fisher, Andrew Vasilakes, David Cochran, and Jacob Lilly. Each of these individuals have played an influential part in facilitating my progress through graduate school, regardless of whether it be an tedious scientific conversation or an enjoyable social activity.

I would also like to specifically thank Robert Wydra for the thousands of times I asked for his advice and the hundreds of times he pleasantly responded. Truthfully, Rob started his graduate work the year before me and has been an irreplaceable resource through this experience. More than just a fellow graduate student, Rob has been an ongoing friend and I will always cherish the time we spent together becoming young scientists.

Lastly, I would be remiss if I failed to mention my friends and family who played such an important role, albeit unnoticed by many, in my progression throughout the last several years. They have been the rock that I stand on and their encouragement that has helped me persevere. Specifically, my parents, Richard and Susan, my brothers, Jonathan and Eric, my sisters Sarah and Madeline, and my closest friends have shown

love and support throughout my time spent here at the University of Kentucky and I owe this entire dissertation to them.

When I started my graduate work, I had a strong desire to be part of a research project involving lung cancer, as my grandfather's passing from this debilitating disease had a marked influence on my life. Beyond anything else, I wanted my family to be proud of my research and their support throughout my graduate work has confirmed this each and every day.

In closing, I would like to say that what you get by achieving your goals is not as important as what you become by achieving your goals. Thank you all for individually being a part of what this dissertation and I have become.

Table of Contents

ACKNOWLEDGEMENTS	iii
Table of Contents	vi
List of Tables	xi
List of Figures	xii
Chapter 1 Introduction	1
1.1 Objectives	3
Chapter 2 Pulmonary Delivery for Targeted Lung Cancer Therapy	5
2.1 Types of Lung Cancer	5
2.2 Current Non-Surgical Treatments of NSCLC	7
2.2.1 Treatment options based on pathological stage	8
2.2.2 Personalized treatment of NSCLC patients	10
2.3 Pulmonary Delivery	12
2.3.1 Pulmonary delivery for lung cancer treatment.....	14
2.3.2 Dry powders for inhalation	15
2.4 Hydrogels Nanoparticles	17
2.5 Iron Oxide (Fe ₃ O ₄) magnetic nanoparticles	19
2.6 Magnetic nanoparticles and pulmonary delivery	21
2.7 Mucus Barriers and particle transport	28
Chapter 3 Formulation and Characterization of Inhalable Magnetic Nanocomposite Microparticles (MnMs) for Targeted Pulmonary Delivery via Spray Drying.....	34
3.0 Abstract	34
3.1 Introduction	35
3.2 Material and methods	39
3.2.1 Materials	39
3.2.2 Synthesis of iron oxide magnetic nanoparticles (MNPs).....	40
3.2.3 Formulation of magnetic nanocomposite microparticles (MnMs) with spray drying	40
3.2.4 Electron microscopy	41

3.2.5 Thermal gravimetric analysis (TGA).....	42
3.2.6 Karl Fischer titration.....	43
3.2.7 Differential scanning calorimetry (DSC).....	43
3.2.8 X-ray powder diffraction (XRPD).....	44
3.2.9 Particle size analysis.....	44
3.2.10 In vitro aerosol dispersion performance with the Next Generation Impactor™ (NGI™).....	45
3.2.11 Alternating magnetic field (AMF) Heating studies.....	46
3.2.12 Cytotoxicity tests.....	47
3.2.13 Statistics.....	48
3.3 Results and Discussion.....	48
3.3.1 Physiochemical characterization.....	48
3.3.2 Aerosol performance of MnMs.....	54
3.3.3 AMF heating of MNPs released from MnMs.....	57
3.3.4 In vitro cytotoxicity of MnMs exposed to human lung cell lines.....	58
3.4 Conclusions.....	60
Chapter 4 Remote controlled thermal therapy with magnetic nanocomposite microparticles induces cell death in triple negative breast cancer micrometastatic tumor tissue analogs61	
4.1 Introduction.....	61
4.2 Material and methods.....	63
4.2.1 Materials.....	63
4.2.2 Formulation of inhalable magnetic nanocomposite microparticles....	63
4.2.3 Formation of triple negative breast cancer micrometastatic tumor tissue analogs (TM analogs).....	64
4.2.4 MNP-treatment of TM analogs.....	65
4.2.5 Remotely actuated hyperthermia using a custom alternating magnetic field (AM).....	65
4.2.6 Fluorescent imaging on TM analogs.....	66
4.2.7 Quantification of cell death using Sytox.....	67

4.2.8 Prussian blue staining for iron	67
4.2.9 Transmission electron microscopy (TEM) on TM analogs	68
4.3 Results and Discussion.....	69
4.4 Conclusions	80
Chapter 5 Formulation and Characterization of Inhalable Anticancer Agents for Targeted Pulmonary Delivery via Spray Drying	81
5.0 Abstract	81
5.1 Introduction	82
5.2 Materials and Methods	85
5.2.1 Materials	85
5.2.2 Inhalable ACA systems.....	86
5.2.3 Spray Drying.....	87
5.2.4 Scanning Electron Microscopy (SEM) on Inhalable Powders	88
5.2.5 Determination of ACA loading in spray dried composites.....	88
5.2.6 Differential scanning calorimetry (DSC).....	89
5.2.7 X-ray powder diffraction (XRPD).....	90
5.2.8 Particle size analysis	90
5.2.9 In vitro aerosol dispersion performance with the Next Generation Impactor™ (NGITM)	90
5.2.10 Cytotoxicity tests	92
5.2.11 Statistics	93
5.3 Results and Discussion.....	93
5.3.1 Physiochemical Characterization.....	93
5.3.2 Aerosol performance of inhalable powders	101
5.3.3 In vitro activity of ACAs	104
5.4 Conclusions	106
Chapter 6 Responsive Hydrogel Nanoparticles for Pulmonary Delivery.....	107
6.0 Abstract	107
6.1 Introduction	108
6.2 Material and methods	110

6.2.1 Materials	110
6.2.2 Synthesis of responsive hydrogel nanoparticles	111
6.2.3 Electron microscopy and particle sizing	112
6.2.4 Colloidal stability of HNPs	112
6.2.5 pH response of HNP diameter with dynamic light scattering.....	113
6.2.6 pH response of HNP diameter with dynamic light scattering.....	113
6.2.7 Inhalable HNP composites from spray drying.....	113
6.2.8 Aerosol performance with the Next Generation Impactor™ (NGI™)	114
6.3 Results and Discussion.....	116
6.4 Conclusions	131
Chapter 7 Conclusions	132
Appendix A Transport in PEG-Based Hydrogels: Role of Water Content and Crosslinker Molecular Weight	137
A.0 ABSTRACT	137
A.1 INTRODUCTION.....	137
A.2 Material and methods	141
A.2.1 Materials.....	141
A.2.2 Synthesis of hydrogels through UV polymerization.....	141
A.2.3 Conversion of hydrogels through Fourier Transform Infrared Spectroscopy (FTIR) analysis.....	142
A.2.4 Swelling studies	143
A.2.5 FCS setup.....	143
A.2.6 FCS Data Analysis	144
A.3 Results and Discussion	145
A.3.1. Hydrogel synthesis	145
A.3.2 Swelling studies	147
A.3.2 Probe diffusion in PEG hydrogels	151
A.4 Conclusions	156
Appendix B Supplemental Figures	158

References	159
Vita	177

List of Tables

Table 3.1: Summary of experimental conditions for inhalable dry powders.....	41
Table 3.2: MnM and MNP diameters, MNP loadings, and water content of MnMs.....	51
Table 3.3: Aerosol performance properties for inhalable MnMs.....	57
Table 4.1: Summary of treatment groups for TM analogs for inhalable dry powders....	66
Table 5.1: Summary of experimental conditions for inhalable dry powders.....	87
Table 5.2: Diameter from SEM and drug loading.....	97
Table 5.3: Aerosol performance properties for inhalable MnMs (mean \pm std. dev.).....	104
Table 6.1: Aerosol performance of HNP composites for inhalation (mean \pm std. dev.).	129

List of Figures

Figure 2.1: From reference (Li, Kung et al. 2013). Evolution of non–small-cell lung cancer (NSCLC) subtyping from histologic to molecular based. Data adapted (Pao and Girard 2011). EGFR, epidermal growth factor receptor; HER2, human epidermal growth factor receptor2; MAP2K1, mitogen-activated protein kinase kinase 1.....7

Figure 2.2: Taken from reference (Shepherd, Pereira et al. 2005). Kaplan-Meier Curve for Overall Survival among All Patients Randomly Assigned to Erlotinib or Placebo....12

Figure 2.3: A nanomagnetosol solution comprising PEI-pDNA gene vectors coding for the luciferase gene and SPIONs was nebulized to Balb/c-mice (n03) either with (a) or without (b) an external magnetic gradient field applied to the right chest. Twenty-four hours after nebulization luciferase activity in the lungs was measured using in vivo bioluminescence imaging in mice. The lungs were removed subsequently to conduct an ex vivo luciferase assay, revealing a mean luciferase expression of 7.2 pg luciferase per gram tissue in mice that had been exposed to a magnetic gradient and no luciferase in mice without a magnetic gradient during the nebulization procedure (c). Taken from reference (Hasenpusch, Geiger et al. 2012).....26

Figure 2.4: A nanomagnetosol solution comprising PEI-pDNA gene vectors coding for the luciferase gene and SPIONs was nebulized to Balb/c-mice (n03) either with (a) or without (b) an external magnetic gradient field applied to the right chest. Twenty-four hours after nebulization luciferase activity in the lungs was measured using in vivo

bioluminescence imaging in mice. The lungs were removed subsequently to conduct an ex vivo luciferase assay, revealing a mean luciferase expression of 7.2 pg luciferase per gram tissue in mice that had been exposed to a magnetic gradient and no luciferase in mice without a magnetic gradient during the nebulization procedure (c). Taken from reference (Hasenpusch, Geiger et al. 2012).....28

Figure 2.5: From reference (Wang, Lai et al. 2008). Mucoinert (open symbols) vs. Mucoadhesive (filled symbols) behaviour of nanoparticles figure.....31

Figure 2.6: From reference (Sonaje, Lin et al. 2009). Behaviour of oral (◆) and subcutaneous (■) insulin solution and insulin-loaded nanoparticles (▲) in diabetic rats.....33

Figure 3.1: Schematic representation of the formulation and application of magnetic nanoparticle microcomposites (MnMs). From left to right we see the initial formation of these inhalable dry powders through spray-drying a feed consisting of iron oxide MNPs dispersed in a D-mannitol solution of methanol. Upon collection these materials were loaded into a capsule and placed into a dry powder inhaler for in vitro aerosol dispersion performance studies in order to model their predictive deposition patterns in the lungs. Finally, the heating properties of the MNPs released from these MnMs upon dissolution were verified by exposing them to an alternating magnetic field.....39

Figure 3.2: SEM images of a) MF20, b) MF5, and c) MF0 dry powders. Magnification 5,000x.....	49
Figure 3.3: TEM images of a) MF20, b) MF5, and c) MF0 dry powders.....	49
Figure 3.4: XRPD diffractograms for MnM powders.....	53
Figure 3.5: DSC thermograms for MnM powders.....	54
Figure 3.6: Aerosol dispersion performance plot for MnM powders using the NGI at 60 L/min.....	56
Figure 3.7: Heating curves for MnMs under AMF exposure.....	58
Figure 3.8: <i>In vitro</i> cytotoxicity results for human A549 alveolar epithelial adenocarcinoma cells after 24 hours of exposure to MnMs at 37°C.....	59
Figure 4.1: Microscopy images (n=3) of TM analogs after MNP-exposure (-AMF). The treatment groups are arranged in columns with increasing MNP dose from left to right. Left column is control group (n=3); middle column is LD MNPs; right column is HD MNPs. Each panel consists of the following 4 images: green fluorescent (MEF cells, top left), red fluorescent (4T1, top right), bright-field (bottom left), and overlay (bottom right). Images were captured t=5 days post MNP exposure.....	70

Figure 4.2: Comparison of TM analogs with- (+AMF; bottom row) and without (-AMF; top row) application of AMF for 1-hour. The treatment groups are arranged in columns with increasing MNP dose from left to right. Left column is control group (n=3); middle column is LD MNPs; right column is HD MNPs. Each panel consists of the following 4 images: green fluorescent (MEF cells, top left), red fluorescent (4T1, top right), bright-field (bottom left), and overlay (bottom right). Images were captured t=5 days after AMF exposure.....71

Figure 4.3: Representative fluorescent images of (top row; a-c) and bright-field (bottom row; d-f) images of spheroids stained with SYTOX® Blue dead cell stain and not exposed to AMF. From left to right the columns represent treatments of control (a,d) MNPs at 0.1 mg/mL (b,e) and MNPs at 1 mg/mL (c,f).....73

Figure 4.4: Quantification of dead cell count measured as the mean integrated density of blue signal from fluorescent images.....74

Figure 4.5: Prussian blue staining of multicellular breast cancer micrometastatic spheroids. From left to right the columns represent treatments of control (a,d) MNPs at 0.1 mg/mL (b,e) and MNPs at 1 mg/mL (c,f) with the top row (a-c) being treatments without AMF exposure and the bottom row (d-f) exposed to AMF.....75

Figure 4.6: TEM images of the center of TM analogs. Control –AMF (left column; a, d), LD –AMF (middle column; b, e), and HD +AMF (right column; c, f) at magnifications of x2900 (top row; a-c) and x6800 (bottom row; d-f). Red arrows point at extracellular material in MNP treatments.....76

Figure 4.7: TEM images of cells displaying massive vacuolization of the cytoplasm at magnifications of a) x6800, b) 11,000, and c) 23,000. Red box shows where adjacent image is located in lower mag image.....77

Figure 4.8: TEM images of the edge of TM analogs. Control –AMF (left column; a, d), LD –AMF (middle column; b, e), and HD +AMF (right column; c, f) at magnifications of x2900 (top row; a-c) and x6800 (bottom row; d-f). Red arrows point at large MNP agglomerates.....78

Figure 4.9: TEM images of HD MNP -AMF TM analogs at x2900 (a, d), x4800 (b, e) and x6800 (c, f). Top row (a-c) are images from center of TM analog and bottom row (d-f) are images from edge.....79

Figure 5.1: Representative SEM images of a) MC0 and b) MC10 at magnification of 5,000x with inset at 30,000x95

Figure 5.2: Representative SEM images of a) ME0 and b) ME10 at magnification of 5,000x with inset at 30,000x.....96

Figure 5.3: XRPD diffractograms for raw cisplatin (top), MC10 (middle) and MC0 (bottom).....	98
Figure 5.4: XRPD diffractograms for raw erlotinib (top), ME10 (middle) and ME0 (bottom).....	99
Figure 5.5: DSC thermograms for raw cisplatin, MC10, and MC10.....	100
Figure 5.6: DSC thermograms for raw erlotinib, ME0, and ME10.....	101
Figure 5.7: Aerosol dispersion performance plot for MC0 and MC10 powders.....	103
Figure 5.8: Aerosol dispersion performance plot for ME0 and ME10 powders.....	103
Figure 5.9: <i>In vitro</i> comparison of raw cisplatin and MC10 in human lung cancer cell lines A549 (left) and H358 (right).....	105
Figure 5.10: <i>In vitro</i> comparison of raw erlotinib and ME10 in human lung cancer cell lines A549 (left) and H358 (right)	105
Figure 6.1: Representation of responsive hydrogel nanoparticles at varying pH conditions from low (left) to high (right).....	118

Figure 6.2: Hydrodynamic diameter of HNP120s a) over a large range of pH values and b) zoomed in above transition pH.....	119
Figure 6.3: Hydrodynamic diameter of HNP270s a) over a large range of pH values and b) zoomed in above transition pH.....	119
Figure 6.4: Hydrodynamic diameter of HNP120 (diamonds) and HNP270 (squares) showing difference in transition pH.....	120
Figure 6.5: SEM images of HNP120s at a) x100k and b) x180k. ImageJ® size analysis shows $82.6 \text{ nm} \pm 4.3 \text{ nm}$	122
Figure 6.6: SEM images of HNP270s a) x35k and b) x150k. ImageJ® size analysis shows $133.4 \text{ nm} \pm 12.2 \text{ nm}$	122
Figure 6.7: Representative TEM images of representative HNP120s on copper TEM grid illustrating spherical morphology and size uniformity. The diameters of two representative particles are: a) 80.7 nm and b) 88.7 nm.....	124
Figure 6.8: High mag (x500k) TEM image of individual HNP120 with fast Fourier Transform inset showing amorphous character of HNPs.....	124

Figure 6.9: Stability of HNP120s above and below transition pH.....126

Figure 6.10: SEM image of SD HNP120 composite dry powder with individual particle shown in top right corner inset.....127

Figure 6.11: Aerosol dispersion performance plot for inhalable responsive HNPs.....128

Figure 6.12: Hydrodynamic diameter of HNP120s and SD HNP120s a) over a large range of pH values and b) zoomed above transition pH.....130

Figure 6.13: Stability of HNP120s and SD HNP120s above transition pH shows population of SD HNP120s that fall out of suspension.....131

Chapter 1 Introduction

Cancer is designated as the leading cause of mortality worldwide with an estimated 8.2 million deaths in 2012 (Ferlay, Soerjomataram et al. 2013). In the United States, one in four deaths is caused by this devastating disease with nearly 30% of these resulting from lung cancer (Siegel, Naishadham et al. 2012). Non-small cell lung cancer (NSCLC) accounts for approximately 85% of all lung cancers and is the leading cause of cancer mortality worldwide (Mellas, Elmesbahi et al. 2010, Bonomi, Pilotto et al. 2011, Tucker, Laguna et al. 2012).

Although the initial treatment of NSCLC differs depending on stage, physical health of the patient, and a variety of other factors, the preferred treatment is surgical resection; however, most NSCLCs are diagnosed as inoperable stage III or stage IV malignancies (Fathi and Brahmer 2008, Mazzone and Mekhail 2012, Tucker, Laguna et al. 2012). Unfortunately, over 40% of patients develop recurrences after surgery even with adjuvant treatments such as radiation or chemotherapy (Bonomi, Pilotto et al. 2011, Tucker, Laguna et al. 2012). This, among other factors, contributes to 5- and 10-year mortality rates of less than 15 and 7% respectively (Crino, Weder et al. 2010). Hence, there is a great need for more effective non-surgical treatments of NSCLC, and, considering the large mortality rates, any improvement on current strategies would bring about a great benefit.

Targeted pulmonary delivery is well established for treating pulmonary diseases such as asthma and displays characteristics that are promising for its translation into a novel lung cancer treatment strategy (Hasenpusch, Geiger et al. 2012). For NSCLC

therapy, this route of drug delivery could lead to increased concentrations of ACAs in lung tissue and therefore reduced systemic side effects when compared to an equivalent intravenous dose. Hence, it is possible that targeted pulmonary delivery could be used to administer local doses that are higher than current clinical practices and thus result in a more effective treatment modality for NSCLC patients.

Inhalable therapies, traditionally, consist of liquid droplets or solid particles with a mass median aerosol diameter (MMAD) of $<5 \mu\text{m}$ in order to be respirable (Hickey, Mansour et al. 2007, Xu, Mansour et al. 2010). Common inhalable therapies include nebulizers, metered dose inhalers, and dry powder inhalers (DPIs). Dry powder inhalation systems are preferable to traditional metered dose inhalers and nebulizers because of superior stability and ease of use for associated devices (El-Gendy and Berkland 2009). Conversely, spray drying provides the ability to reproducibly formulate dry powders consisting of microparticles that are suitable for pulmonary delivery and offers the ability to control certain physiochemical properties of these particles by adjusting process parameters (Vanbever, Mintzes et al. 1999, Mobus, Siepmann et al. 2012, Odziomek, Sosnowski et al. 2012, Shen, Chen et al. 2012). Additionally, spray-drying allows for easy production of aerodynamically adequate carriers of nanoparticles and ACAs that could further enhance the effectiveness of locally delivering the therapy.

This dissertation includes an investigation and discussion of a range of inhalable nanocomposites for the targeted treatment of lung cancer with the overall goal being the development of a novel lung cancer treatment modality that could improve on current non-surgical clinical practices. These nanocomposites consisted of iron oxide magnetic nanoparticles (MNPs), anticancer agents (ACAs) and hydrogel nanoparticles (HNPs) in

varying combinations. Formulation of the inhalable powders was accomplished via spray drying and Chapter 2 presents a background of the nanomaterials and formulation techniques.

1.1 Objectives

The overall objective of this dissertation was to examine the feasibility and potential of spray drying nanoparticles and anticancer agents into inhalable composite powders as innovative treatment modalities for patients with primary and secondary lung cancer. This was accomplished through the following four projects:

1. “Formulation and Characterization of Inhalable Magnetic Nanocomposite Microparticles for Targeted Pulmonary Delivery”
2. “Remote controlled thermal therapy with magnetic nanocomposite microparticles induces cell death in triple negative breast cancer micrometastatic tumor tissue analogs”
3. “Inhalable Anticancer Agents for Targeted Pulmonary Delivery and Lung Cancer Therapy”
4. “Responsive Hydrogel Nanoparticles for Pulmonary Delivery”

This dissertation begins with background on the relevant aspects of this research in Chapter 2. Current non-surgical treatments of non-small cell lung cancer, magnetic nanoparticles (MNPs), pulmonary delivery, and hydrogel nanoparticles (HNPs) are reviewed in order to highlight their potential in cancer therapy applications. Chapter 3, titled “Formulation and Characterization of Inhalable Magnetic Nanocomposite

Microparticles for Targeted Pulmonary Delivery,” involves the incorporation of magnetic nanoparticles into dry powder composites via spray drying. The physicochemical properties of these composites are then thoroughly evaluated and their potential for targeted remote-controlled thermal therapy is examined by heating studies in an alternating magnetic field (AMF) and *in vitro* aerosol performance studies. Chapter 4 is a continuation of Chapter 3 wherein the magnetic nanoparticle microcomposites (MnMs) formulated in Chapter 3 are evaluated for their application in metastatic triple-negative breast cancer (TNBC). Specifically, the fourth chapter is titled “Remote controlled thermal therapy with magnetic nanocomposite microparticles induces cell death in triple negative breast cancer micrometastatic tumor tissue analogs.” Chapter 5, titled “Inhalable Anticancer Agents for Targeted Pulmonary Delivery and Lung Cancer Therapy” presents the results of incorporating two commonly administered anticancer agents, cisplatin and erlotinib, into inhalable dry powder composites. The aerodynamic performance of these dry powders is examined and the activity of the released ACAs is studied on two human lung cell lines. Chapter 6, “Responsive Hydrogel Nanoparticles for Pulmonary Delivery,” reports the synthesis and incorporation of responsive hydrogel nanoparticles (HNPs) into inhalable composites through spray drying. These HNPs respond to changes in pH by swelling and/or agglomerating and have potential for future development into triggered drug release carriers that respond to the reduced pH in the tumor environment. Finally, Chapter 7 reports the conclusions of this research.

Chapter 2 Pulmonary Delivery for Targeted Lung Cancer Therapy

Over the last several decades great efforts have been poured into lung cancer research. Billions of dollars in funding (\$254 million from NIH in 2014 alone) and countless hours of research have been invested in attempts to, ultimately, find a cure for this pervasive disease (Health 2015). However, the return on this investment has not been as fruitful as anticipated, as survival rates have shown minimal improvements over the last 40 years. Still, much effort is needed to improve these dismal survival rates and enhance the quality of life for lung cancer patients.

2.1 Types of Lung Cancer

Traditionally, primary lung cancer can be split into two main histological types called small cell lung cancer (SCLC) and non-small cell lung cancer (NSCLC), with the latter accounting for approximately 80-85% of all cases (Molina, Yang et al. 2008, Zarogoulidis, Zarogoulidis et al. 2013). SCLC, the less common histological type, is split into two sub groups referred to as pure- and combined small-cell lung cancer (SCLC and CSCLC, respectively) (Wallace, Arya et al. 2014). In CSCLC any additional component of NSCLC subtype is present along with SCLC and it represents approximately 30% of all SCLC cases (Wagner, Kitabayashi et al. 2009). There is a higher proportion of SCLC patients who are smokers than in NSCLC patients and SCLC has very low 5-year survival rates of 1-2% for extensive-stage SCLC (Wallace, Arya et al. 2014).

Non-small cell lung cancer represents the majority population of lung cancer patients and, traditionally, can be split into three major subtypes referred to as squamous

cell carcinoma, large cell carcinoma, and adenocarcinoma (Zarogoulidis, Zarogoulidis et al. 2013), but with a large genetic diversity within each of these major types. Of these three histological classifications, adenocarcinoma is the most common type of NSCLC and, interestingly, presents with known oncogenic mutations in over 60% of cases (Oxnard, Binder et al. 2013, !!! INVALID CITATION !!!).

Modern advances in genetic profiling have led to the general acceptance that histological classification, by itself, insufficiently describes a particular type of NSCLC cancer (Mar, Vredenburgh et al. 2015). Today, it would be considered negligence for an oncologist to determine a chemotherapy regimen for a NSCLC patient without first knowing the mutation status of certain common genetic mutations (called oncogenes) such as ALK and EGFR (Oxnard, Binder et al. 2013, Iacono, Chiari et al. 2015). Figure 2.1 provides a look at oncogenes identified in NSCLC and illustrates the relative degree of incidence in two separate histological classifications (Oxnard, Binder et al. 2013).

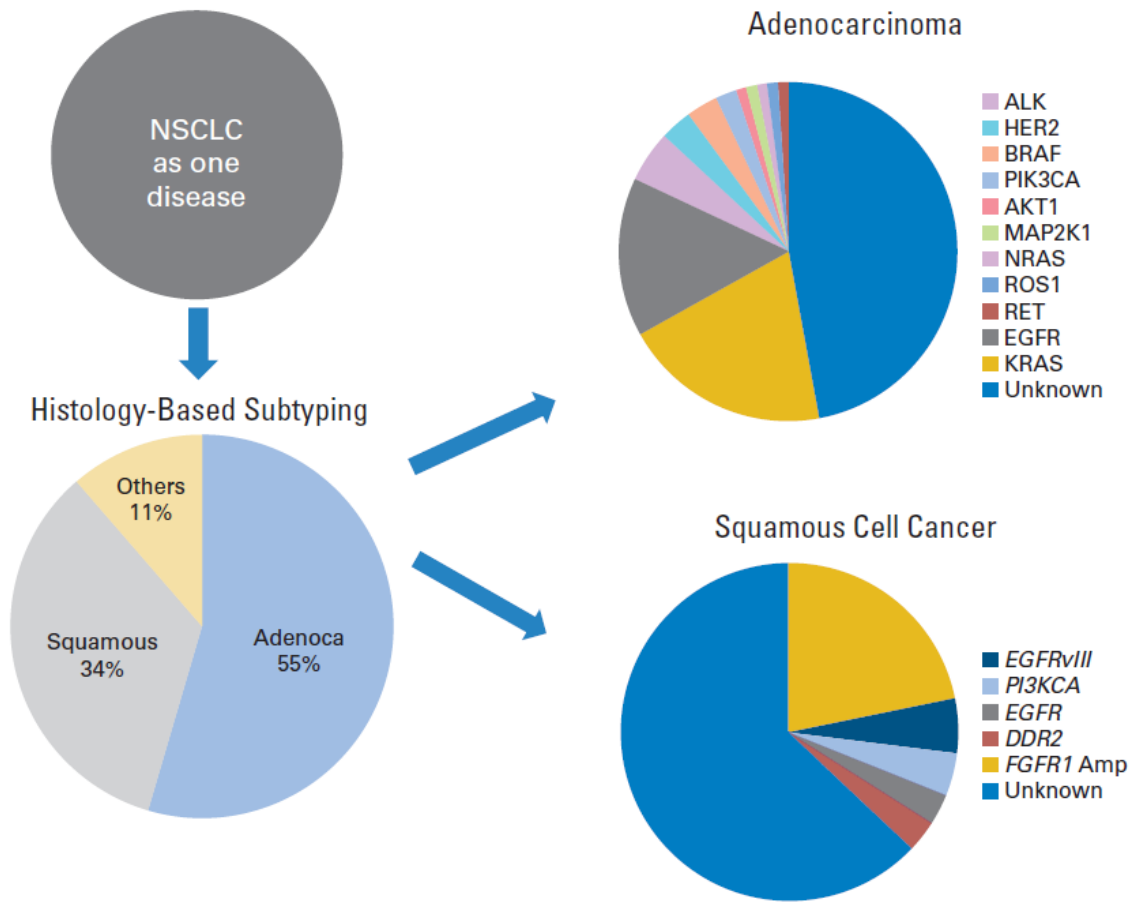


Figure 2.1: From reference (Li, Kung et al. 2013). Evolution of non-small-cell lung cancer (NSCLC) subtyping from histologic to molecular based. Data adapted (Pao and Girard 2011). EGFR, epidermal growth factor receptor; HER2, human epidermal growth factor receptor2; MAP2K1, mitogen-activated protein kinase kinase 1.

2.2 Current Non-Surgical Treatments of NSCLC

Non-surgical approaches to treating locally advanced NSCLC are primarily combinations of adjuvant- and neoadjuvant radiotherapy (RT) and chemotherapy (CT). Late stage disease is treated with primarily with systemic therapies such as CT and targeted agents. Different guidelines exist for treatment options of NSCLC patients but

these decisions are largely dictated by stage and surgery preference (when possible). Staging of NSCLC is completed using the TNM system that depends on tumor size (T), lymph node involvement (N) and degree of metastasis (Institute 2015). Here we provide a quick glance of current treatment approaches for different stages of NSCLC patients in order to provide a convenient overview of these options, yet we understand that cancer is a highly heterogeneous disease and requires case-by-case treatment plans that do not necessarily fall under the generalizations provided here. Additionally, we present background information on the most commonly employed chemotherapeutic agent for NSCLC patients, discuss trends in personalizing NSCLC therapy, and provide background on erlotinib (Tarveva®), which was the first successful drug for genetically targeted NSCLC treatment.

2.2.1 Treatment options based on pathological stage

As expected, the prognosis for NSCLC patients depends on pathological stage, with lower stages having superior survival rates (Zarogoulidis, Zarogoulidis et al. 2013). Stage I-IIIb patients who do not have surgical resection (by choice or circumstance) are typically administered a form of RT or placed into a clinical trial (Institute 2015). For patients not entering a clinical trial, the type of RT administered as well as the combination of CT varies based on a number of factors (Institute 2015).

For those patients who undergo surgical resection, stage I cases are not generally given adjuvant CT or RT unless admitted to a clinical trial involving such approach (Zarogoulidis, Zarogoulidis et al. 2013). Large meta-analyses have confirmed the benefit of cisplatin-based adjuvant CT for resected stage II-IIIa NSCLC patients, leading to the

designation of this treatment modality as the gold standard for such cases (Pisters, Evans et al. 2007, Robinson, Ruckdeschel et al. 2007, Scott, Howington et al. 2007, Crino, Weder et al. 2010, Zarogoulidis, Zarogoulidis et al. 2013); however, some guidelines include neoadjuvant CT as a treatment option as well as RT alone for certain patients such as stage IIIA cases (Institute 2015). Radiotherapy is also administered in combination with platinum-based CT for certain resected stages II-IIIa patients and lymph node involvement plays a large role in prescribing this treatment modality (Zarogoulidis, Zarogoulidis et al. 2013).

Advanced stage IIIB-IV have a very poor prognosis and therefore a variety of CT and RT treatment options are considered as well as maintenance therapy or best supportive care. However, the standard first-line treatment for advanced NSCLC patients is a platinum-based two drug combination regimen (Gatzemeier, Pluzanska et al. 2007). Recently, it was suggested that stage IIIB-IV and inoperable patients receive 4 cycles of cisplatin-based CT along with a third-generation cytotoxic or cytostatic drug (Zarogoulidis, Zarogoulidis et al. 2013).

Cisplatin was first examined for anticancer activity in 1968 after showing inhibition of cell proliferation in bacteria cultures (Rosenberg 1985). Since its approval for medical use in 1978 by the United States Food and Drug Administration (FDA), this anticancer agent (ACA) has been used in the treatment of a variety of cancers such as ovarian, testicular, and bladder as well as head and neck cancer (Babincova, Altanerova et al. 2008). Cisplatin is still considered the gold-standard for treatment of many types of NSCLC and is classified as a cytotoxic ACA (Zarogoulidis, Zarogoulidis et al. 2013). One of the main mechanisms of cisplatin-induced cytotoxicity lies in the ability of

cisplatin to form irreversible crosslinks in DNA causing G1 cell cycle arrest and apoptosis [13]. While cisplatin is a highly toxic and nonspecific ACA, more recent efforts to personalize cancer treatment have led to the development of drugs targeted to patients with specific genetic alterations.

2.2.2 Personalized treatment of NSCLC patients

Personalized treatment of NSCLC patients with molecularly targeted therapies is revolutionizing the way researchers and clinicians approach this devastating disease (Li, Kung et al. 2013, Oxnard, Binder et al. 2013). These rational therapies are based on commonly mutated genes in NSCLC patients (called oncogenes) and the resulting drugs have provided an unprecedented step forward in treatment of a disease that has only seen marginal improvement over the last 40 years (Oxnard, Binder et al. 2013). The success of these treatments is also leading to paradigm shift in treatment selection from empirical- to rational design and will undoubtedly play a role in future guidelines for standard treatment options (Li, Kung et al. 2013). Our increased understanding of oncogenes and recent groundbreaking clinical studies with targeted therapies are transforming the way we treat NSCLC patients by using molecularly targeted anticancer agents for personalized therapy based on genetic profiles. One early example of this is erlotinib (Rosell, Carcereny et al. 2012, Oxnard, Binder et al. 2013, Mar, Vredenburgh et al. 2015).

Erlotinib (Tarceva[®]), a small molecule tyrosine kinase inhibitor (TKI), was approved for the treatment of NSCLC and is given to patients with tumor associated epidermal growth factor receptor (EGFR) mutations as it showed a survival benefit for

such patients (Eberhard, Johnson et al. 2005, Shepherd, Pereira et al. 2005, Gatzemeier, Pluzanska et al. 2007). Unlike cytotoxic drugs (e.g. cisplatin), cytostatic drugs such as erlotinib prevent proliferation of cells as opposed to inducing cellular death (Gatzemeier, Pluzanska et al. 2007). The mechanism by which erlotinib, and other EGFR-TKIs, prevent cancer growth involves binding the intracellular domain of EGFR at the adenosine triphosphate binding site (Smith 2005). Binding of erlotinib to EGRF inhibits phosphorylation and thereby prevents activation of multiple downstream pathways including the PI3K-AKT-mTOR and RAS-RAF-MEK-ERK pathways involved in cell survival and proliferation, respectively (Hirte 2013).

The groundbreaking Phase III study completed by Shepherd et al. showed a better Kaplan-Meier curve for overall survival (OS) (Figure 2.2) in EGFR+ patients given erlotinib versus those treated with standard chemotherapy, and illustrated the effectiveness of targeted therapies in NSCLC therapy (Rosell, Carcereny et al. 2012). Additionally, over 25% of all lung cancers, and up to 80% of NSCLCs, over express EGFR; hence, NSCLC represents a large number of patients whom are candidates for targeted therapy with targeted therapies such as erlotinib (Gatzemeier, Pluzanska et al. 2007, Kanthala, Pallerla et al. 2015). Figure 2.2 is from (Rosell, Carcereny et al. 2012).

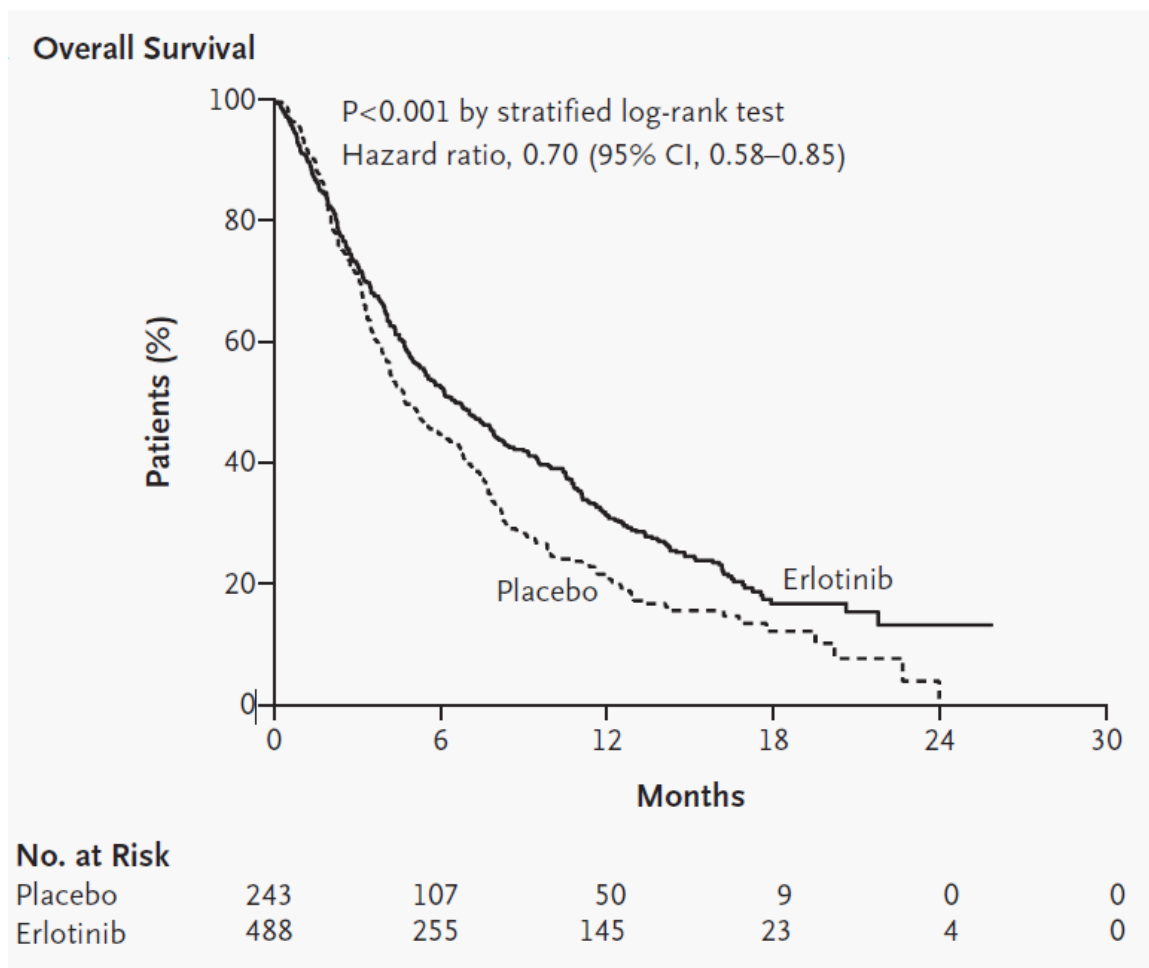


Figure 2.2: Taken from reference (Shepherd, Pereira et al. 2005). Kaplan-Meier Curve for Overall Survival among All Patients Randomly Assigned to Erlotinib or Placebo.

2.3 Pulmonary Delivery

Targeted pulmonary delivery is well established for treating diseases of the lung such as asthma and displays characteristics that are promising for its translation into a novel lung cancer treatment modality (Hasenpusch, Geiger et al. 2012). The performance of a pharmaceutical aerosol is quantified with a variety of parameters, the most important of which is the aerodynamic diameter, D_A . The aerodynamic diameter of a given particle

(or droplet) is largely dependent on size, shape, surface roughness, and density (Chow, Tong et al. 2007, Vehring 2008). Qualitatively, D_A represents the diameter of a geometrically perfect sphere of unit density, and zero surface roughness, that would reach the same terminal velocity in air as the actual, non-ideal, particle (Chow, Tong et al. 2007, Vehring 2008). Quantitatively, it is derived by equating the terminal velocities of the ideal and non-ideal particle as shown in equation 2.1 below (Anthony J. and Mansour 2009):

$$V_T = \frac{\rho_p g D_p^2 C(D_p)}{\kappa_p 18 \eta} = \frac{\rho_0 g D_A^2 C(D_A)}{\kappa_0 18 \eta} \quad (\text{Equation 2.1})$$

Here, the subscript p indicates properties of the particle of interest and A indicates those properties of the idealized aerodynamic particle (or droplet); g is the acceleration of gravity; η is the viscosity of air; D_i , ρ_i , κ_i , and $C(D_i)$, are the diameter, density, shape factor, and slip correction factor of species i (which, for the idealized case, become unity for ρ_i and κ_i). For particles with a diameter $> 1 \mu\text{m}$ this equation becomes:

$$D_A = D_p \sqrt{\frac{\rho}{\kappa_p}} \quad (\text{Equation 2.2})$$

Additionally, the majority of pharmaceutical aerosols display spherical morphology or have rotational symmetry, therefore the shape factor, κ_p , is equal to one (Anthony J. and Mansour 2009).

Experimentally, the aerodynamic diameter is determined through inertial impaction studies using cascade impactors and is referred to as the mass median aerosol diameter (MMAD). A large advantage to such empirical determination of the aerodynamic diameter is not needing to know the shape factor or density of the aerosol formulation (Anthony J. and Mansour 2009). Usually, inhalable aerosol therapies consist

of liquid droplets or solid particles with a MMAD $< 5 \mu\text{m}$ in order to be respirable (Hickey, Mansour et al. 2007, Xu, Mansour et al. 2010).

2.3.1 Pulmonary delivery for lung cancer treatment

Traditionally, anticancer agents (ACAs) are administered intravenously or, to a lesser extent, orally for systemic delivery (Carvalho, Carvalho et al. 2011). However, studies have shown that systemic delivery results in relatively low concentration of drug in the desired site within the lungs, and this, among other factors, has lead researchers to examine inhalation as means of administering ACAs to patients with lung malignancies (Vaughn, McConville et al. 2006, Carvalho, Carvalho et al. 2011).

For NSCLC therapy, pulmonary delivery could lead to increased concentrations of ACAs in lung tissue and therefore reduced systemic side effects when compared to an equivalent systemic dose. Conversely, reports have indicated as much as a 10-fold increase in drug concentration within the lungs when administered via pulmonary delivery relative to systemic delivery via oral administration (Vaughn, McConville et al. 2006). Hence, it is possible that targeted pulmonary delivery could be used to administer local doses that are higher than current clinical practices and thus result in an effective treatment modality for NSCLC patients.

Phase I studies of inhaled cisplatin (via nebulization) reached no maximum tolerated dose and observed no dose limiting toxicity at up to 60 mg/m^2 compared with clinically accepted dosages of $50\text{-}100 \text{ mg/m}^2$ (Wittgen, Kunst et al. 2007). Additionally, phase I/II studies of inhalable doxorubicin showed no systemic toxicity for all administered doses; however, dose-limiting occurred due to direct effects on the upper

and lower respiratory tract (Otterson, Villalona-Calero et al. 2007, Otterson, Villalona-Calero et al. 2010).

A study evaluating the effectiveness of inhaled carboplatin (nebulized liquid solution) revealed a significant increase in survival for stage IV NSCLC patients who received a combination of intravenous and pulmonary drug administration as opposed to IV- or pulmonary only (Zarogoulidis, Eleftheriadou et al. 2012). This suggests that even advanced-stage NSCLC patients could potentially benefit from a portion of their chemotherapy being delivered via inhalation and illustrates the potential for inhaled ACAs in both local and metastatic lung malignancies. This potential of inhaled chemotherapy in secondary lung cancer patients was examined in a phase Ib/IIa study with inhaled cisplatin (via nebulization) on metastatic osteosarcoma patients. Two out of the 14 patients in this study had no pulmonary disease one year after inhalation of therapy, thereby confirming the potential of pulmonary delivery for both primary and secondary lung cancer patients (Chou, Bell et al. 2007). One limitation of traditional inhalation techniques used in most clinical studies (i.e. nebulization) is low aqueous solubility of hydrophobic anticancer agents such as taxanes, but this limitation could be overcome through dry powder inhalation (Carvalho, Carvalho et al. 2011).

2.3.2 Dry powders for inhalation

Dry powder formulations are promising in biomedical applications due to propellant-free, low-cost devices (Rahimpour, Kouhsoltani et al. 2014) as well as improved stability of the formulation as a result of the dry state (Carpenter, Pikal et al. 1997). Devices for administering dry powders (i.e. dry powder inhalers or DPIs) are

breath-activated, which can reduce variability associated with inhaling liquid aerosols by avoiding necessary coordination of patients (Timsina, Martin et al. 1994, Todo, Okamoto et al. 2001). Additionally, dry powder formulations do not require active ingredients to be water soluble and, considering the wide variety of anticancer agents, offer a more promising approach than liquid aerosols for treating this disease. The primary particles in dry powder formulations can also be tailored by particle engineering technologies such as spray drying and therefore designed for regional targeting within the lungs, which is not possible to the same extent with liquid aerosols (Daniher and Zhu 2008, Son and McConville 2008).

Spray drying provides the ability to reproducibly formulate dry powders, consisting of microparticles, that are suitable for pulmonary delivery and offers the ability to control certain physiochemical properties of these particles by adjusting process parameters (Vanbever, Mintzes et al. 1999, Mobus, Siepmann et al. 2012, Odziomek, Sosnowski et al. 2012, Shen, Chen et al. 2012). Additionally, this technique enables easy production of powders composed of multiple chemical species by simply dispersing them in the feed solvent (Stocke, Meenach et al. 2014). Incorporating small molecules, such as most ACAs, into spray dried powders simply requires selecting a solvent appropriate for spray drying in which your excipients and active ingredients are soluble and optimizing the conditions for the particular formulation.

Nanoparticles can also be incorporated into composite powders through spray drying. Incorporating nanoparticles into larger composites is thought to be necessary, as some have suggested they are too small for pulmonary delivery due to lack of deposition and subsequent exhalation (Azarmi, Tao et al. 2006, Stocke, Meenach et al. 2014).

Hence, spray-drying can be used to incorporate ACAs and multifunctional nanoparticles into inhalable dry powders thereby opening up an entire field of nano-based drug delivery platforms that could be utilized to treat NSCLC patients. These factors, among others, have led to the assertion that dry powders are superior to liquid based formulations (El-Gendy and Berkland 2009, Rahimpour, Kouhsoltani et al. 2014).

2.4 Hydrogels Nanoparticles

Hydrogels represent an important class of biomaterials with a wide variety of applications including, among others, tissue engineering, biosensors, drug delivery, and medical implants (Peppas, Keys et al. 1999, Peppas, Bures et al. 2000, Kopecek 2009). Traditionally, hydrogels are defined as three-dimensional polymeric networks formed by crosslinking hydrophilic polymers, and many of their applications center around gels at equilibrium (e.g. contact lenses) (Peppas, Bures et al. 2000, Peppas, Hilt et al. 2006). However, the responsive behavior of hydrogel materials provides them with unique capabilities in biomedical applications (Gupta, Vermani et al. 2002).

Responsive hydrogels have been examined thoroughly over the past several years and researchers have used a variety of approaches to achieve desired functionality (Gupta, Vermani et al. 2002). By incorporating various monomers, crosslinkers, and synthesis conditions one can tune the hydrogel to respond in a variety of manners including degradation of the hydrogel network or swelling/shrinking of the gel (Ghandehari, Kopeckova et al. 1997, De, Aluru et al. 2002). Additionally, the response of the hydrogel can be initiated by a variety of external stimuli such as heat, specific analytes, and changes in pH (Soppimath, Aminabhavi et al. 2002, Yang, Peters et al.

2008, Anthony J. and Mansour 2009). Although hydrogels are generally fabricated at the macroscale, hydrogel nanoparticles represent a unique class of responsive nanoparticles.

Hydrogel nanoparticles (or nanogels) are crosslinked structures that, as with the bulk-scale counterparts, have a high water content that provides enhanced biocompatibility (Oh, Drumright et al. 2008). When these particles are formulated to be < 200 nm these particles are excellent candidates as drug carriers due to receptor mediated cellular uptake and prolonged circulation times by eluding uptake by the mononuclear phagocyte system (Oh, Drumright et al. 2008). Additionally, the structure of these particles provides them with a unique interior that is in contact with its surroundings and thereby yields drug carrier systems with a vast range of applications.

Previous reports of delivering hydrogel particles to the lungs via pulmonary administration demonstrated the ability to engineer micron-sized hydrogel particles that can be delivered to the lungs as stand-alone carriers (El-Sherbiny and Smyth 2010, Du, El-Sherbiny et al. 2014, Secret, Kelly et al. 2014). Liquid aerosols of hydrogel micro- and nanoparticle suspensions were also accomplished using metered dose inhalers and nebulizers (Farhat, Holloway et al. 2009, Selvam, El-Sherbiny et al. 2011). Additionally, the *in vivo* administration of 220 nm nanogels showed sustained release of a model peptide after pulmonary administration, thereby illustrating the potential of HNPs administered via inhalation (Lee, Lee et al. 2012). As such, hydrogel nanoparticles represent a class of materials that has promise for incorporation into novel drug delivery systems such as inhalable composites for lung cancer applications.

2.5 Iron Oxide (Fe₃O₄) magnetic nanoparticles

A large amount of cancer-related research has pointed to the benefits of utilizing nanotechnology in the development of novel treatment strategies (Pankhurst, Connolly et al. 2003, Ferrari 2005, Peer, Karp et al. 2007, Cho, Wang et al. 2008). Iron oxide (Fe₃O₄) magnetic nanoparticles (MNPs) represent a unique class of nanomaterials and have generated considerable interest in biomedicine due to their broad applicability in biomedical fields. Tissue engineering, biosensing, drug delivery, and hyperthermia represent a few such applications in which MNPs have great potential (Reddy, Arias et al. 2012). Additionally, MNPs have been approved by the FDA for several commercial products including their use as an MRI contrast agent. The dual potential of these materials in therapy and diagnostics – so called theranostics – makes MNPs especially attractive for future development in cancer applications (Pankhurst, Connolly et al. 2003, Frimpong and Hilt 2010, He, David et al. 2013).

Over the years, a wide variety of MNP-based drug delivery systems have been developed through techniques such as surface coatings and magnetic composites (Satarkar and Hilt 2008, Satarkar and Hilt 2008, Hawkins, Bottom et al. 2012, Wydra, Kruse et al. 2013, Kruse, Meenach et al. 2014, Stocke, Meenach et al. 2015). Many of these applications take advantage of the unique capability of MNPs to heat in the presence of an alternating magnetic field (AMF). Under such conditions, MNPs generate thermal energy through frictional (Brownian) and magnetic (Neel) relaxation processes, and this heat can be used to trigger other therapies, increase transport of particles, or induce hyperthermia as a thermal treatment (Frimpong, Fraser et al. 2007, Satarkar and

Hilt 2008, McGill, Cuylear et al. 2009, Yakacki, Satarkar et al. 2009, Knecht, Ali et al. 2012).

The ability of a MNP system to heat in an alternating magnetic field can be quantified by calculating a specific absorption rate (SAR), which is defined in equation 2.3 below:

$$SAR = \frac{\sum C_i m_i}{m} \frac{dT}{dt} \quad (\text{Equation 2.3})$$

In this equation m_i , C_i , are the mass and specific heat capacity of component i , respectively, and m is the mass of iron oxide. SAR values are dependent on the magnetic field strength and are therefore reported along with this value. Higher SAR values for MNP systems are desirable in order to obtain maximum heating and minimum field strength. One specific, and widely studied, application of heat generation from MNPs is hyperthermia.

Hyperthermia is loosely defined as mildly heating the body tissue to an elevated temperature and can be administered to the whole body, regionally, or locally (Vertrees, Leeth et al. 2002, Wust, Hildebrandt et al. 2002). Despite mixed reports of what temperature range constitutes hyperthermia, it is generally accepted that above 46°C the treatment is referred to as thermoablation, and some have suggested 41-46°C as the range of hyperthermia (Vernon, Hand et al. 1996, Jordan, Scholz et al. 1999, Wust, Hildebrandt et al. 2002, Babincova, Altanerova et al. 2008, Colombo, Carregal-Romero et al. 2012, Ohguri, Imada et al. 2012, Xu, Karmakar et al. 2012). In isolation, hyperthermia is a viable treatment option for cancer patients and in combination with chemotherapeutic agents such as cisplatin it has shown a synergistic effect as defined by Valeriote and Lin (Valeriote and Lin 1975, Vernon, Hand et al. 1996, Jordan, Scholz et al. 1999, Wust,

Hildebrandt et al. 2002, Babincova, Altanerova et al. 2008, Ohguri, Imada et al. 2012, Xu, Karmakar et al. 2012). Additionally, recent reports of aerosols containing MNPs have elicited the ability to administer remotely actuated hyperthermia to the lungs in a targeted manner (Sadhukha, Wiedmann et al. 2013).

2.6 Magnetic nanoparticles and pulmonary delivery

Over the past decade, a growing interest in delivering MNPs directly to the lungs via pulmonary delivery is evident by the number of inhalation-based publications, which include delivery of uncoated MNPs, cubic nanoaggregates, magnetic liposomes, core-shell MNPs, high aspect ratio MNPs and dry powder magnetic composites (Ally, Martin et al. 2005, Ally, Amirfazli et al. 2006, Dames, Gleich et al. 2007, Martin and Finlay 2008, Redman, Martin et al. 2011, Hasenpusch, Geiger et al. 2012, Ragab, Rohani et al. 2012, McBride, Price et al. 2013, Ragab and Rohani 2013, Sadhukha, Wiedmann et al. 2013, Verma, Crosbie-Staunton et al. 2013, Nahar, Absar et al. 2014, Tewes, Ehrhardt et al. 2014, Stocke, Meenach et al. 2015). The attractiveness of such systems lies in the ability to noninvasively administer and localize these unique nanomaterials through pulmonary delivery, thereby presenting a drug delivery platform with obvious potential in a wide variety of applications. However, as with most biomedical applications, the therapeutic potential of inhalable MNPs must be balanced with safety considerations.

A number of reports regarding the safety of inhaled magnetic particles have presented mixed conclusions regarding the local and systemic toxicity of this route of administration; however, some have concluded that nanoparticles delivered to the pulmonary tract show no evidence of histological changes and temporary pulmonary

toxicity (Dames, Gleich et al. 2007, Cho, Cho et al. 2009, Choi, Oh et al. 2009, Kwon, Kim et al. 2009, Hasenpusch, Geiger et al. 2012, Srinivas, Rao et al. 2012, Szalay, Tatrai et al. 2012, Oakes, Scadeng et al. 2013, Verma, Crosbie-Staunton et al. 2013). Although the details of these reports are beyond the scope of this review, we acknowledge these considerations and point the readers toward potential drawbacks of this approach before continuing our discussion on inhalable applications of MNPs for inhalable therapies.

Recently, our group reported the incorporation of MNPs into inhalable dry powder composites, via spray drying, for potential applications in localized hyperthermia (Stocke, Meenach et al. 2015). We showed that these dry powders displayed good aerodynamic performance and that high loadings of MNPs were achieved while retaining adequate aerodynamic behavior. The embedded MNPs retained their heating capabilities under AMF exposure, upon released from the composites, and showed only modest *in vitro* toxicity at relatively high concentrations in A549 human lung cancer cells studies. These *in vitro* results highlight the potential of formulating inhalable dry powder composites for targeted hyperthermia applications.

Sadhuka et al. reported *in vivo* hyperthermia studies with aerosols containing EGFR-targeted magnetic nanoparticles for hyperthermia applications (Sadhukha, Wiedmann et al. 2013). In this work, the previously reported EGFR-targeting peptide (YHWYGYTPQNVI) (Li, Zhao et al. 2005) was conjugated to magnetic nanoparticles and then delivered to female Fox Chase SCID® Beige mice via inhalation of an aerosol generated through ultrasonic atomization of liquid suspensions. Their results showed that 1-week post inhalation, EGFR-targeted MNPs were retained in the lungs at concentrations higher than MNPs conjugated to a scrambled peptide. Additionally, a

murine orthotopic NSCLC model was used to examine the effectiveness of these materials for localized hyperthermia. These experiments revealed no difference in lung tumor bioluminescence among untreated-saline, non-targeted-, and targeted MNP systems when no AMF exposure was administered. Conversely, AMF-induced hyperthermia resulted in a statistically significant decrease in lung tumor bioluminescence for the EGFR-targeted MNPs exposed to AMF. These studies show *in vivo* proof-of-concept for noninvasive pulmonary delivery and targeting of MNPs for localized hyperthermia. In addition to physically targeting MNPs through inhalation, a second degree of targeting magnetic aerosols is achievable through magnetic fields.

For over 30 years, targeting magnetic material to specific regions within the body has interested researchers, but most of these reports have focused on particles in circulation (Mosbach and Schroder 1979, Widder and Senyei 1983, Driscoll, Morris et al. 1984, Pankhurst, Connolly et al. 2003). The rationale behind magnetic targeting is the same as all targeted drug delivery systems wherein localizing the therapy increases the potency within desired tissue while reducing side effects in other areas of the body. In addition to passive targeting of magnetic nanoparticles (through the enhanced permeation and retention (EPR) effect), active targeting can be achieved through a variety of approaches including surface modification, site-specific injection, and the application of a magnetic field (Silva, Silva et al. 2007). Targeting magnetic particles in circulation has been previously reviewed (Dobson 2006, Silva, Silva et al. 2007) so here we will focus our discussion on this technique as it pertains to MNP-containing aerosols.

Magnetic targeting of aerosols is a relatively new application of biomedical targeting wherein inhaled therapies can be directed to preferentially accumulate in

desired regions of the lungs. This method is particularly attracting for patients with diseased lungs, as it combines two degrees of targeting: 1) physically targeting the affected tissue through pulmonary delivery alone (discussed above) and 2) further site-specific enhancement of MNP-deposition through magnetic guidance. To our knowledge, the first report of magnetically guided aerosols for therapeutic applications was in 2005 by Ally et al. This work described theoretical concepts of magnetic aerosols and validated these hypotheses through foundational *in vitro* studies showing magnetic guidance of magnetic aerosols (Ally, Martin et al. 2005).

The *in vivo* validation of magnetic targeting as a therapeutically viable treatment modality was reported by Dames et al. in 2007. Liquid droplets containing MNPs – so-called magnetosols – were administered via nebulization and intratracheal intubation (Dames, Gleich et al. 2007). Computer-aided simulations suggested that a magnetic flux gradient of $\nabla B > 100 \text{ Tm}^{-1}$ was necessary for targeting the magnetosols. They achieved this by placing the tip of a customized electromagnet over the right lobe of female BALB/c mice during inhalation. They showed enhanced deposition of MNPs in the targeted regions of the lungs wherein the amount of MNPs deposited in the right (targeted) lung was increased by a factor of 8 relative to the untargeted (left) lung. Additionally, histological evaluation demonstrated no disadvantageous effect on lung function from the magnetosols with- or without application of magnetic field.

The Rudolph group also published a recent study where they delivered magnetic aerosols containing model drugs to BALB/c mice via voluntary inhalation of nebulized liquid droplets (Hasenpusch, Geiger et al. 2012). In this work, the authors used mathematical simulations to optimize a portable magnet consisting of four identical

magnets arranged in a quadupole and then attached this magnet to the chest of the mice during inhalation. This quadupole resulted in a magnetic field of 0.2 Telsa and a magnetic gradient of 140 Tm^{-1} 2 mm from the surface of the magnet, which is the distance they estimated between the animals' chest and the lung tissue. After inhalation, the MNP-content in the lungs was determined using a previously reported method of magnetrelaxometry (Dames, Gleich et al. 2007) as well as a colorimetric determination of non-heme, and both methods revealed a 2.1-fold increase in the targeted right lung of the animals relative to the untargeted left lung (no difference was observed when inhalation was administered in the absence of a magnetic field). Additionally, a plasmid DNA (coding for the reporter gene *luciferase*) was complexed with 25 kDa PEI and added to the pre-nebulized aerosol suspension. The *in vivo* bioluminescence was measured 24 hours after inhalation (using an IVIS-100 system) and the transgene expression is illustrated in Figure 2.3.

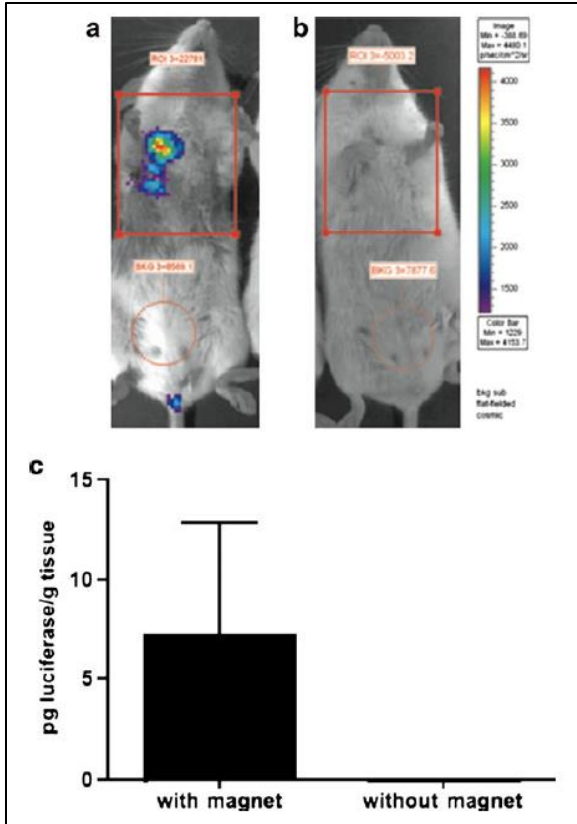


Figure 2.3: A nanomagnetsol solution comprising PEI-pDNA gene vectors coding for the luciferase gene and SPIONs was nebulized to Balb/c-mice (n03) either with (a) or without (b) an external magnetic gradient field applied to the right chest. Twenty-four hours after nebulization luciferase activity in the lungs was measured using in vivo bioluminescence imaging in mice. The lungs were removed subsequently to conduct an ex vivo luciferase assay, revealing a mean luciferase expression of 7.2 pg luciferase per gram tissue in mice that had been exposed to a magnetic gradient and no luciferase in mice without a magnetic gradient during the nebulization procedure (c). Taken from reference (Hasenpusch, Geiger et al. 2012).

This image clearly shows luciferase expression in the targeted right lung of the mice (Figure 2.3a) and no detectable expression in the untargeted left lung (Figure 2.3b). Further, *ex vivo* quantification of luciferase (Figure 2.3c) quantitatively confirmed the findings of the bioluminescence imaging. In addition to enhanced deposition, histopathological analysis revealed no alterations in the lungs of mice after inhalation of magnetosols. These studies show the potential of MNPs in pulmonary delivery by confirming the ability to provide two levels of active targeting through inhaling MNPs directly to the lungs and magnetically guiding them for site-specific accumulation.

In addition to enhanced deposition, reports have indicated the possibility of improving the retention of MNPs by applying a magnetic field after deposition from aerosols (Ally, Amirfazli et al. 2006). Ally et al. reported the theoretical factors affecting the retention of the magnetic particles once they reach the lungs and compared their findings with *ex vivo* experiments. The focus of this study was the upper airways where the main mechanism of particle clearance is the mucociliary escalator, so their model focused on the ability of magnetic fields to aid in overcoming this clearance mechanism. Figure 2.4 illustrates the concept of this work schematically. Their results indicated that the viscosity of the mucus was the most important factor affecting the retention of the magnetic particles and illustrate the potential of magnetic fields to enhance retention of particles in within the lungs which are very efficient at eliminating particulate matter. Others have shown interest in enhancing mucus penetration of MNPs through magnetic field and were able to accomplish this in mucus models; however, they were unable to reproduce these results in actual mucus due to the highly rigid structures within the mucus mesh.

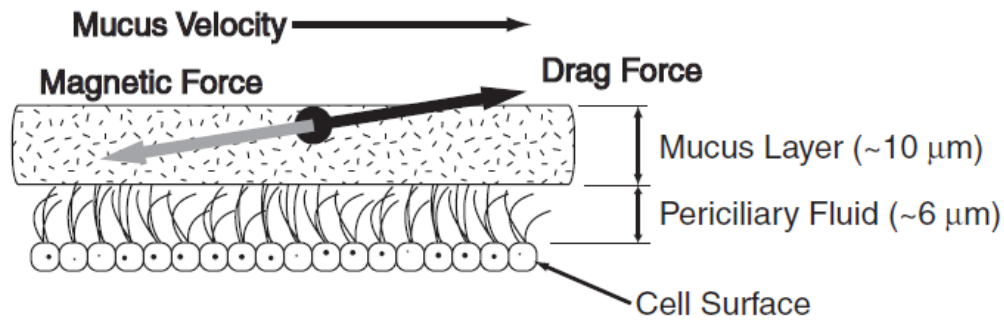


Figure 2.4: A nanomagnetsol solution comprising PEI-pDNA gene vectors coding for the luciferase gene and SPIONs was nebulized to Balb/c-mice (n03) either with (a) or without (b) an external magnetic gradient field applied to the right chest. Twenty-four hours after nebulization luciferase activity in the lungs was measured using in vivo bioluminescence imaging in mice. The lungs were removed subsequently to conduct an ex vivo luciferase assay, revealing a mean luciferase expression of 7.2 pg luciferase per gram tissue in mice that had been exposed to a magnetic gradient and no luciferase in mice without a magnetic gradient during the nebulization procedure (c). Taken from reference (Hasenpusch, Geiger et al. 2012).

2.7 Mucus Barriers and particle transport

Airborne particles delivered to the lungs via the pulmonary tract will first contact a layer of mucus or surfactant that covers the epithelial cell lining of this organ (Lai, Wang et al. 2009). In regions containing this mucus layer, particles intended to reach the underlying tissue must traverse a treacherous path consisting of physical and chemical hindrances to transport (Cone 2009). Additionally, the particles must be able to pass through this barrier in a timely fashion as the mucus layer is continually cleared by the

mucociliary escalator (Lai, Wang et al. 2009). Hence, regardless of the novelty and biocompatibility exhibited by a particulate drug delivery system, sufficient transport rates are necessary to ensure any therapeutic benefit.

When selecting a coating or additive, it is crucial to consider the barrier through which these particles must travel. Mucus is a common barrier to transport of colloidal drug delivery systems and covers sites such as the eyes, lungs, nose, vagina, and upper GI tract (Cone 2009). This viscoelastic fluid is very effective in trapping foreign particles and exists as a complex, heterogeneous, aqueous mixture of proteins, lipids, DNA, ions, cells, and cellular debris (Lai, Wang et al. 2009). The primary component of mucus is mucin, which forms a crosslinked network able to hinder the diffusion of foreign particles by physical and chemical means (Lai, O'Hanlon et al. 2007). Mucin fibers are connected end-to-end via disulfide linkages and the resulting pores in this network are on the nanometer scale (Sheehan, Kirkham et al. 2004, Lai, Wang et al. 2009). Additionally, these amphiphilic proteins trap both hydrophobic and hydrophilic particles through low-affinity interactions (Lai, Wang et al. 2009). Hence, selecting a system that minimizes these interactions will result in more effective transport of the particles.

Recently, it was shown that the use of a polymer coating enabled particles as large as 500 nm to traverse mucus at rates approaching unhindered diffusional transport as seen in a phosphate buffer solution (Lai, O'Hanlon et al. 2007). Hanes' group took a top-down approach at designing their coating by attempting to recreate the ability of relatively large viruses to efficiently transport through mucus (Olmsted, Padgett et al. 2001). Viruses minimize interaction with mucin fibers by an adhesion-preventing mechanism wherein their surfaces are densely coated with both positive and negative charges (Wada and

Nakamura 1981). Lai et al interpreted this quality as a highly hydrophilic yet net neutral surface and thus selected Poly(ethylene glycol) as a coating (Lai, O'Hanlon et al. 2007). Previously immobile polystyrene beads were shown to have diffusion coefficients only 4-6 fold less than in PBS after coating with PEG.

These reports of PEG increasing transport rates, however, contradicted previous reports that PEG was mucoadhesive so the authors investigated this matter further (Sahlin and Peppas 1997). Carboxylated polystyrene nanoparticles (NPs) were coated with PEG at varying molecular weights and classified as either mucoadhesive or mucoinert based on transport rates (Wang, Lai et al. 2008). Additionally, they studied the effect of the density of PEG surface coverage, which was indirectly measured as zeta potential (where neutral charge indicates complete coverage of PEG).

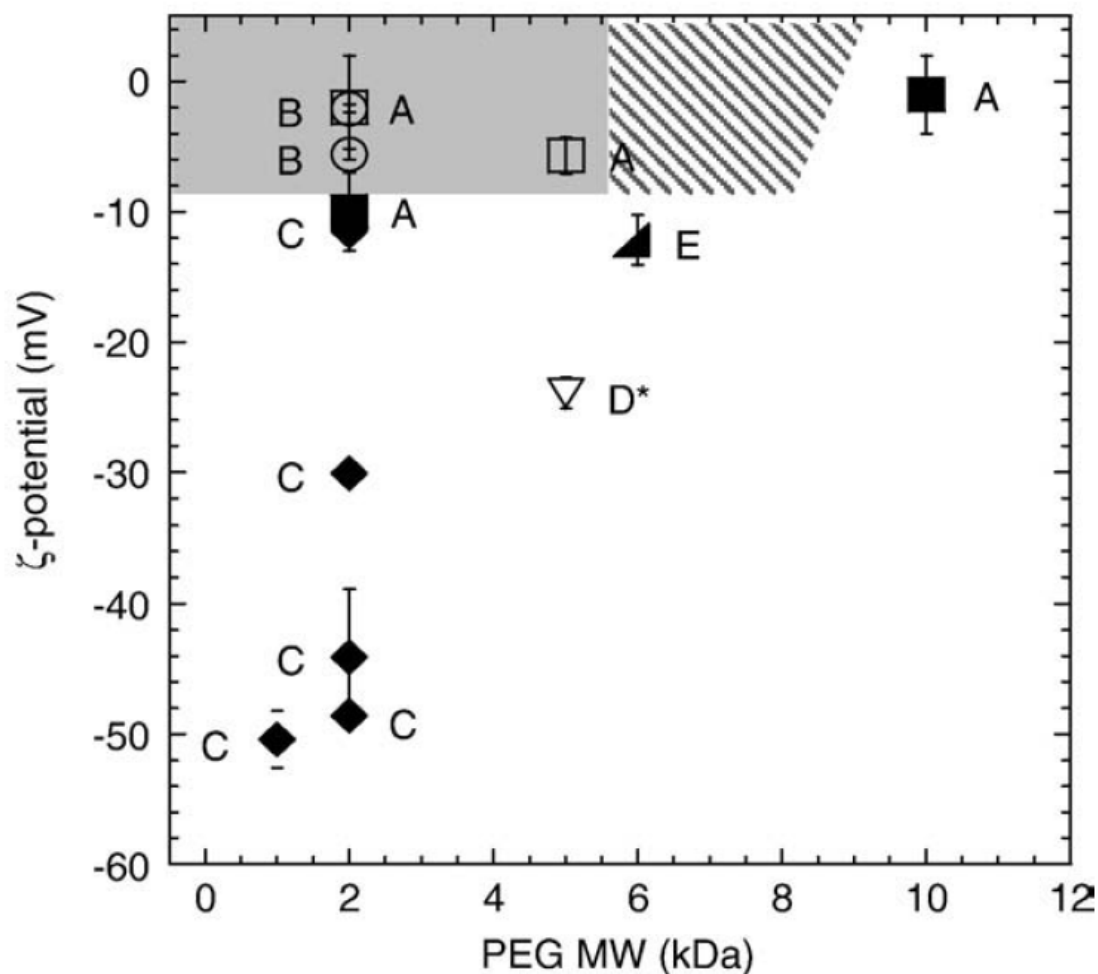


Figure 2.5: From reference (Wang, Lai et al. 2008). Mucoinert (open symbols) vs. Mucoadhesive (filled symbols) behaviour of nanoparticles figure.

Figure 2.5 shows a variety of particles reported to be mucoadhesive (filled symbols) along with those said to be mucoinert (open symbols). Results indicate that there is a specific range (shaded region) of PEG molecular weight and surface coverage for which the coated nanoparticles are mucoinert. Their hypothesis is that by increasing the molecular weight of PEG increases (and thus the hydrophilicity of the particles) the

particles avoid hydrophobic interactions with the mucin network, and the high surface coverage of PEG (low zeta potential) minimizes electrostatic interactions. They reasoned that PEG's mucoadhesive properties, at higher MW PEG moieties, are due to physical entanglement between PEG chains and mucin fibres. These reports illustrate the complexity of engineering a system that allows particles to effectively transport through the mucus barrier.

Another example of hindered transport is oral administration of proteins such as insulin (Chen, Sonaje et al. 2011). The layer of endothelial cells lining the walls of the upper GI tract is a very effective barrier to passive transport of molecules larger than 500-700 Da (Chen, Sonaje et al. 2011, Muller 2011). Additionally, proteins often require colloidal encapsulation as some reports indicate that 94-98% of orally administered proteins are digested by GI proteases (Ganapathy, Gupta et al. 2006, Muller 2011). Hence, an effective oral protein delivery system requires supramolecular particles to navigate, or facilitate passage of proteins, to and through the intestinal epithelium in order to reach the underlying blood vessels.

Sonaje et al. reported an insulin oral bioavailability of $15.1 \pm 0.9\%$ by encapsulating insulin in pH-responsive poly- γ -glutamic acid (γ -PGA) and chitosan (CS) nanoparticles (Sonaje, Lin et al. 2010). Chitosan, a cationic polysaccharide, was chosen because of its ability to increase paracellular permeability through the opening of tight junctions between adjacent cells (Ranaldi, Marigliano et al. 2002, Sonaje, Lin et al. 2010). Positively charged γ -PGA was incorporated as an additive to facilitate ionic gelation resulting in nanoparticles approximately 200 nm in diameter. As the particles travel down the GI tract the increasing pH reduces the interaction between γ -PGA and

CS. At high enough pH, the particles become unstable and disintegrate releasing preloaded insulin.

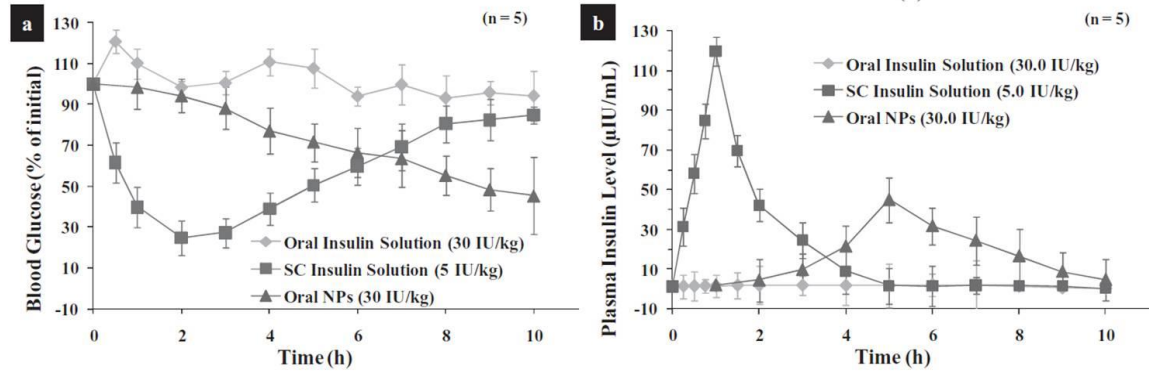


Figure 2.6: From reference (Sonaje, Lin et al. 2009). Behaviour of oral (◆) and subcutaneous (■) insulin solution and insulin-loaded nanoparticles (▲) in diabetic rats.

Animal studies were performed on diabetic rats to confirm or dispute the efficacy of the NPs *in vivo* and determine the oral bioavailability. Figure 2.6 shows an increase in the plasma insulin level (a) and the corresponding decrease in blood glucose level (b) for the NPs after oral administration. These results indicate that the insulin released remained in its active form. This was also confirmed by circular dichroism spectroscopy, which revealed no significant change in the conformation of insulin released compared with the standard insulin.

Chapter 3 Formulation and Characterization of Inhalable Magnetic Nanocomposite Microparticles (MnMs) for Targeted Pulmonary Delivery via Spray Drying

Inhalable composites for targeted pulmonary delivery of iron oxide (Fe₃O₄) magnetic nanoparticles (MNPs) to the lungs were formulated through spray-drying. The resulting aerodynamic performance of these composites as well as the activity of the MNPs released upon dissolution was important considerations. The goal was to controllably incorporate MNPs into powders with adequate aerodynamic performance and to be able to release unhindered MNPs that retain their ability to remotely heat in the presence of an alternating magnetic field. The chapter is taken directly or adapted from work **published** in **Stocke et al. (2014)** Copyright 2014 Elsevier B.V. Used with permission from Nathanael A Stocke, Samantha A. Meenach, Susanne M. Arnold, Heidi M. Mansour, and J. Zach Hilt.

3.0 Abstract

Targeted pulmonary delivery facilitates the direct application of bioactive materials to the lungs in a controlled manner and provides an exciting platform for targeting magnetic nanoparticles (MNPs) to the lungs. Iron oxide MNPs remotely heat in the presence of an alternating magnetic field (AMF) providing unique opportunities for therapeutic applications such as hyperthermia. In this study, spray drying was used to formulate magnetic nanocomposite microparticles (MnMs) consisting of iron oxide MNPs and D-mannitol. The physicochemical properties of these MnMs were evaluated and the in vitro aerosol dispersion performance of the dry powders was measured by the

Next Generation Impactor[®]. For all powders, the mass median aerosol diameter (MMAD) was $<5 \mu\text{m}$ and deposition patterns revealed that MnMs could deposit throughout the lungs. Heating studies with a custom AMF showed that MNPs retain excellent thermal properties after spray drying into composite dry powders, with specific absorption ratios (SAR) $> 200 \text{ W/g}$, and *in vitro* studies on a human lung cell line indicated moderate cytotoxicity of these materials. These inhalable composites present a class of materials with many potential applications and pose a promising approach for thermal treatment of the lungs through targeted pulmonary administration of MNPs.

3.1 Introduction

Targeted pulmonary inhalation aerosol delivery facilitates the direct application of bioactive materials to the lungs in a controlled manner. Medical conditions such as asthma, chronic obstructive pulmonary disease (COPD), and pulmonary infections secondary to cystic fibrosis employ targeted pulmonary inhalation aerosol delivery as a first-line treatment because of inherent advantages (Dolovich, Ahrens et al. 2005) such as a fast onset of pharmaceutical action, higher local concentrations of drugs, and reduced systemic side effects (Patton and Byron 2007). Further, the treatments of pulmonary diseases with inhalation methods avoid first-pass metabolism of pharmaceutical agents (Mansour, Rhee et al. 2009) resulting in significantly less drug required for aerosol dosage forms to exert a therapeutic effect in the lungs.

Dry powder inhalation aerosol offers several advantages over liquid aerosol formulations such as increased stability and sterility of formulations as well as controllable particle size for targeting regions of the lung (Dolovich, Ahrens et al. 2005).

Additionally, dry powder formulations can be used to administer higher amounts of water insoluble pharmaceutical actives as in contrast to liquid-based inhalation aerosol systems such as nebulizers and pressurized meter dose inhalers (pMDIs).

Recently, there has been a growing interest in utilizing the advantages of pulmonary delivery for treating lung diseases such as cystic fibrosis (CF) and lung cancer thereby expanding the potential applications of successful aerosol formulations. Phase I trials of inhaled cisplatin showed no dose-limiting toxicity or maximum tolerated dose (Wittgen, Kunst et al. 2007) and a phase II study of inhaled doxorubicin showed a favorable median survival compared to intravenous administration (Otterson, Villalona-Calero et al. 2010). Traditionally, inhaled therapies such as these utilize aerosols consisting of small molecule drugs and excipients; however, targeted pulmonary delivery provides a platform for localizing novel multifunctional nanoparticles to the lungs through direct, topical application (Azarmi, Roa et al. 2008, Mansour, Rhee et al. 2009).

The concept of delivering iron oxide MNPs¹ to the lung for drug delivery purposes has been explored recently due to their unique properties that provide novel functionality to drug delivery systems as well as their FDA approval as marketed pharmaceutical products for medical applications such as a contrast agent in magnetic resonance imaging (MRI) (Pankhurst, Connolly et al. 2003, Dames, Gleich et al. 2007, Frimpong and Hilt 2010, Xie, Zeng et al. 2010, Redman, Martin et al. 2011, McBride, Price et al. 2013, Sadhukha, Wiedmann et al. 2013, Verma, Crosbie-Staunton et al.

¹AMF: Alternating magnetic field; MMAD: Mass median aerosol diameter; MnM: Magnetic nanocomposite microparticle; MNP: Magnetic nanoparticle; NGI: Next generation impactor

2013). One such functionality is the magnetic guidance of aerosols containing MNPs for enhanced targeting to specific regions within the lungs. The Rudolph lab has successfully directed magnetic aerosols, as nebulized MNP suspensions, to regions of the lungs using magnetic fields (Dames, Gleich et al. 2007, Hasenpusch, Geiger et al. 2012). These studies show the ability to deliver a higher dose of model drugs to specific regions of the lungs and demonstrate one of the many potential advantages to incorporating multifunctional MNPs to inhalation therapies.

Additional advantages of using MNP-containing aerosols include their ability to remotely heat in the presence of an alternating magnetic field (AMF) providing enhanced control over actuating the onset of therapy (Satarkar and Hilt 2008, Satarkar, Biswal et al. 2010). In suspension, MNPs generate heat through frictional (Brownian) and magnetic (Néel) relaxation processes, and the heat generated from these particles can be used to trigger other therapies, increase transport of particles, and induce hyperthermia as a thermal treatment (Jordan, Scholz et al. 2006, McGill, Cuylear et al. 2009, Knecht, Ali et al. 2012, Li, ten Hagen et al. 2013).

Hyperthermia is the heating of tissue to 41-45°C and can be applied locally, regionally, or throughout the body. Additionally, it has shown promise in treating cancer by enhancing chemotherapy and radiotherapy (Vernon, Hand et al. 1996, Horsman and Overgaard 2007, Issels 2008). Locally targeted hyperthermia in the treatment of cancer has the advantage of reducing undesired cellular death to healthy tissue and can be accomplished with MNPs under AMF exposure (Jordan, Scholz et al. 1999, Frimpong and Hilt 2010, Meenach, Hilt et al. 2010, Satarkar, Meenach et al. 2011). Previous clinical trials have utilized magnetic nanoparticles under AMF exposure to demonstrate

the feasibility of remotely administering interstitial heating to cancer patients (Jordan, Scholz et al. 2001, Johannsen, Thiesen et al. 2010). Hence, delivering MNPs directly to the lungs through inhalable carriers could allow for targeted administration of hyperthermia in the treatment of lung cancer provided these carriers have appropriate aerodynamic properties. However, the introduction of foreign matter such as MNPs to the lungs poses safety risks to the patient, thus necessitating toxicological evaluation.

Previous *in vitro* toxicity studies with fluorescent iron oxide MNPs showed no pulmonary toxicity in murine alveolar macrophages for concentrations as high as 1000 µg/ml. However, *in vivo* studies on adult male Wistar rats showed general and organ toxicity after intratracheal administration of iron oxide nanoparticle suspensions at a low and high dose of 1 and 5 mg/ kg, respectively (Kwon, Kim et al. 2009, Szalay, Tatrai et al. 2012). Additionally, the effect on body weight, as well as liver and kidney weight, indicated systemic spreading of these particles through the systemic circulation.

The objectives of this work are to formulate composite dry powders for inhalation aerosol delivery containing multifunctional nanoparticles for the future development of novel pulmonary treatments. In this study, spray drying in closed-mode was used to formulate magnetic nanocomposite microparticles (“MnMs”) consisting of iron oxide MNPs and D-mannitol, which is an FDA-approved pharmaceutical excipient shown to be well tolerated for dry powder inhalation (Gjoerup, Hilberg et al. 2012). Figure 3.1 provides a schematic representation of the formulation and applicability of these materials. The physicochemical properties of these inhalable dry powders were thoroughly characterized with a variety of techniques and their *in vitro* aerosol performance was studied with the Next Generation Impactor®. The capability of these

materials to remotely heat in the presence of an AMF was examined and the *in vitro* cytotoxicity of these materials was examined in a human lung cell line (A549).

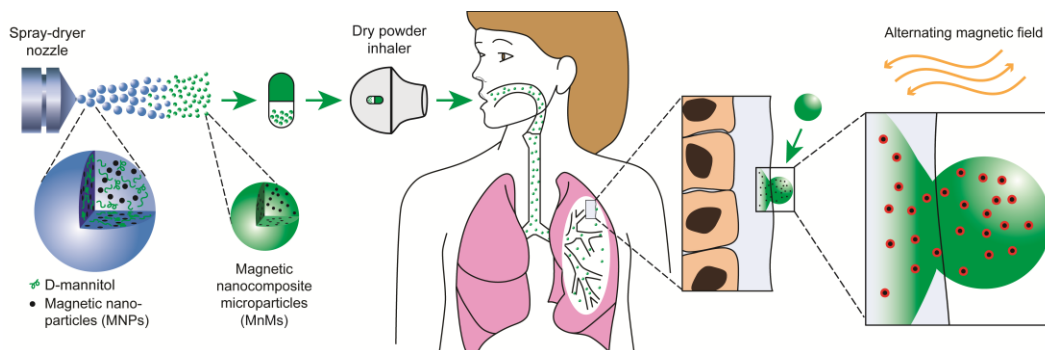


Figure 3.1: Schematic representation of the formulation and application of magnetic nanoparticle microcomposites (MnMs). From left to right we see the initial formation of these inhalable dry powders through spray-drying a feed consisting of iron oxide MNPs dispersed in a D-mannitol solution of methanol. Upon collection these materials were loaded into a capsule and placed into a dry powder inhaler for *in vitro* aerosol dispersion performance studies in order to model their predictive deposition patterns in the lungs. Finally, the heating properties of the MNPs released from these MnMs upon dissolution were verified by exposing them to an alternating magnetic field.

3.2 Material and methods

3.2.1 Materials

Iron(II) chloride tetrahydrate ($\text{FeCl}_2 \cdot 4\text{H}_2\text{O}$), iron(III) chloride hexahydrate ($\text{FeCl}_3 \cdot 6\text{H}_2\text{O}$), and D-mannitol were obtained from Sigma Aldrich (St. Louis, MO). Chloroform, anhydrous methanol, and high performance liquid chromatography-grade methanol were purchased from Fisher Scientific (Pittsburgh, PA). Ultrahigh-purity nitrogen gas was from Scott-Gross (Lexington, KY), and ammonium hydroxide

(NH₄OH) was obtained from EMD chemicals (Gibbstown, NJ). Honeywell Riedel-de Haen® Hydranal®-Coulomat AD, reagent for Karl Fischer (KF) coulometric titration, was purchased from Sigma-Aldrich (St Louis, MO). Special anhydrous AQUA STAR methanol for moisture determinations was purchased from EMD Chemicals, Inc. (Darmstadt, Germany)

3.2.2 Synthesis of iron oxide magnetic nanoparticles (MNPs)

Aqueous co-precipitation was used to synthesize iron oxide nanoparticles. Briefly, FeCl₂·4H₂O (Fe²⁺) and FeCl₃·6H₂O (Fe³⁺) salts were dissolved in 40 mL of deionized (DI) water at a 2:1 Fe³⁺:Fe²⁺ molar ratio. The solution was sonicated in a water bath for approximately 20 min and transferred to a 3-neck 500 mL round bottom flask. The round bottom flask was heated to 85°C under nitrogen flow with a mechanical stirrer at 300 rpm. Once the vessel reached 85°C, 5 mL of NH₄OH (28 % w/w) was added with a syringe and the reaction was carried out for 1 hour. Recovered particles were washed with ethanol via magnetic decantation and dried in a vacuum oven prior to spray drying.

3.2.3 Formulation of magnetic nanocomposite microparticles (MnMs) with spray drying

Spray drying was accomplished with a Büchi Mini Spray Dryer B290 coupled with a B-295 Inert Loop and high-performance cyclone (all from Büchi Labortechnik, Flawil, Switzerland) using parameters previously optimized by our lab (Li and Mansour 2011). Spray drying experiments were carried out in closed mode using UHP dry nitrogen gas at a flow rate of 600 L/h, an inlet temperature of 150°C, and an aspirator rate of 35 m³/h. Once the inlet temperature of 150°C was reached, pure methanol was fed to

the spray dryer until the outlet temperature was stable and this temperature was recorded, as tabulated in Table 3.1. For feed mixtures, D-mannitol was dissolved in methanol and iron oxide MNPs were weighed out and subsequently dispersed such that the combined mass of these two components resulted in a dilute concentration of 0.1% wt/vol. The MF20 and MF5 powders resulted in a MNP concentration of 0.20 mg/ml and 0.05 mg/ml, respectively. Two liters of the feed mixture were fed to the spray dryer at a pump rate of 50% (15 mL/min) through a stainless steel nozzle with a diameter of 0.7 mm. For the MF20 and MF5 experiments, which contained MNPs, the feed mixture was sonicated throughout the experiment to insure adequate dispersion of MNPs. Powders were collected and transferred to a glass desiccator over Drierite™ and stored in the freezer at -23°C. Two different iron oxide loadings were incorporated into the powders and Table 3.1 summarizes these systems and their spray drying parameters.

Table 3.1: Summary of experimental conditions for inhalable dry powders.

System	Initial MNPs (wt%)	Inlet T (°C)	Outlet T (°C)
MF20	20%	150	67
MF5	5%	150	58
MF0	0%	150	70

3.2.4 Electron microscopy

Scanning transmission electron microscopy (STEM) was carried out in order to confirm the presence of iron oxide in the MnMs and to observe the spatial distribution of

the nanoparticles within the composites. Powders were dispersed in chloroform at 100 µg/ml, added dropwise onto a support film grid (Electron Microscopy Sciences, Hatfield, PA), and allowed to dry overnight in a desiccator over Drierite™. Chloroform was used as a dispersant because D-Mannitol is practically insoluble in this organic solvent (Pena, Daali et al. 2000). Images were captured with a JEOL 2100F Field Emission Electron Microscope (JOEL, Tokyo, Japan) equipped with an Oxford EDS detector (Oxford Instruments, Oxford, United Kingdom).

Scanning electron microscopy (SEM) was performed in order to observe the particle size, surface roughness, shape and morphology. A Hitachi S4300 microscope (Tokyo, Japan) was used to capture images. Double-sided adhesive carbon tabs were adhered to aluminum studs (Ted Pella, Redding, CA) and blotted on weigh paper with our dry powder. These samples were coated with a thin film of a gold/palladium alloy using an Emscope SC400 sputter coating system at 20 mA for 2 minutes under argon gas. For all electron microscopy experiments at least 3 independent samples were examined and multiple images were examined for each sample.

3.2.5 Thermal gravimetric analysis (TGA)

Thermal gravimetric analysis was performed using a TA TGA Q50 (TA Instruments New Castle, DE) in order to quantify the actual MNP loading in the powders. Samples were placed in a Tzero™ alodined aluminum pan that was hermetically sealed and then placed into the furnace along with an empty alodined aluminum hermetically sealed reference pan. The temperature of the furnace was raised to 120°C at a rate of 5°C /min and then held isothermally for 20 minutes to remove any trace solvent. The

temperature was then increased to 500°C and held isothermally for 30 minutes in order to completely decompose any D-mannitol present and allow for calculating the actual mass of iron oxide nanoparticles in the dry powders. Experiments were carried out in triplicate

3.2.6 Karl Fischer titration

Karl Fischer coulometric titration was carried out in order to determine the residual water content in the powders. A 737 KF Coulometer coupled with 703 Ti Stand (Metrohm Ltd., Antwerp, Belgium) was used. Approximately 5 mg of these powders were dissolved into anhydrous methanol for moisture determinations and allowed to sonicate for approximately 10 minutes to ensure complete dissolution of composites thereby releasing the MNPs into suspension. The resulting dispersions were injected into reaction cell filled with Hydranal[®] KF reagent with a 2 mL syringe and the amount of water injected was measured. Pure solvent was also injected to determine the amount of residual water in the solvent. The mass of water in the injected samples was used to calculate the water content in the dry powders by subtracting out the water content of the solvent.

3.2.7 Differential scanning calorimetry (DSC)

DSC was carried out in order to determine the thermal phase transitions of the dry powders. An Auto Q20 Differential Scanning Calorimeter equipped with an RSC-90 refrigerated cooling system (TA Instruments-Waters LLC, New Castle, DE) and Tzero[™] technology was used for measurements. Approximately 2 mg of sample was weighed into a Tzero[™] alodined aluminum pan that was hermetically sealed and then placed into

the furnace along with an empty alodined aluminum hermetically sealed reference pan. The temperature was initialized at 0°C and subsequently raised to 250°C at a rate of 5.00°C /min.

3.2.8 X-ray powder diffraction (XRPD)

XRPD was used to examine the long range order of the MnMs. Powders were analyzed by an X-ray diffractometer (Multiplex, Rigaku) with Cu K α radiation (40 kV, 44 mA) in order to examine their crystallinity. Scans were obtained from 5 to 60° 2 θ with step size of 0.2 and scan rate of 2 °/min.

3.2.9 Particle size analysis

Dynamic Light Scattering (DLS) was performed to determine the hydrodynamic diameter of the MNPs before spray drying and after being released by dissolution of the MnMs. Aqueous dispersions were made with a MNP concentration of 200 μ g/mL and were read in a disposable cuvette using a Beckman Coulter® Delsa Nano Submicron Particle Size and Zeta Potential Particle Analyzer (Beckman Coulter, Brea, California). For these experiments, MNPs from the same synthesis batch were compared in order to examine the effects of spray drying on particle diameter and avoid observing batch-to-batch variability as seen in precipitation reactions.

SigmaScan® 5.0 software (Systat, SanJose, CA) was used to analyze SEM images and digitally determine the mean size and standard deviation of MnMs. Representative SEM images at a magnification of 5000x were analyzed by measuring the diameter of at least 100 particles per image with the SigmaScan software.

3.2.10 In vitro aerosol dispersion performance with the Next Generation Impactor™ (NGI™)

Impactor studies were carried out with a M170 Next Generation Impactor™ (MSP Corporation Shoreview, MN) in accordance with United States Pharmacopeia (USP) Chapter <601> specifications on aerosols (2006). The conditions for these experiments were previously reported (Meenach, Vogt et al. 2013, Wu, Zhang et al. 2013). The NGI was equipped with a stainless steel induction port (USP throat adaptor) attachment and specialized stainless steel NGI™ gravimetric insert cups (NGI Model 170, MSP Corporation, Shoreview, Minnesota). Type A/E glass fiber filters with diameter 55mm (Pall Corporation, NY) were placed on each stage of the impactor and weighed before and after the experiment to determine the particle mass deposited. Approximately 10 mg of powder was loaded into each clear hydroxypropyl methylcellulose, size-3 capsule (Quali-V®) (QUALICAPS, Spain) and these capsules were placed into a HandiHaler® DPI™ device (Boehringer Ingelheim Pharmaceuticals, Inc. Ridgefield, CT) attached to a customized rubber mouth piece connected to the NGI™. Three capsules were loaded and released for each sample and experiments were performed in triplicate. The total dose for each sample was approximately 30 mg. A Copley HCP5 vacuum pump (Copley Scientific, United Kingdom) and a Copley TPK 2000 critical flow controller (Copley Scientific, United Kingdom) were used to produce a flow rate (Q) of 60 L/min in order to model the flow rate in a healthy adult lung. This flow rate was adjusted before each experiment using a Copley DFM 2000 flow meter (Copley Scientific, United Kingdom).

For Q=60 L/min, the aerodynamic cutoff diameters (D_{a50}) for each stage of the impactor were given from the manufacturer as: stage 1 (8.06 μm); stage 2 (4.46 μm); stage 3 (2.82 μm); stage 4 (1.66 μm); stage 5 (0.94 μm); stage 6 (0.55 μm); and stage 7 (0.34 μm). The emitted dose (ED), respirable fraction (RF), and fine particle fraction (FPF) were calculated as follows:

$$ED \% = \frac{\text{Initial mass in capsules} - \text{Final mass in capsules}}{\text{Initial mass in capsules}} \times 100\% \quad (\text{Equation 3.1})$$

$$RF \% = \frac{\text{Mass of particles on stages 2-7}}{\text{Total particle mass on all stages}} \times 100\% \quad (\text{Equation 3.2})$$

$$FPF \% = \frac{\text{Mass of particles on stages 2-7}}{\text{Initial mass in capsules}} \times 100\% \quad (\text{Equation 3.3})$$

The mass median aerodynamic diameter (MMAD) and geometric standard deviation (GSD) for the particles were determined using a Mathematica® program written by Dr. Warren Finlay (Finlay 2008).

3.2.11 Alternating magnetic field (AMF) Heating studies

Heating studies were performed on synthesized MNPs as well as MNPs released from MnMs upon aqueous dissolution using a custom Taylor Winfield AMF source (Taylor-Winfield Technologies, Youngstown, Ohio). Pure MNPs (as synthesized) and MnMs were dissolved at a concentration of 10 mg/ml. Particles were dispersed in DI water, sonicated for approximately 20 min and placed in an oven at 25°C. 1 mL of these suspensions was transferred to a 2 mL centrifuge tube and placed inside the induction coil of the AMF source. The samples were heated at a field strength of approximately 55 kA/m and a frequency of 300 kHz for 5 minutes and a Luxtron FOT Lab Kit® (LumaSense Santa Clara, CA) was used to monitor the temperature of the suspension.

The specific absorption rate (SAR) is a calculation that normalizes the heating curve to the concentration of MNPs and indicates the ability of the MNPs to heat. SAR values were calculated for these data using equation 34:

$$SAR = \frac{\sum c_i m_i}{m} \frac{dT}{dt} \quad (\text{Equation 3.4})$$

where m_i , C_i , are the mass and specific heat capacity of component i, respectively. The ratio dT/dt was determined as the slope of a linear trendline over a 30 second time interval in the initial linear region of the heating curve. The mass of iron oxide, m , for the MF20 and MF5 powders was calculated using results from TGA experiments.

3.2.12 Cytotoxicity tests

Human A549 alveolar epithelial adenocarcinoma cells were purchased from American Type Culture Collection (Manassas, VA, USA). Cells were cultured in 75 cm² flasks in Dulbecco's modified eagle medium (DMEM) containing 10% FBS, 5% PSTREP, and 1% Fungizone at 37C in a humidified incubator with 5% CO₂. For viability studies, A549 cells were seeded into 96-well plates at 10,000 cells/cm², placed in an incubator at 37°C and allowed to attach overnight. Cells were subsequently exposed to varying concentrations of MnMs dispersed in DMEM media for 24 hours at 37°C. Following exposure, live cells were stained with calcein AM, which is hydrolyzed to the fluorescent molecule calcein by intracellular esterases, and placed in a Biotek Synergy Mx microplate reader (Biotek, Winooski, VT) to measure the fluorescent intensity. Relative viability was calculated as the ratio of the mean fluorescence intensity to that of the control, which contained media only. For each experiment 10 wells were

used for each concentration and experiments were performed in triplicate therefore and the statistical analysis was performed with N=3.

3.2.13 Statistics

All experiments were performed in at least triplicate. The aerosolization studies were experimentally designed by Design Expert™ 8.0.7.1 software (Stat-Ease Corp., MN, USA). SigmaPlot 12.3 was used for one-way ANOVA tests and when statistically difference was observed a Holm-Sidak test was used to determine any significance in observed data. A p-value of <0.05 was considered statistically significant.

3.3 Results and Discussion

3.3.1 Physiochemical characterization

Magnetic nanocomposite microparticles (MnMs) were successfully formulated via spray drying and Figure 3.2 shows representative SEM images of the MnM powders. All particle systems displayed smooth and spherical particle morphologies, which are important for optimal aerodynamic performance. Additionally, these images show a relatively uniform size distribution of the particles, which was confirmed by measuring the geometric diameter of MnM particles with SigmaScan® (Table 3.2). Representative STEM images of the MnMs show the successful loading of MNPs (Figure 3.3) via spray drying thereby confirming our hypothesis that composite powders containing novel magnetic nanoparticles can be formulated via spray drying in closed-mode. The presence of MNPs within composite dry powders is evident as areas of higher contrast (brighter regions) and energy dispersive X-ray spectroscopy confirmed these findings (data not

shown). The MF20 powder (Figure 3.3a) shows the highest amount of MNPs and thereby confirms our ability to tailor the amount of MNPs loaded into these novel composites, which would be necessary in the further development of these composites for specific medicinal applications. These images illustrate the ability to load large quantities of MNPs into spray dried composites and suggest no change in particle shape or morphology. Additionally, these images show that MNPs are dispersed relatively uniformly throughout the MnMs and suggests the spray drying process does not form large MNP aggregates and this was subsequently confirmed with DLS.

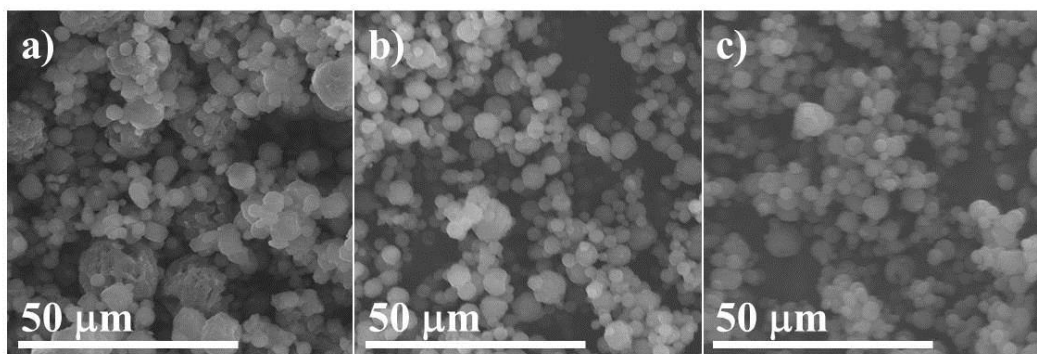


Figure 3.2: SEM images of a) MF20, b) MF5, and c) MF0 dry powders. Magnification 5,000x.

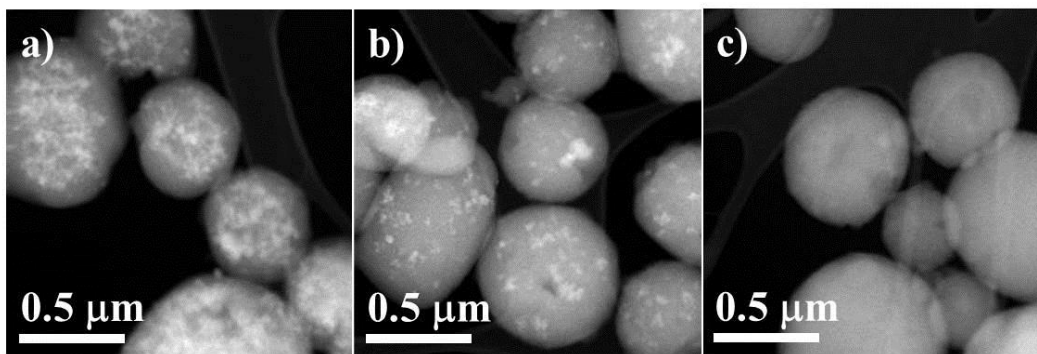


Figure 3.3: TEM images of a) MF20, b) MF5, and c) MF0 dry powders.

DLS, Karl Fisher titration, and TGA were carried out to evaluate the diameters of MNPs released from the composite particles, water content of the powders, and MNP loading in MnMs, respectively. Table 3.2 summarizes the data from these experiments. DLS was used to measure the hydrodynamic radii of the MNPs before incorporation into MnMs and after release from composites via aqueous dissolution. The diameter of the iron oxide MNPs before incorporation into MnM composites was 145.7 ± 2.9 nm. After spray drying into MnMs, the diameters of the MNPs in the MF20 and MF5 powders were 159.0 ± 3.8 nm and 144.2 ± 4.5 nm, respectively. These data confirmed minimal differences in the particle diameters of the MNPs released from composites and confirms the absence of agglomerate formation during the formation of MnMs with spray drying. Importantly, these results show the ability to incorporate our MNPs into composite powders for inhalation without losing the advantageous properties associated with their small size. Karl Fisher titration demonstrated that the various MnM powders have low residual water content which is optimal for aerodynamic performance and illustrate that these powders can be stored in such a way to avoid water vapor uptake and the associated complications such as agglomeration due to increased interparticulate interactions. It is interesting to observe that MF20 powders showed a higher mean residual water content than MF5 although this difference was not statistically significant. Additionally, the variability in the water content was much higher for the MF20 powder and this could be due to residual water present on the MNPs before spray drying. TGA allowed for the quantification of MNP loading in the MnMs and revealed slightly higher loading values in the final spray dried particles than in the initial feed conditions; however, the MNP loading was relatively consistent from batch-to-batch. The increased loading of iron oxide in the final

particles is likely due to smaller particles (<300 nm) continuing to the filter of the spray drying system and thus not reaching the sample collection vial. Additionally, particles containing more MNPs have a higher density and therefore a larger aerodynamic diameter leading to higher probability of collection.

Table 3.2: MnM and MNP diameters, MNP loadings, and water content of MnMs.

System	MNP Diameter (nm)	MnM Diameter (nm)	MNP_{feed} (wt%)	MNP_{actual} (wt%)	Water Content (wt%)
MF20	159.0 ± 3.8	851 ± 505	20	27.8 ± 1.8	4.3 ± 4.0
MF5	144.2 ± 4.5	701 ± 280	5	13.3 ± 1.5	1.2 ± 0.6
MF0	n/a	770 ± 301	0	n/a	1.0 ± 0.6

DSC and XRPD were performed to observe thermal phase transitions and crystallinity of the MnM powders, respectively. Figure 3.4 shows the XRPD diffractograms for the MnMs with important peaks labeled. The representative peaks for iron oxide (Fe₃O₄) are marked with stars and representative peaks for the crystalline polymorphs of d-D-mannitol are marked with a diamond and cross, respectively (Burger, Henck et al. 2000, Fronczek, Kamel et al. 2003). The expected peaks for iron oxide are seen in the MF5 and, as expected, become much more intense in the MF20 due to higher MNP loading. The MF0 powder shows peaks from α and β polymorphs of D-mannitol and provides a good reference to see any change in crystallinity due to the incorporation of MNPs. As can be seen, the MF5 and MF20 powders contain the same peaks as MF0 but at different

relative intensities. As an example, it is observed that there is a change in the ratio of representative peaks for the α and β polymorphs at 2θ degree values of 13.6 and 14.5, respectively. It can be seen that the incorporation of MNPs into the spray dried composites results in a higher β -polymorph character of mannitol in the solid state. This increase in the amount of the β -polymorph demonstrates that the incorporation of iron oxide MNPs results in a polymorphic interconversion between the different crystalline polymorphs of D-mannitol. This also suggests that such phenomena should be closely monitored for future development of powders as conversion between crystalline polymorphs of a given material can lead to changes in its physical properties such as melting point and solubility among others, since polymorphs of the same material have different Gibbs free energy states. DSC thermograms (Figure 3.5) reveal an endothermic phase transition at approximately 165°C representing the melting point of D-mannitol which is in excellent agreement with its reported melting temperature (Burger, Henck et al. 2000). These findings indicate that these novel MnMs possess excellent thermal stability and suggest, metaphorically, that these MnMs will “melt in your lungs, not in your hands” (in actuality they will dissolve). These findings are important because they show that the storage of these systems is insensitive to temperature for practical purposes.

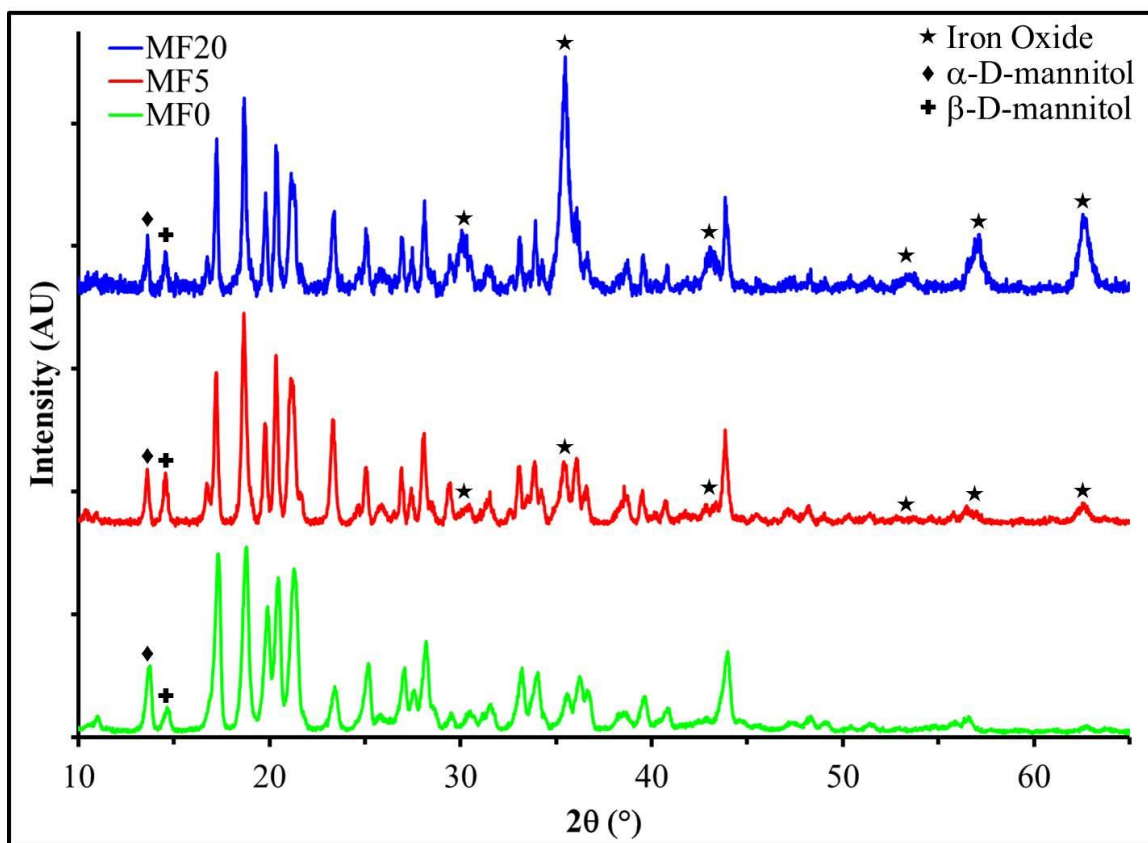


Figure 3.4: XRPD diffractograms for MnM powders.

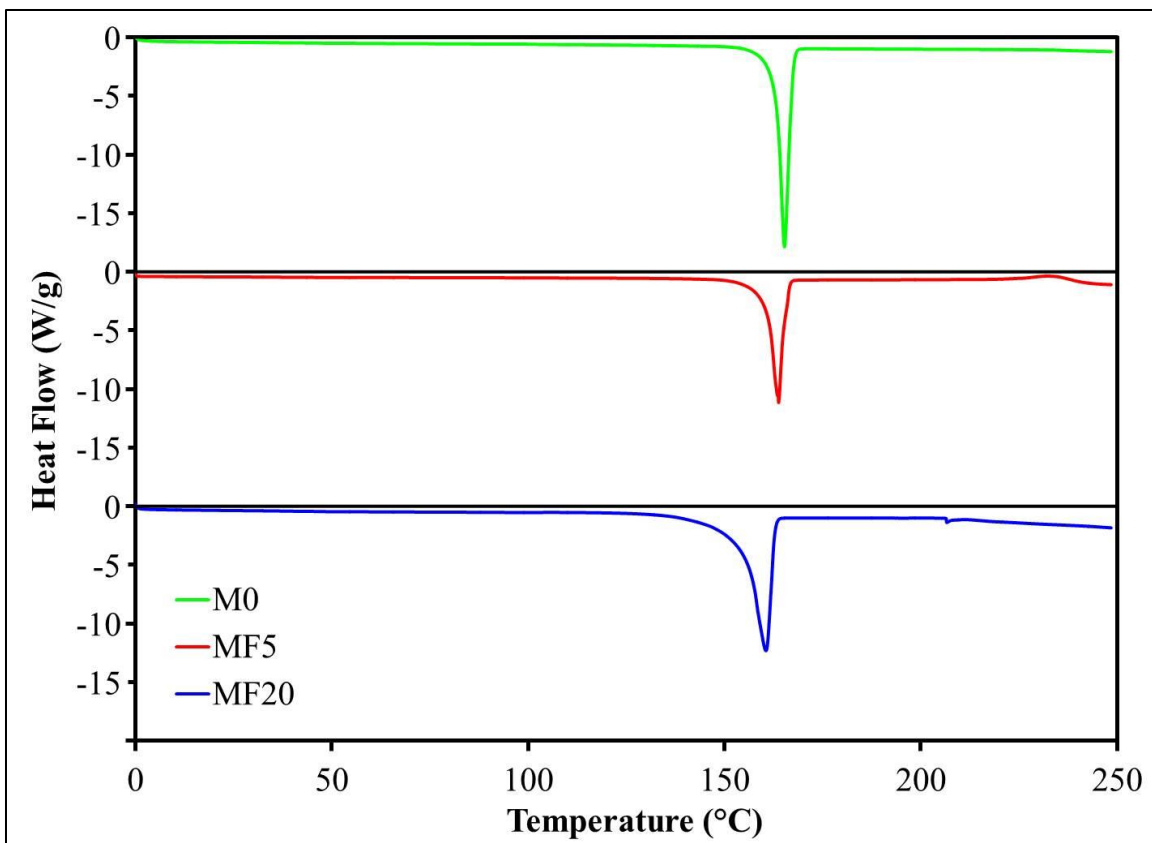


Figure 3.5: DSC thermograms for MnM powders.

3.3.2 Aerosol performance of MnMs

The MnM powders showed excellent aerosol performance thereby confirming that they are suitable for dry powder aerosol delivery. The aerosol performance of the MnMs (Figure 3.6) indicates a large number of the particles being deposited on all stages of the impactor for each powder system thereby illustrating the potential and the versatility of these formulations to reach all regions of the lungs. This would be advantageous for particular lung cancers such as bronchioloalveolar carcinomas, as well as for carcinomas occurring in the upper lung region (e.g. bronchial carcinoma) which can be targeted based on aerodynamic particle size based on the deposition on stage 1.

Specifically, particles below 10 microns but greater than 5 microns can effectively target the upper lung region of the bronchi and bronchials (Suarez and Hickey 2000). Additionally, these deposition patterns can be altered to shift the deposition pattern to more specific regions by changing processing variables in spray drying as well as by using other excipients (Suarez and Hickey 2000). Table 3.3 summarizes the aerosol performance parameters for each system. The fine particle fraction (FPF) and respirable fraction (RF) values for all of the powders were approximately 30% and 50%, respectively, which are higher than the 10-20% values of currently marketed dry powder inhalation (DPI) pharmaceutical products even in the absence of a lactose carrier (Suarez and Hickey 2000). Additionally, these powders all displayed high emitted doses of approximately 90% which demonstrates favorable dispersion efficiency. The mass median aerosol diameter (MMAD) was calculated for the aerosols produced from the MnM powders and all of these values were less than 5 μm suggesting their ability to adequately deposit throughout all regions of the lungs and effectively reach the lower airways. Interestingly, we see similar deposition patterns between MF5 and MF0 while the MF20 powder has slightly higher deposition on some of the earlier stages. This shift in deposition pattern is most likely due to the significant increase in the density of the composite particles as a result of such a high MNP-loading. Still, all three powders displayed good aerosol performance and these results suggest that these MnMs are suitable for DPI administration and suggest a new administration route for the delivery of iron oxide nanoparticles. Additionally, these findings propose a novel method for incorporating nanomaterials into composites that can subsequently be delivered to the

highly permeable tissue of the lungs assuming they can traverse the mucosal lining in regions where it exists.

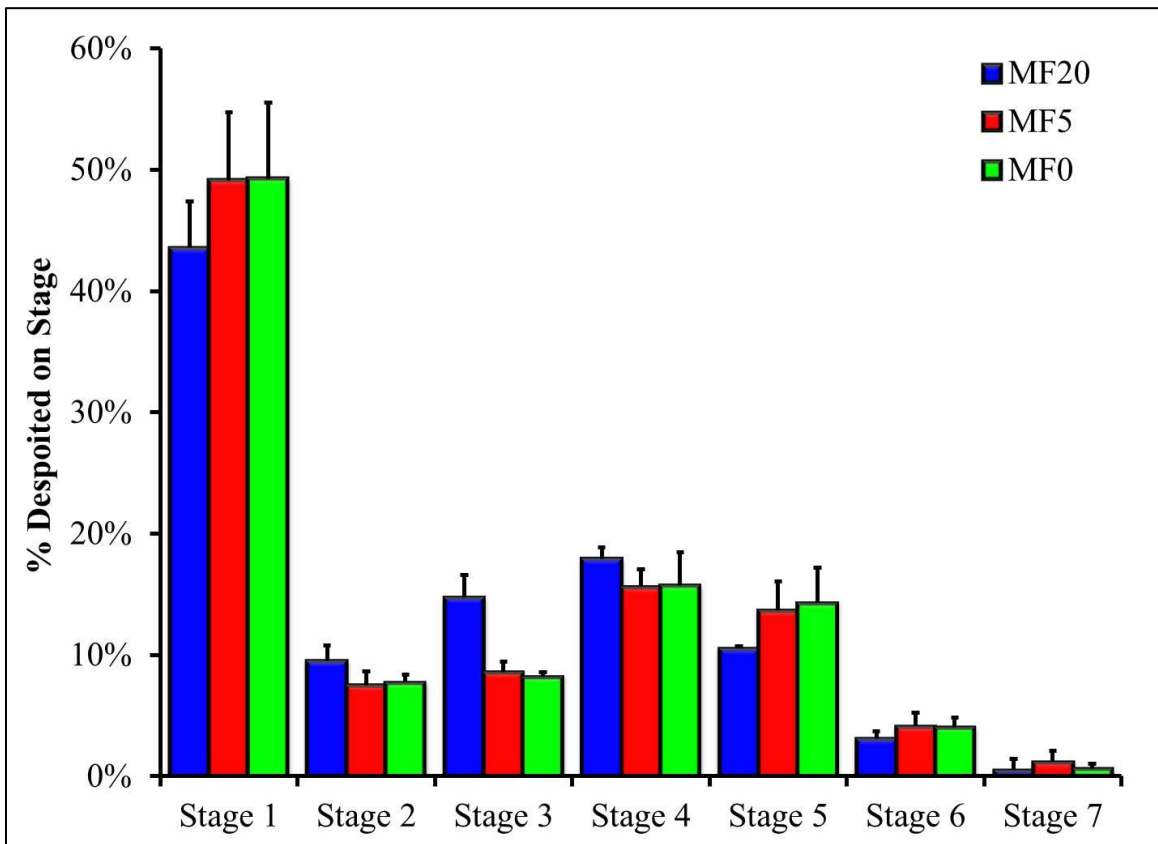


Figure 3.6: Aerosol dispersion performance plot for MnM powders using the NGI at 60 L/min.

Table 3.3: Aerosol performance properties for inhalable MnMs.

	<u>MF20</u>	<u>MF5</u>	<u>MF0</u>
MMAD (μm)	4.5 ± 0.2	4.5 ± 1.0	4.4 ± 1.0
GSD (μm)	2.4 ± 0.1	2.8 ± 0.1	2.7 ± 0.3
FPF (%)	34.3 ± 3.8	31.2 ± 2.0	29.6 ± 6.8
RF (%)	56.5 ± 3.8	50.9 ± 5.6	50.7 ± 6.3
ED (%)	92.0 ± 2.9	92.5 ± 2.9	88.0 ± 6.7

3.3.3 AMF heating of MNPs released from MnMs

Representative heating curves for the MnM systems are shown in Figure 3.7 and these data confirm that the MNPs retained excellent heating capabilities. Experiments were performed at room temperature and therefore illustrate that the temperatures reached for the MF20 powders are well above the hyperthermia range indicating sufficient heat for the intended goals. Additionally, the range of heating between the MF5 and MF20 powders suggests the ability to significantly change heating capability of these powders by altering the MNP loading. The SAR of the iron oxide MNPs before incorporation into MnM composites was 422 ± 18 W/g. After spray drying into MnMs, the SAR values for the MF20 and MF5 powders were 317 ± 51 W/g and 252 ± 53 W/g, respectively. These data illustrate that, although a drop in SAR was seen, the MNPs show excellent heating capability and these SAR values compare favorably with previous reports from our group (Wydra, Kruse et al. 2013). High SAR values suggest that

relatively low amounts of MNPs would be necessary to achieve elevated temperatures within a biological system where the losses would presumably be less.

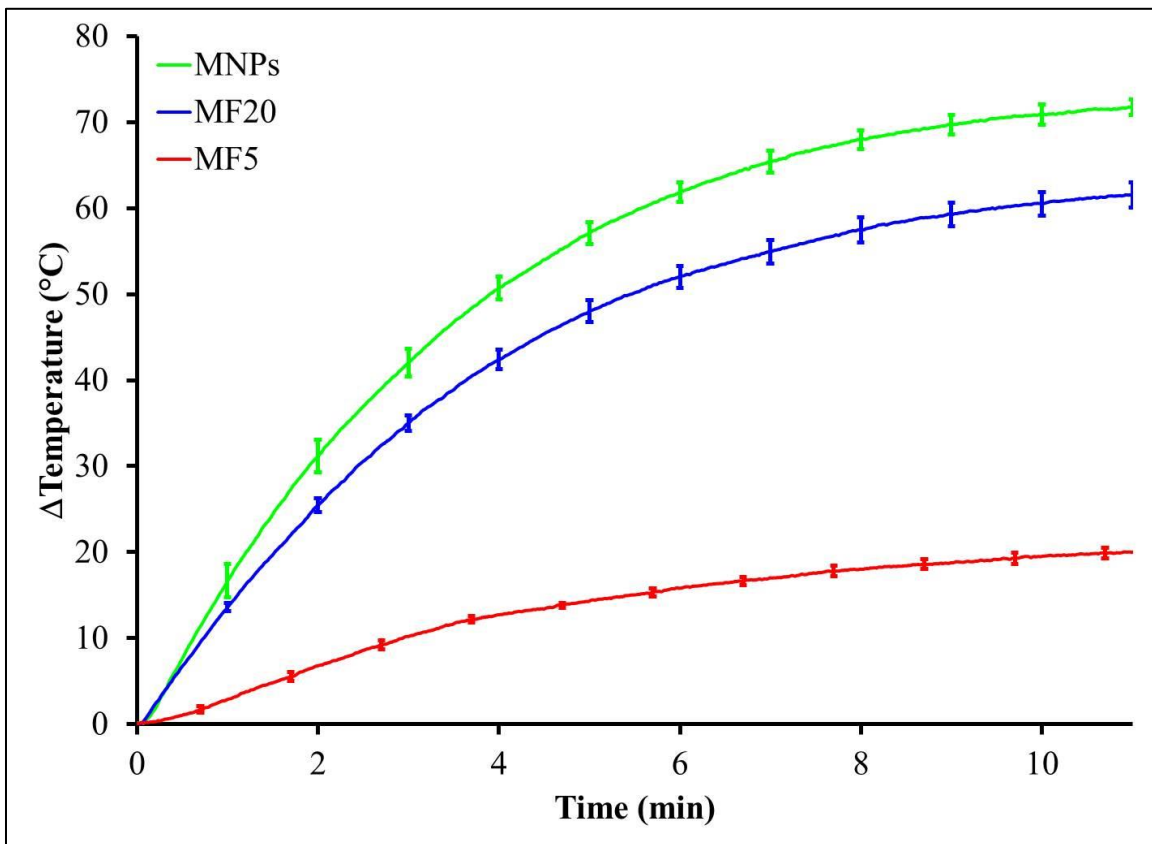


Figure 3.7: Heating curves for MnMs under AMF exposure

3.3.4 *In vitro* cytotoxicity of MnMs exposed to human lung cell lines

These MnMs deposit effectively *in vitro* on the stages of the NGI which can be modeled for predictive deposition in the alveolar lung region and in the smaller airways (bronchioalveolar region). Hence, it was of interest to test these powders on a human lung cell lines that represent these lung regions for application in lung cancer. Figure 3.8 shows the results from *in vitro* cytotoxicity studies on the A549 (human lung alveolar

epithelial (Type 1) adenocarcinoma) cells. These data reveal a slight decrease in cell viability for higher concentrations of the MnMs indicating moderate cytotoxicity of these materials in this concentration range. Future development of the MNPs incorporated to these MnMs could reduce the cytotoxic effect of these materials by coating them with biocompatible chemical moieties. These preliminary *in vitro* results suggest these materials have the potential to be safe when administered via inhalation aerosol delivery. Additionally, these results indicate that MnMs could provide a novel method of delivering targeted nanotherapy to the lungs in a safe and effective manner.

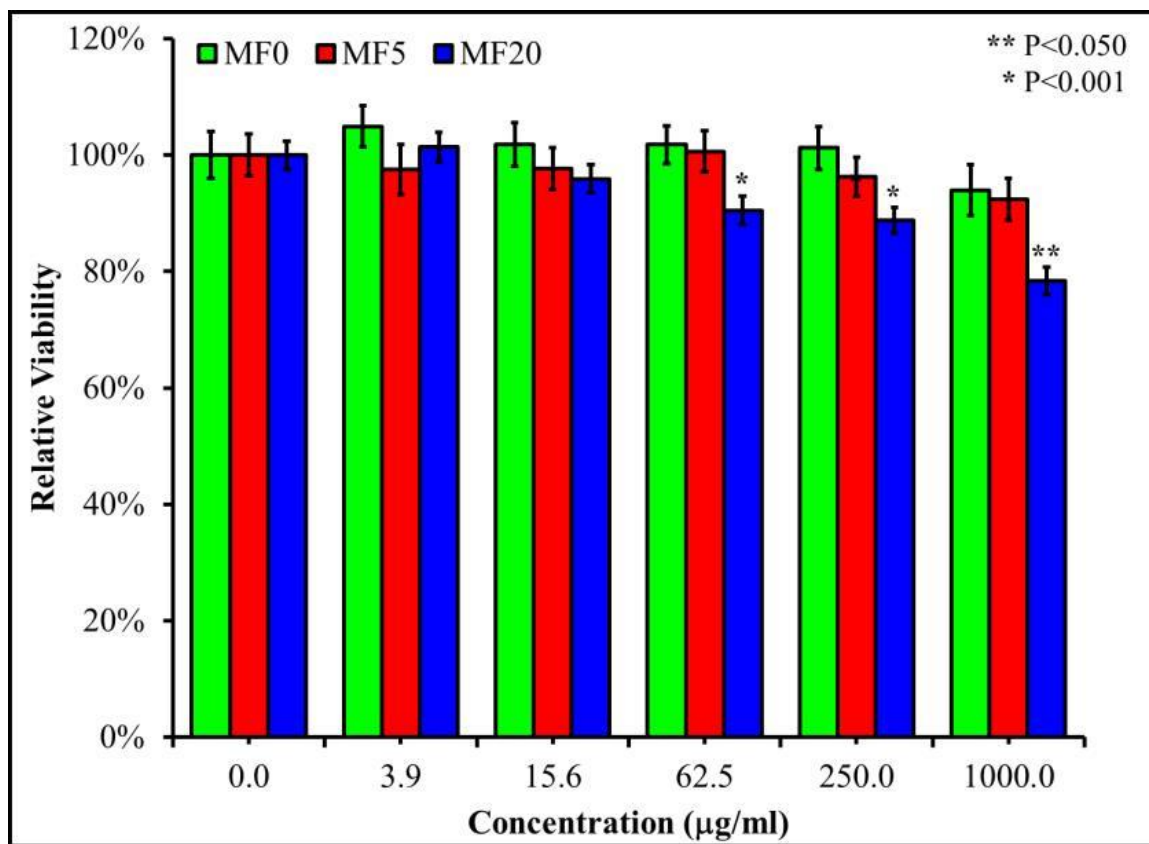


Figure 3.8: *In vitro* cytotoxicity results for human A549 alveolar epithelial adenocarcinoma cells after 24 hours of exposure to MnMs at 37°C.

3.4 Conclusions

Iron oxide MNPs were successfully incorporated into MnMs through spray drying in closed-mode. Physicochemical characterization of these composites revealed the potential to use these particles in the inhalation aerosol treatment of lung cancer via targeted hyperthermia. Aerosol performance studies revealed favorable aerodynamic properties for the MnM powders with FPF and RF values greater than 50% along with ED values around 90%. The MMADs for all aerosols delivered by a currently marketed DPI device were approximately 4.5 μm and the aerosol performance plots suggest the potential for high deposition of these particles throughout the lungs. Heating studies imply that these materials can be remotely heated after formulation and in vitro cytotoxicity studies show moderate toxicity on human lung A549 cells. These data provide initial evidence that these materials can potentially be targeted throughout the lung including the upper lung region for application in bronchial lung cancer and also in the mid-to-lower lung regions. Additionally, MnMs possess the ability to release MNPs that remotely heat in the presence of an AMF. These novel composites present an exciting class of materials with many potential applications and pose a promising approach to a novel thermal treatment of the lungs through targeted pulmonary inhalation aerosol delivery of MNPs.

**Chapter 4 Remote controlled thermal therapy with magnetic nanocomposite
microparticles induces cell death in triple negative breast cancer micrometastatic
tumor tissue analogs**

4.1 Introduction

Breast cancer is the second leading cause of death in women, behind lung cancer, and 1-in-8 women are diagnosed with this dreadful disease (DeSantis, Ma et al. 2014). Triple negative breast cancer (TNBC) is an aggressive subtype wherein the cells do not express commonly targeted receptors for estrogen (ER), progesterone (PR), and human epidermal growth factor 2 (HER2) (Hudis and Gianni 2011). TNBC accounts for approximately 15% of all breast cancers and is very aggressive with a disproportionately higher rate of metastasis (Andre and Zielinski 2012). Additionally, patients with distant metastatic disease show a significantly shorter survival time with TNBC relative to all other breast cancer types (Kassam, Enright et al. 2009). Currently there is an unmet need for novel approaches to treating patients with metastatic TNBC and recent studies have revealed that TNBC has a higher propensity of metastasizing to the lungs (Andre and Zielinski 2012, Gerratana, Fanotto et al. 2015).

Pulmonary delivery presents a promising approach for delivering local therapy to the lungs of both primary and secondary lung cancer patients due to higher local concentrations and reduced systemic side effects (Otterson, Villalona-Calero et al. 2007, Otterson, Villalona-Calero et al. 2010). Additionally, clinical trials with stage IV lung cancer patients showed a statistically significant increase in median survival time when carboplatin was administered via combined injection and inhalation as opposed to injection only (Zarogoulidis, Eleftheriadou et al. 2012). These results suggest that

pulmonary delivery has the potential to complement traditional approaches for patients with metastatic disease in the lungs. Additionally researchers have been interested in delivering iron oxide magnetic nanoparticles to the lungs for thermal therapy applications (Stocke, Meenach et al. 2014).

Iron oxide magnetic nanoparticles (MNPs) represent a unique class of materials that have generated a considerable amount of interest for biomedical applications (Hao, Xing et al. 2010). The biocompatibility of MNPs has led to a variety of commercialized biomedical applications (Mahmoudi, Sant et al. 2011) and their ability to be actuated remotely via an alternating magnetic field (AMF) has spurred interest in their therapeutic potential (Jordan, Scholz et al. 1999, Frimpong and Hilt 2010). In the presence of an AMF, iron oxide magnetic nanoparticles generate heat through Brownian and Néel relaxation and this thermal energy can be used to actuate the onset of therapy or as a form of therapy itself (Satarkar and Hilt 2008, Satarkar and Hilt 2008, Frimpong, Dou et al. 2010, Satarkar, Meenach et al. 2011, Wydra, Kruse et al. 2013). For cancer patients, researchers have been interested in the potential advantages of thermal therapy both in isolation and in combination with anticancer agents but clinical translation of such therapies has been limited (Vertrees, Leeth et al. 2002, Babincova, Altanerova et al. 2008, Thiesen and Jordan 2008, Lubner, Brace et al. 2010, Kruse, Meenach et al. 2014).

Over the past several years, cellular spheroids have gained interest as more representative cancer models due to large discrepancies between traditional two-dimensional cell culture and physiological tumors (Bates, Edwards et al. 2000). Additionally, multicellular spheroids attempt to more accurately represent the heterogeneity present in the tumor environment by combining two or more cell types

(Kunz-Schughart, Kreutz et al. 1998). Conversely, our lab went a step further to develop tumor tissue analogs composed of tumor cells as well as normal fibroblasts and endothelial components (Upreti, Jamshidi-Parsian et al. 2011). The combination of normal and neoplastic cells allows for a more accurate recapitulation of the microtumor environment, which is often neglected with *in vitro* assays.

In this work, we developed TNBC micrometastatic tumor tissue analogs (TM analogs) to study the potential of inhalable formulations for secondary lung cancer patients with highly metastatic TNBC. The TM analogs were composed of the following three murine cell lines: 4T1 breast cancer cells (ER-, PR-, and HER2- (Kau, Nagaraja et al. 2012)), MEF fibroblast cells, and C166 endothelial cells. Iron oxide magnetic nanoparticles were previously formulated into inhalable magnetic nanocomposites (MnMs) via spray drying (Stocke, Meenach et al. 2014) and, here, were applied to the TM analogs. Remote controlled thermal therapy on TM analogs was accomplished using a custom alternating magnetic field (AMF) and the resulting tissues were analyzed both quantitatively and qualitatively.

4.2 Material and methods

4.2.1 Materials

4.2.2 Formulation of inhalable magnetic nanocomposite microparticles

The formulation and characterization of the materials used in this work were previously reported (Stocke, Meenach et al. 2014). Briefly, uncoated iron oxide magnetic nanoparticles (MNPs) were synthesized via aqueous co-precipitation of ferric and ferrous iron salts at a 2:1 ratio, respectively. The MNPs were washed with ethanol and water and

allowed to dry before incorporation into inhalable dry powder composites via spray drying with a Büchi Mini Spray Dryer B290 coupled with a B-295 Inert Loop and high-performance cyclone (all from Büchi Labortechnik, Flawil, Switzerland). D-mannitol was dissolved in methanol and iron oxide MNPs were weighed out at 20 wt% based on the combined mass of these two components, which resulted in a dilute concentration of 0.1% wt/vol in methanol. Two liters of the feed mixture were fed to the spray dryer at a pump rate of 50% (15 mL/min) through a stainless steel nozzle with a diameter of 0.7 mm. Spray drying experiments were carried out in closed mode using UHP dry nitrogen gas at a flow rate of 600 L/h, an inlet temperature of 150°C, an aspirator rate of 35 m³/h, and under sonication via water bath sonicator. Powders were collected and transferred to a glass desiccator over Drierite™ and stored in the freezer at -23°C.

4.2.3 Formation of triple negative breast cancer micrometastatic tumor tissue analogs (TM analogs)

4T1-mcherry tumor cells, C166-GFP endothelial cells and murine embryonic fibroblasts (MEF) were used to generate 3D TM analogs “hanging drops” of media (Dulbecco modified Eagle medium with 10% fetal bovine serum and antibiotic mix). Briefly, single cell suspension of 4T1-mcherry cells, C166-GFP cells and MEF cells in equal proportion (3000 cells/20µL) was dispensed on the inside of the lid of each well of a 48-well cell culture plate (Greiner Cellstar, BioExpress, Kaysville, UT). The growth of tumor tissue analogs was monitored over time until day 10 in a hanging drop of medium, following which they were subject to MNP (Magnetic nanoparticle) treatment. The 3D co-cultures/ tumor tissue analogs were subsequently transferred to optically clear Greiner

repellent plates for MNP and AMF treatment, imaging and analysis of the treatment response.

4.2.4 MNP-treatment of TM analogs

MnM powders were dispersed in media at 1.0 mg/mL and 0.1 mg/mL and these two treatment groups will be referred to as high dose (HD) and low dose (LD), respectively. The media surrounding TM analogs was carefully removed and 50 μ l of the MNP dispersions was transferred to each 96-well containing n=5 TM analogs. For control groups fresh media was added to the 96-wells. Each treatment group consisted of 4 96-wells, totaling 20 TM analogs, and these groups are summarized in Table 4.1. The TM analogs were allowed to incubate in the MNP suspensions for 24 hours at 37°C in a humidified environment supplemented with 5% CO₂. After 24 hours of MNP-exposure, the TM analogs were rinsed with media 3 times and placed on a trans-well insert in a 35 mm petri dish. 2 ml of media was added to the dish in order to insure the TM analogs had sufficient supply of nutrients during hyperthermia treatments.

4.2.5 Remotely actuated hyperthermia using a custom alternating magnetic field (AM)

For hyperthermia experiments each petri dish was placed directly above the coil of a custom Taylor Winfield[®] Alternating Magnetic Field (AMF) Source. The AMF was ran at a field strength of 55 kA/m at a frequency of 300 kHz and the AMF treatment groups were exposed to the field for 1 hour. During the experiments a custom built Styrofoam casing was used to enclose the coil and petri dish and a hot air supply was used to hold the temperature of the surroundings to approximately 37°C. A Luxtron

Optical Thermometer® was used to measure the temperature of the surroundings throughout these experiments and the hot air supply was adjusted manually in order to maintain 37°C. After AMF-exposure, each treatment group was allowed to incubate for 4 hours at 37°C in a humidified environment supplemented with 5% CO₂. TM analogs were fixed in 4% formaldehyde for 24 hours. Table 4.1 summarizes the treatment groups in this study and the corresponding naming convention used here.

Table 4.1: Summary of treatment groups for TM analogs for inhalable dry powders.

System	[MNP] (mg/mL)	MNP exposure time (hr)	AMF exposure time (hr)
Control	-	24	-
LD MNP	0.1	24	-
HD MNP	1.0	24	-
Control +AMF	-	24	1
LD +AMF	0.1	24	1
HD +AMF	1.0	24	1

4.2.6 Fluorescent imaging on TM analogs

After remotely actuated hyperthermia experiments TM analogs (n=5) were allowed to incubate for 72 hours at 37°C in a humidified environment supplemented with 5% CO₂ and imaged with a FV1000 laser scanning confocal microscope. For each TM analog, images were captured with a 453 nm laser for green fluorescent and 532 nm laser

for red fluorescent. Bright field images were captured to estimate the size of the TM analogs. Images were processed using FV10-ASW 1.7 viewer software. Images were analyzed using Olympus image analysis software and ImageJ 1.47v (National Institute of Health, Bethesda, USA) as 8-bit. These images were reported along with a composite wherein the 3 separate images were merged.

4.2.7 Quantification of cell death using Sytox

In order to quantify the amount of cell death TM analogs (n=5) were stained with Sytox Blue Dead Cell Stain. SYTOX blue stain is a high-affinity nucleic acid stain that easily penetrates cells with compromised plasma membranes. Spheroids were incubated with SYTOX blue to observe the dead cells, which were excited with argon 406 lasers.

4.2.8 Prussian blue staining for iron

The amount of iron present in TM analogs was evaluated using a Prussian Blue stain for iron content. Spheroids were harvested and processed through sucrose gradient and then snap frozen in O.C.T, Tissue-Tek, Miles USA, Inc. (Elkhart, IN). Five micrometer cryostat sections were obtained with the help of a Leica CM1950 cryotome and transferred on to Superfrost™ Plus slides (Fischer Scientific; Boston, MA) for detection of iron-oxide particles using Prussian blue staining. Sections were dipped in freshly prepared 10% aqueous solution of potassium ferrocyanide and hydrochloric acid for 20 minutes to stain iron accumulated within TM analogs. Sections were then washed three times with distilled water and counterstained with nuclear red for 5 minutes. After rinsing the slides, sections were dehydrated through grades of alcohol and then cleared with xylene and permanent slides were made after coverslipping with permount media

(Sigma). Light microscopic images were obtained at 10x and 20x magnification with the help of Olympus light microscope (Olympus America Inc., Melville, NY) for identifying the distribution of iron-oxide nanoparticles within TM analogs.

4.2.9 Transmission electron microscopy (TEM) on TM analogs

Transmission electron microscopy (TEM) was carried out on TM analogs (n=5) in order to qualitatively observe MNP uptake and cellular characteristics after AMF treatment. Immediately following 1 hour of AMF exposure the TM analogs were placed in an incubator for 4 hours at 37°C in a humidified environment supplemented with 5% CO₂. Subsequently, TM analogs were transferred to a 20 mL glass vial and washed with 0.1 M Sorenson's Phosphate Buffer (SPB) to remove media before fixing. The buffer was removed and a 3.5% glutaraldehyde solution in 0.1 M SPB was added to the vial and allowed to sit for 45 min at approximately 4°C. Subsequently, the fixate was removed and the TM analogs were washed three times for 5 minutes in 0.1 M SPB supplemented with 5% sucrose. After this, the SBS was removed and a 1% osmium tetroxide solution in 0.1 M SPB was added to the vial containing the TM analogs and allowed to sit for 45 mins at 4°C. The osmium tetroxide solution was removed and TM analogs were washed with 0.1 M SPB and dehydrated by subsequent ethanol washes at 50-, 70-, 80-, 90-, and 100% (twice) for 10 mins each. After the second wash with 100% ethanol the TM analogs were washed with propylene oxide twice for 20 mins each. The propylene oxide was then removed and the TM analogs were allowed to sit overnight under a mild heating lamp in a 1:1 mixture of propylene oxide and an epoxy resin. The next day, the propylene oxide and epoxy resin mixture was removed and the cells were washed with

just the epoxy resin twice for an hour each time. After the second wash was removed the TM analogs were transferred to a centrifuge tube for sectioning, epoxy resin was added and the samples were allowed to polymerize for 48 hours at 60°C. After polymerization, the pellets were sliced into 70-90 µm sections with a Reichert-Jung Ultracut E microtome and stained with a combination of uranyl acetate, (saturated solution in 70% ethanol) for 5 minutes, and lead citrate, (see attached recipe), for 2 minutes. The specimens were observed using a Philips Tecnai Biotwin 12, manufactured by FEI.

4.3 Results and Discussion

The effect of MNPs, released from the inhalable dry composites, on the TM analogs (n=5) was examined 5 days post MNP-exposure with fluorescent and brightfield imaging (Figure 4.1) for three different MNP doses (control, LD, and HD). In addition to illustrating the reproducibility of these spheroids, these data show no apparent adverse effect on the mechanical stability of the TM analogs. Additionally, these data confirm the presence of all three cell types wherein each panel shows evidence of the MEF (green), 4T1 (red) and C166 (colorless) cells confirming their multicellular composition.

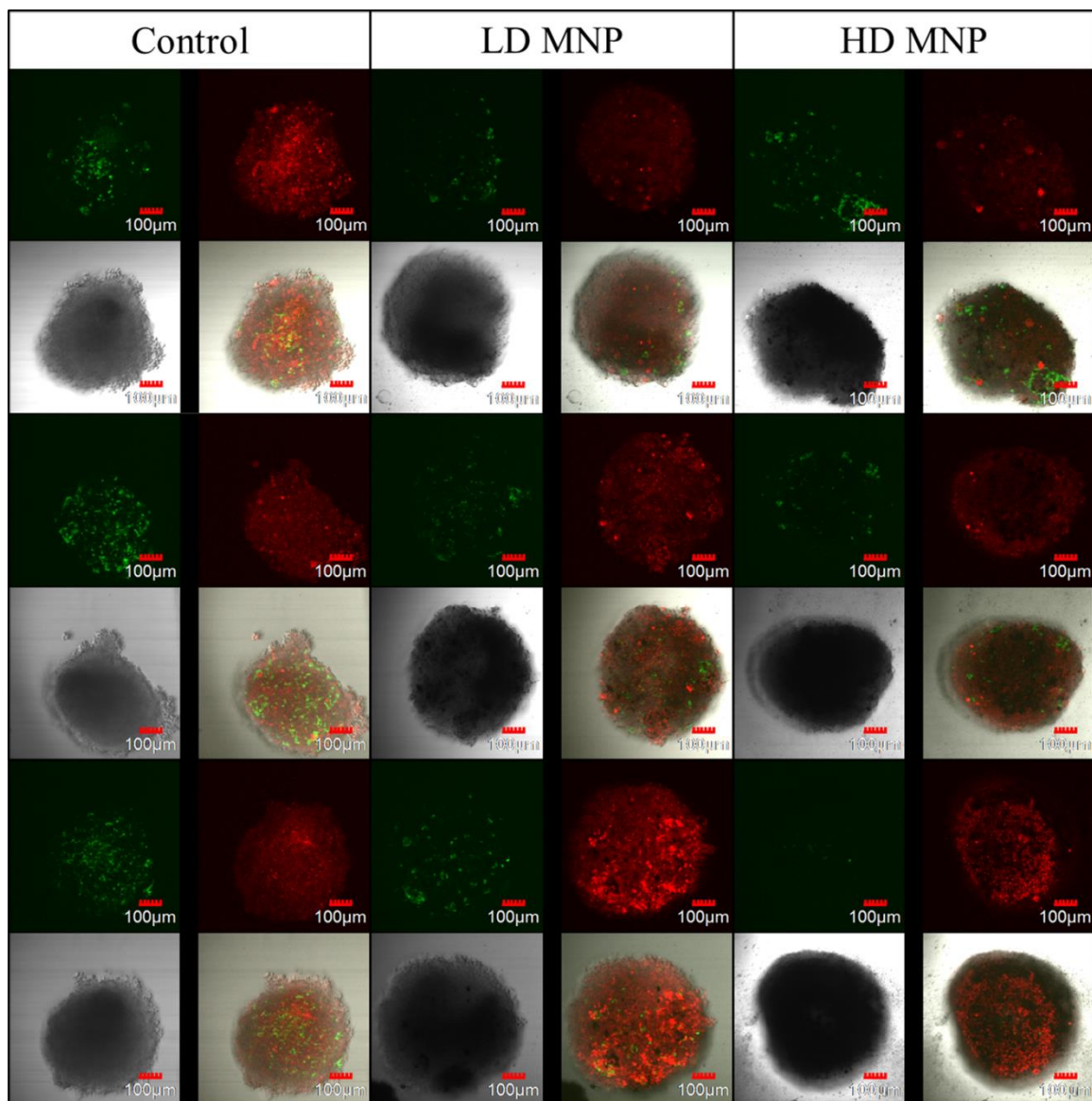


Figure 4.1: Microscopy images (n=3) of TM analogs after MNP-exposure (-AMF). The treatment groups are arranged in columns with increasing MNP dose from left to right. Left column is control group (n=3); middle column is LD MNPs; right column is HD MNPs. Each panel consists of the following 4 images: green fluorescent (MEF cells, top left), red fluorescent (4T1, top right), bright-field (bottom left), and overlay (bottom right). Images were captured t=5 days post MNP exposure.

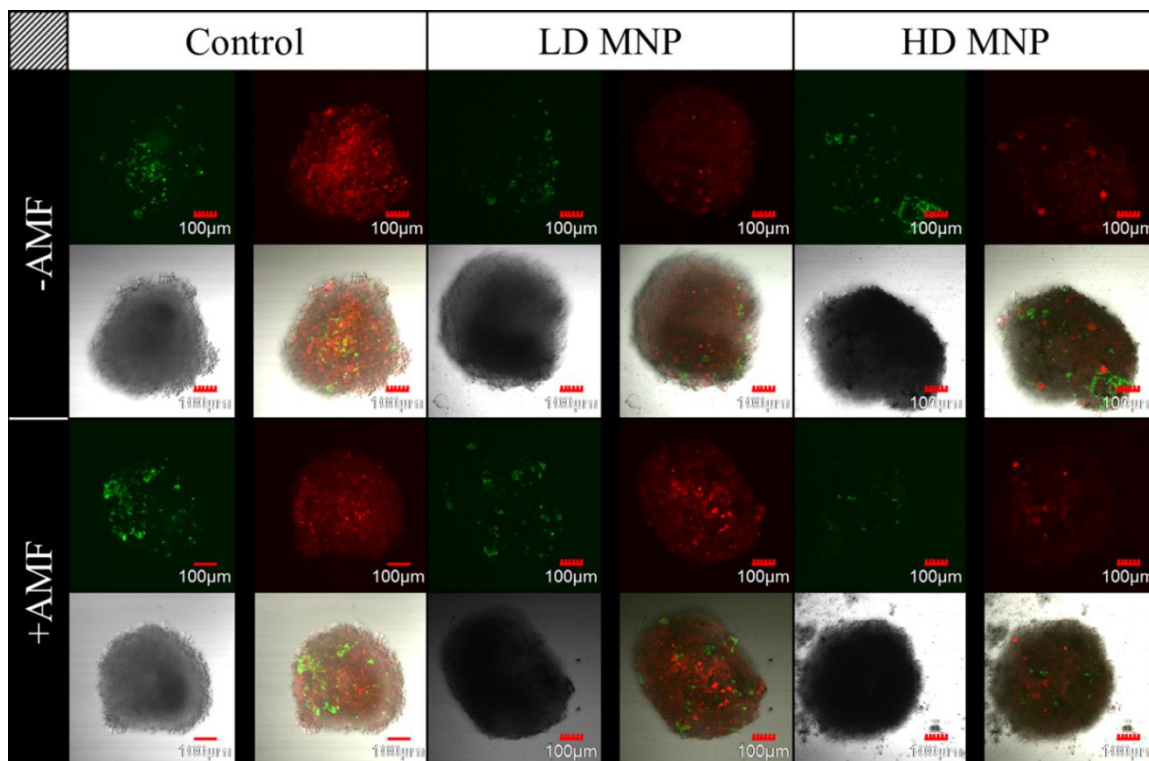


Figure 4.2: Comparison of TM analogs with- (+AMF; bottom row) and without (-AMF; top row) application of AMF for 1-hour. The treatment groups are arranged in columns with increasing MNP dose from left to right. Left column is control group (n=3); middle column is LD MNPs; right column is HD MNPs. Each panel consists of the following 4 images: green fluorescent (MEF cells, top left), red fluorescent (4T1, top right), bright-field (bottom left), and overlay (bottom right). Images were captured t=5 days after AMF exposure.

The effect of AMF-exposure on TM analogs was also examined through fluorescent and brightfield microscopy. TM analogs from each treatment group (n=5) were placed in an AMF for 1 hour (designated +AMF) and Figure 4.2 compares these spheroids with their corresponding TM analogs containing the same MNP dose yet not placed in AMF

(designated -AMF). As expected, no difference was observed in the +AMF and -AMF control groups (without MNPs) suggesting the experimental conditions had no effect on the tissues. Interestingly, as the MNP dose increased, we saw signs of mechanical deterioration occurring in the TM analogs as evident by cellular debris surrounding the spheroids. This was increasingly pronounced in the HD +AMF treatment group wherein large amounts of cellular debris were observed (Figure 4.2f).

Subsequently, cellular death from MNP and AMF exposure was quantified in these advanced *in vitro* models to examine the potential of the inhalable composites for treating secondary lung malignancies. Cellular death was quantified by staining TM analogs from each treatment group (n=5) with SYTOX[®] Blue (dead stain) 5 days post AMF experiments. Fluorescent images were captured (Figure 4.3) and the normalized mean integrated fluorescence intensity of the SYTOX[®] Blue was calculated as an indicator of cell death. Figure 4.4 reports the quantitative data and shows similar levels of cell death in all -AMF treatments (top row). Additionally, an increase in cellular death was measured in both the LD MNP +AMF and HD MNP +AMF treatment groups (Figure 4.3 e & f) but this increase was only statistically significant ($p < 0.05$) for the latter.

It should be noted that increasing concentrations of MNPs result in higher levels of MNPs deposited to the TM analogs and results in dark areas where the nanoparticles diffract light (see darkening in Figure 4.1 from left to right). This is a common issue with *in vitro* fluorescent assays using MNPs and must be taken in consideration when analyzing the data. Nonetheless, we saw a statistical increase in the amount of cell death in the +AMF treatment despite the potential reduction in fluorescent intensity from HD

MNPs. Conversely, non-specific toxic effects of MNPs could potentially be masked by reducing the dead signal through diffraction.

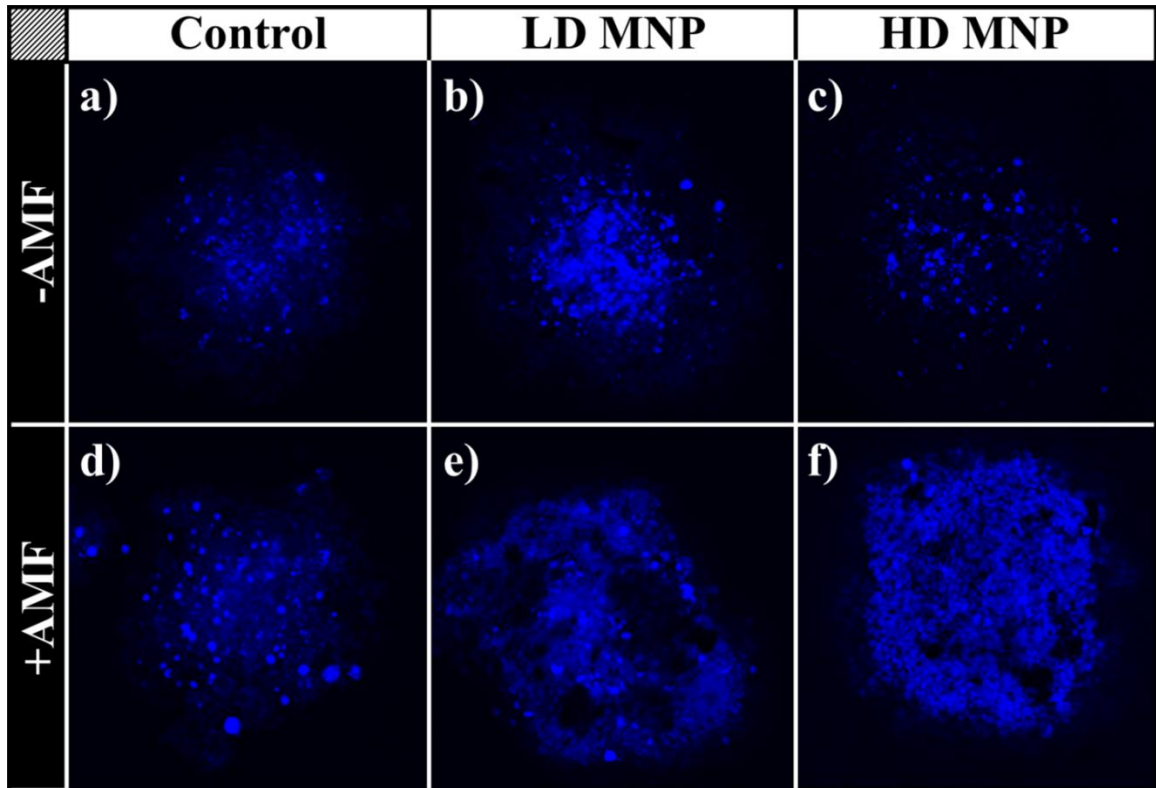


Figure 4.3: Representative fluorescent images of (top row; a-c) and bright-field (bottom row; d-f) images of spheroids stained with SYTOX® Blue dead cell stain and not exposed to AMF. From left to right the columns represent treatments of control (a,d) MNPs at 0.1 mg/mL (b,e) and MNPs at 1 mg/mL (c,f)

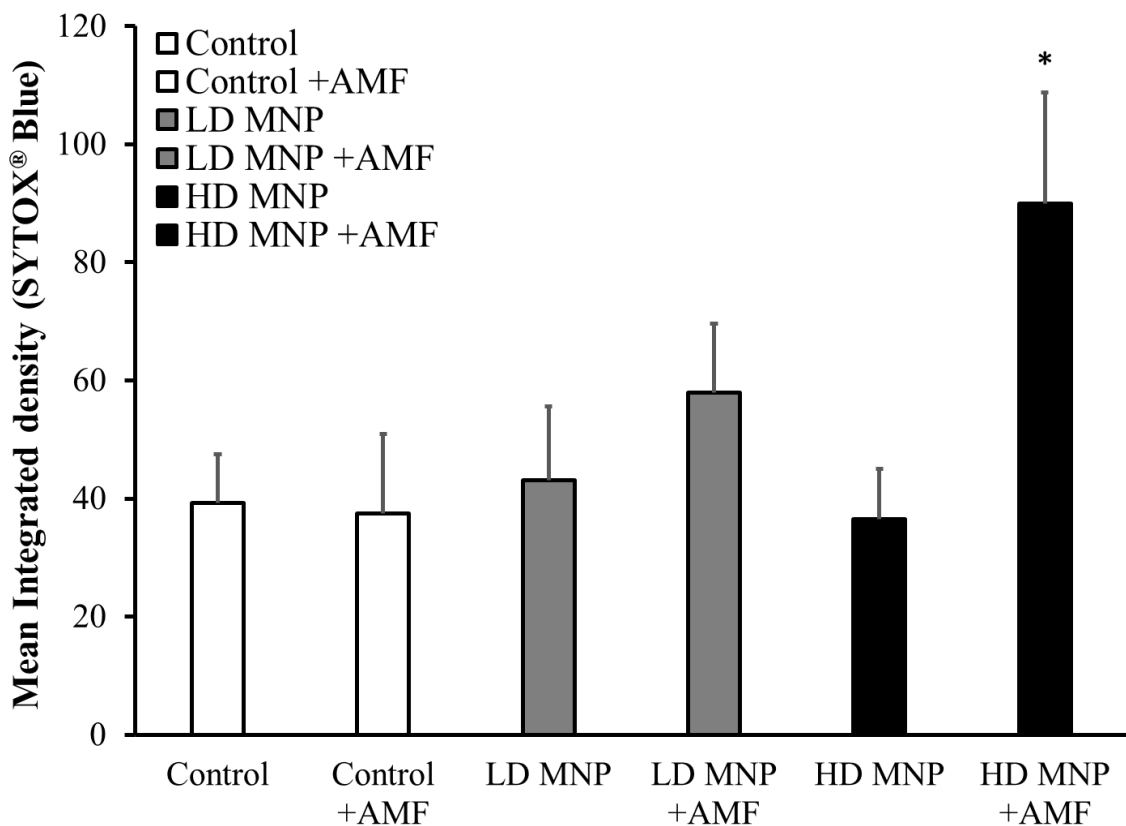


Figure 4.4: Quantification of dead cell count measured as the mean integrated density of blue signal from fluorescent images.

To investigate the accumulation and agglomeration of the MNPs in the TM analogs, histological sections were cut and stained with Prussian blue for iron content. As expected, the amount of iron in the TM analogs increased with increasing MNP dose (Figure 4.5). Additionally, to further explore this matter, TM analogs were cast in resin, sectioned, and stained for TEM imaging in order to gain a better understanding of the MNP-localization as well as cellular response. Electron micrographs were acquired for the following three treatment groups: 1) control -AMF, 2) HD MNP -AMF, and 3) HD MNP +AMF.

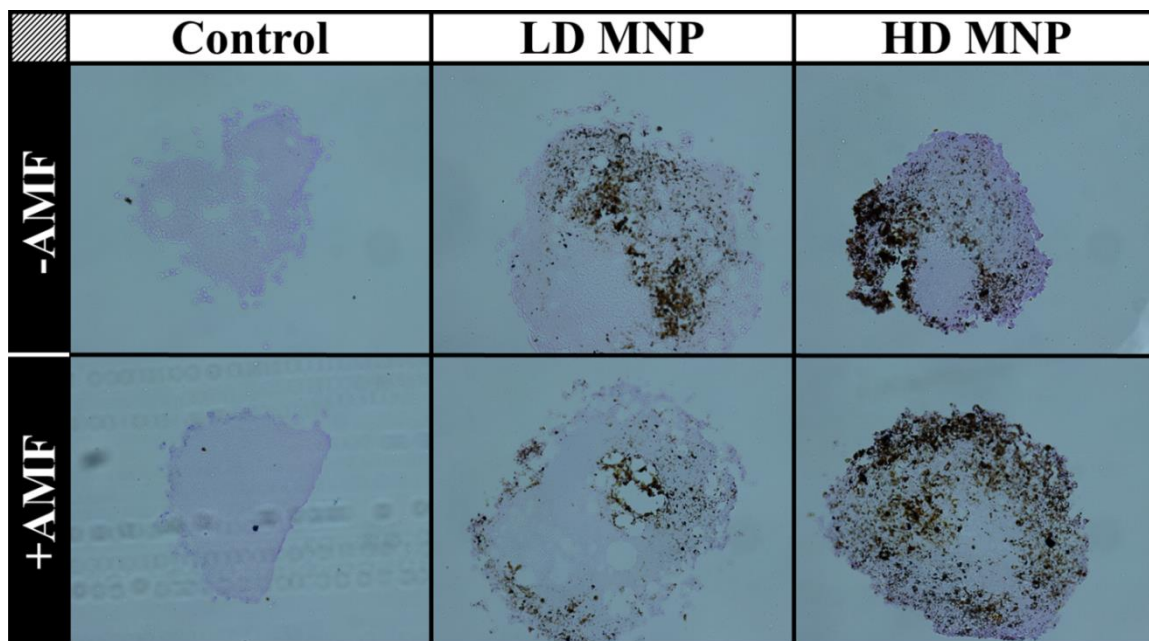


Figure 4.5: Prussian blue staining of multicellular breast cancer micrometastatic spheroids. From left to right the columns represent treatments of control (a,d) MNPs at 0.1 mg/mL (b,e) and MNPs at 1 mg/mL (c,f) with the top row (a-c) being treatments without AMF exposure and the bottom row (d-f) exposed to AMF.

TEM images taken at the center of the TM analogs (Figure 4.6) showed no penetration of MNPs to this region of the tissue. However, TM analogs exposed to MNPs displayed an extracellular component that was not seen in the control group. This extracellular material was much more prevalent in the HD MNP +AMF (see supplemental figures) treatment group and could be cellular debris as a result of autophagy (Galluzzi, Maiuri et al. 2007). A specific example of this observation is reported in Figure 4.7 wherein this extracellular debris is surrounding cells displaying massive vacuolization of the cytoplasm, which is an indicator of autophagy (Galluzzi, Maiuri et al. 2007).

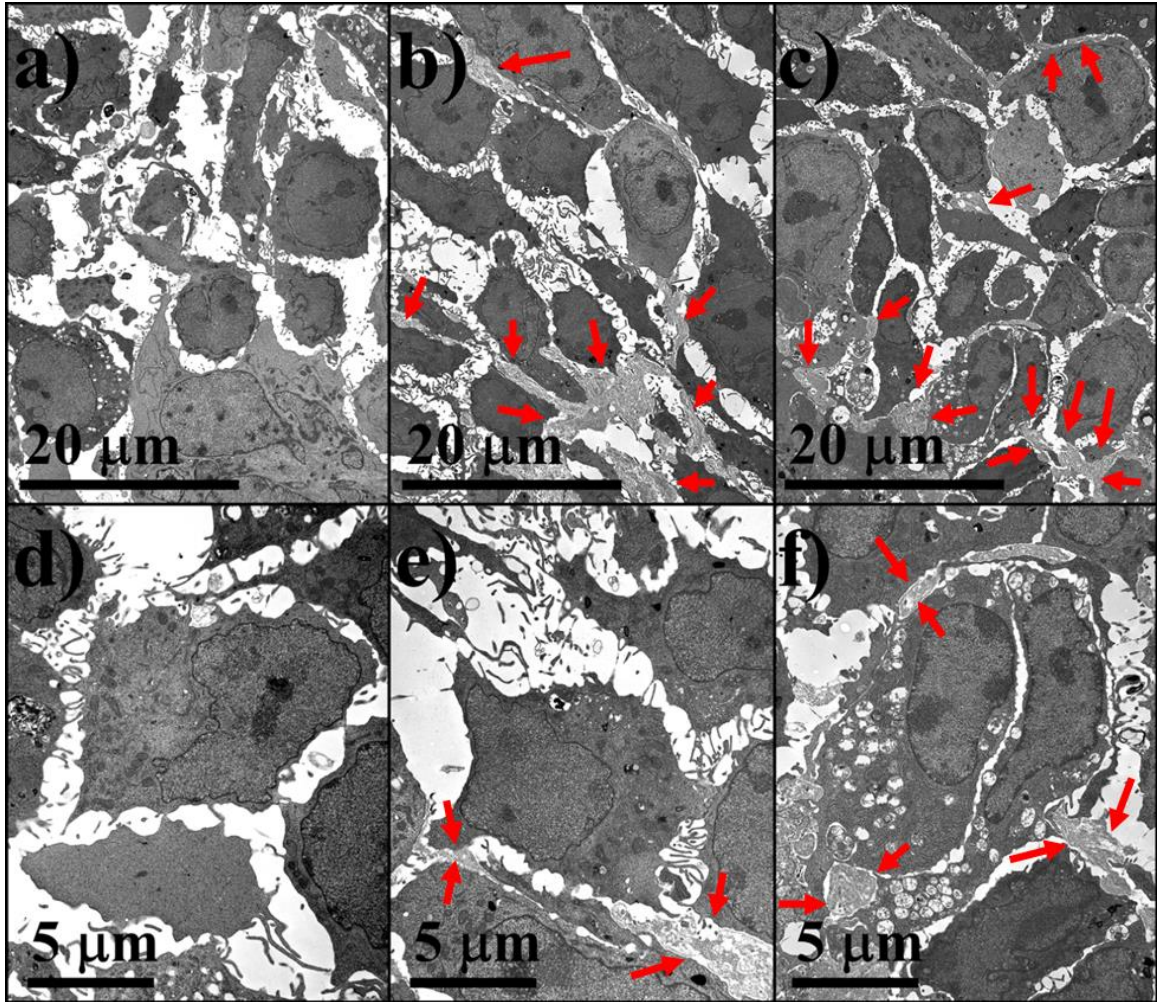


Figure 4.6: TEM images of the center of TM analogs. Control -AMF (left column; a, d), LD -AMF (middle column; b, e), and HD +AMF (right column; c, f) at magnifications of x2900 (top row; a-c) and x6800 (bottom row; d-f). Red arrows point at extracellular material in MNP treatments.

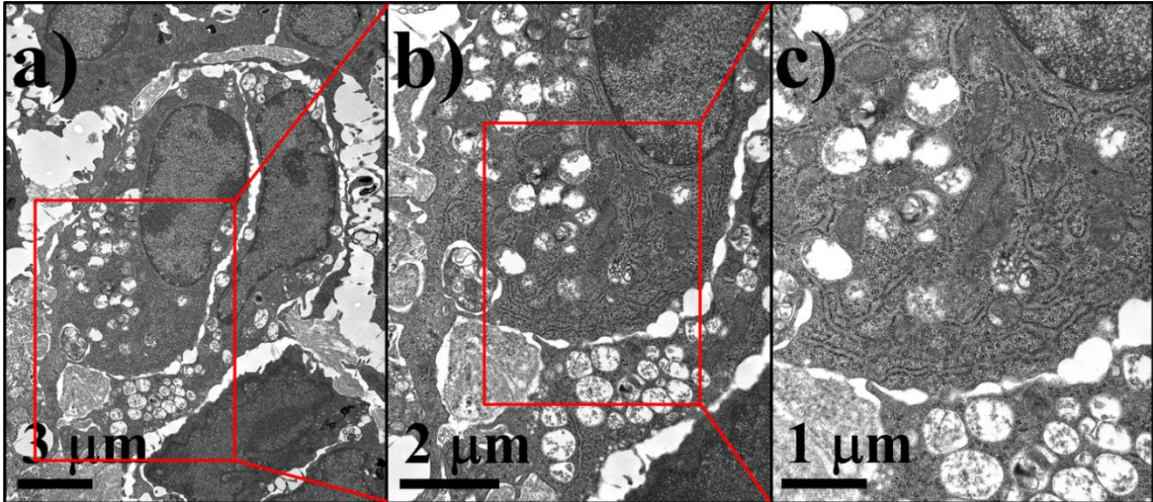


Figure 4.7: TEM images of cells displaying massive vacuolization of the cytoplasm at magnifications of a) x6800, b) 11,000, and c) 23,000. Red box shows where adjacent image is located in lower mag image.

Additionally, TEM images taken at the periphery of the TM analogs (Figure 4.8) clearly show the presence of MNPs in the HD -AMF and HD +AMF treatment groups. The MNPs that are released from the composites powders during exposure to TM analogs have a core diameter of approximately 10 nm and a hydrodynamic diameter of approximately 150 nm (Stocke, Meenach et al. 2015); however, a large portion of the MNPs that accumulate in TM analogs appear as very large agglomerates which could be occur as a result of MNPs settling on the surface of the spheroids during exposure. An example of an internalized MNP is given in Figure 4.8.

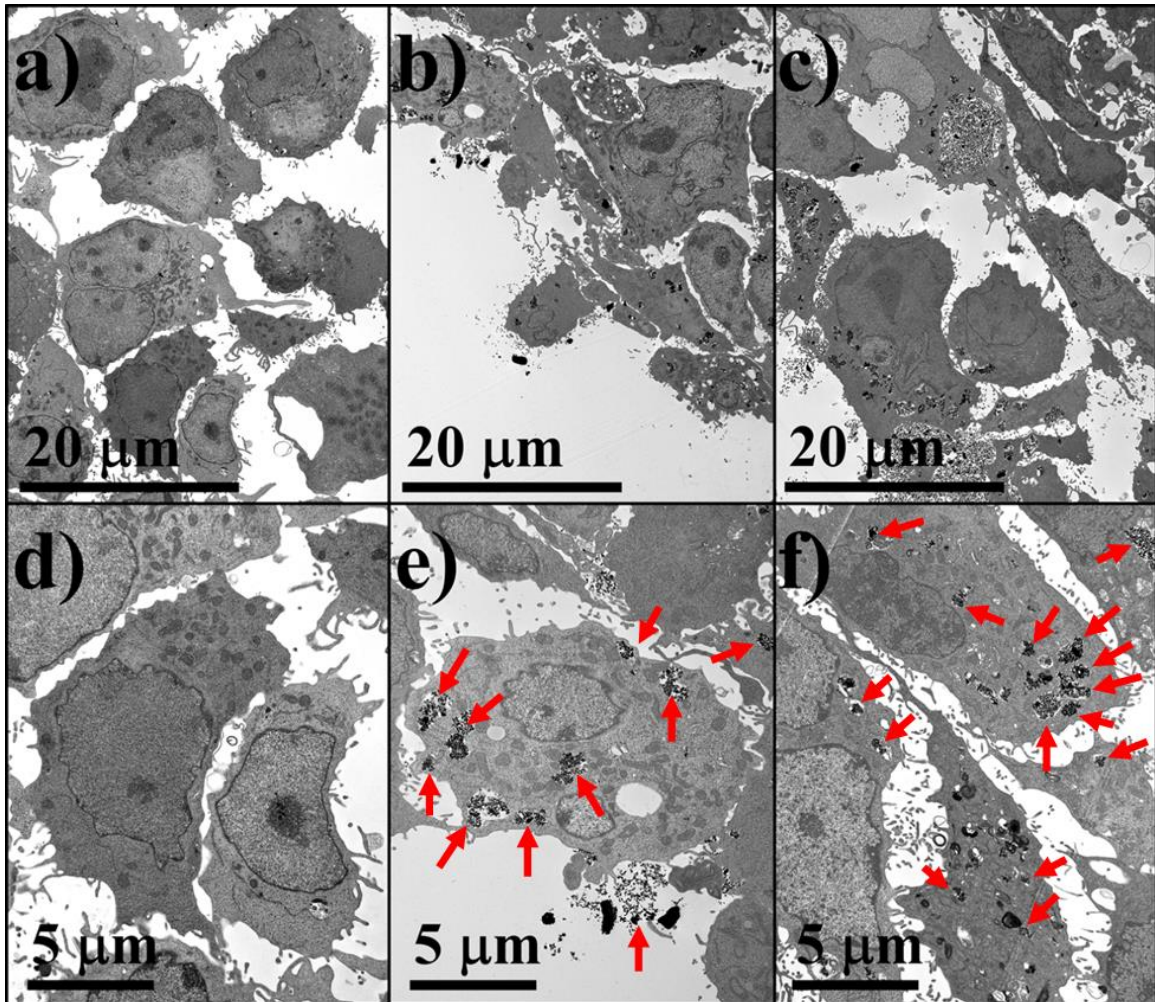


Figure 4.8: TEM images of the edge of TM analogs. Control -AMF (left column; a, d), LD -AMF (middle column; b, e), and HD +AMF (right column; c, f) at magnifications of x2900 (top row; a-c) and x6800 (bottom row; d-f). Red arrows point at large MNP agglomerates.

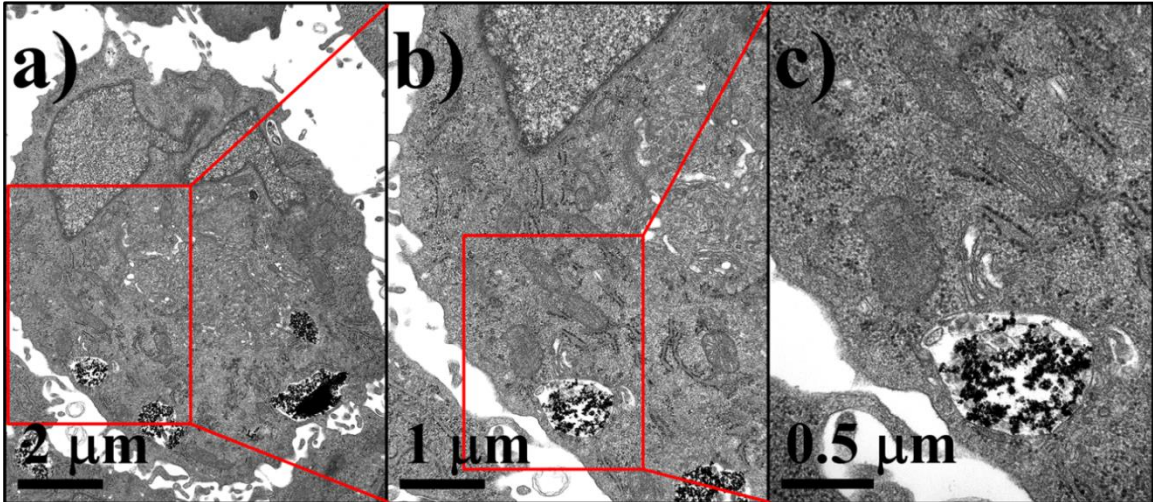


Figure 4.9: TEM images of HD MNP -AMF TM analogs at x2900 (a, d), x4800 (b, e) and x6800 (c, f). Top row (a-c) are images from center of TM analog and bottom row (d-f) are images from edge.

In vivo studies involving aerosols containing MNPs have previously been reported for hyperthermia applications, but these studies aerosolized a liquid suspension of EGFR-targeted MNPs (Sadhukha, Wiedmann et al. 2013). These studies utilized an orthotopic lung cancer mouse model and saw a reduction in tumor bioluminescence when an AMF was applied. Others have reported the ability to target liquid aerosols containing MNPs to specific regions within the lungs of mice by applying a stationary magnetic field (Dames, Gleich et al. 2007, Hasenpusch, Geiger et al. 2012). Such findings illustrate the potential of these MNP-containing inhalable aerosols for metastatic patients in which surgery is not generally recommended (Zarogoulidis, Zarogoulidis et al. 2013).

4.4 Conclusions

Triple negative breast cancer micrometastatic tumor tissue analogs (TM analogs) were successfully formed and showed relatively consistent size and spherical morphology, thereby highlighting their potential as advanced *in vitro* models of secondary lung malignancies. Previously reported inhalable MnMs were applied to these advanced models and showed no measureable adverse effects in the absence of AMF-exposure. Conversely, remote controlled thermal therapy on was accomplished by placing the TM analogs in an alternating magnetic field (AMF). TM analogs subjected to a high enough concentration of MNPs showed a statistically significant increase in cellular death after AMF-exposure and indicated the potential of these inhalable composites for future development. These TM analogs provide an approved physiologically relevant *in vitro* model of secondary lung malignancies from metastatic TNBC and our findings suggest the potential of inhalable composites containing MNPs.

Chapter 5 Formulation and Characterization of Inhalable Anticancer Agents for Targeted Pulmonary Delivery via Spray Drying

The ability to deliver two common anticancer agents was examined by spray drying these drugs into inhalable composites. The aerodynamic performance of these composites was examined and cell culture studies with two human lung cancer cell lines were carried out to insure the drugs retained their activity. The goal was to formulate inhalable powders containing ACAs with adequate aerodynamic performance and to be able to release active ACAs. The chapter is taken directly or adapted from work that was recently submitted to Pharmaceutical Research. Used with permission from Nathanael A Stocke, Marjorie L. Guy, Shuo Tang, Heidi M. Mansour, Susanne M. Arnold, Heidi M. Mansour, and J. Zach Hilt.

5.0 Abstract

Non-small cell lung cancer (NSCLC) is the leading cause of cancer mortality worldwide. Patients diagnosed with this devastating disease have low survival rates and high incidence of recurrence, thus highlighting the need for more effective lung cancer treatment modalities. Pulmonary delivery provides a platform for noninvasive delivery of novel materials to the lungs and has the potential for delivering equivalent local anticancer agent (ACA) concentrations while reducing systemic side effects. Here, we formulated inhalable powders consisting of the two FDA-approved ACAs cisplatin and erlotinib (active drug in the non-inhalation drug product, Tarceva[®]) and characterized their physicochemical properties with a variety of techniques. Cascade impactor studies

were used to evaluate the aerodynamic performance of these powders and *in vitro* cell studies determined the activity of the ACAs released from the powders in two human lung cancer cell lines. Inhalable ACAs were examined with scanning electron microscopy and showed spherical particle morphology and relatively uniform size distribution yet unique surface characteristics (typo-suggest correcting and clarifying) based on particle composition. The inhalable ACAs showed good aerodynamic performance with MMAD values ranging from 3.0-5.6 μm and all powders displaying fine particle fractions >25% even in the absence of a carrier such as lactose. Finally, *in vitro* cell culture studies revealed that cisplatin and erlotinib incorporated into inhalable powders retained their activity upon release into media and confirmed the potential of these systems for future development.

5.1 Introduction

Non-small cell lung cancer (NSCLC) accounts for 85% of all lung cancers and is the leading cause of cancer mortality worldwide (Mellas, Elmesbahi et al. 2010, Bonomi, Pilotto et al. 2011, Tucker, Laguna et al. 2012). While, surgical resection cures the majority of early stage NSCLC, most patients are diagnosed with inoperable, incurable stage III and IV lung cancer (Fathi and Brahmer 2008, Mazzone and Mekhail 2012, Tucker, Laguna et al. 2012). Additionally, over 40% of NSCLC patients develop recurrences even after surgery, and this contributes to 5- and 10-year mortality rates of less than 15 and 7% respectfully (Crino, Weder et al. 2010, Bonomi, Pilotto et al. 2011, Tucker, Laguna et al. 2012). Hence, there is a critical need for more effective lung

cancer treatment modalities consisting of noninvasive and nontoxic alternatives built around novel materials with great therapeutic potential.

Chemotherapy, the mainstay of treatment in metastatic disease, causes significant toxicity and this has driven researchers to develop targeted drug delivery systems. Cisplatin is the most common anticancer agent (ACA) and was first examined for anticancer activity in 1968 after showing inhibition of cell proliferation in bacteria cultures (Rosenberg 1985). Since its approval for medical use in 1978 by the United States Food and Drug Administration (FDA), cisplatin has been used in the treatment of a variety of cancers such as ovarian, testicular, and bladder as well as head and neck cancer (Babincova, Altanerova et al. 2008). While cisplatin is a highly toxic and nonspecific ACA, more recent efforts to personalize cancer treatment have led to the development of drugs targeted to patients with specific genetic alterations.

Erlotinib (Tarceva®) is a small molecule tyrosine kinase inhibitor (TKI), and was approved for the treatment of NSCLC patients after showing a survival benefit for patients with tumor associated epidermal growth factor receptor (EGFR) mutations (Eberhard, Johnson et al. 2005). These findings have paved the way for a large increase in efforts toward genetically personalized cancer treatment and represent an exciting field of cancer-related drug delivery research.

In general, alternative drug delivery platforms focus on improving the safety and/or efficacy of an active pharmaceutical ingredient. For chemotherapy, high toxicities associated with systemic delivery of ACAs as well as low concentrations within tumors advocate the exploration of alternative delivery options. Localizing the concentration of

ACAs to the lungs and lowering their corresponding systemic delivery could increase the efficacy of for appropriate lung tumors.

Pulmonary delivery provides a platform for noninvasive delivery of novel materials to the lungs and has the potential for delivering equivalent local ACA concentrations while reducing systemic side effects. This administration route is well established for treating other pulmonary diseases such as asthma (Hasenpusch, Geiger et al. 2012) and displays characteristics that are promising for its translation into a novel lung cancer treatment strategy (Hasenpusch, Geiger et al. 2012). A clinical study evaluating the effectiveness of inhaled carboplatin (nebulized liquid solution) revealed a significant increase in survival for stage IV NSCLC patients who received a combination of intravenous and pulmonary drug administration as opposed to IV or pulmonary only. This suggests that even advanced-stage NSCLC patients could potentially benefit from a portion of their chemotherapy being delivered via inhalation. Hence, it is possible that targeted pulmonary delivery could present a more effective or complimentary treatment modality for certain NSCLC patients.

Inhalable therapies, traditionally, consist of liquid droplets or solid particles with a mass median aerosol diameter (MMAD) of $<5 \mu\text{m}$ in order to be respirable (Hickey, Mansour et al. 2007, Xu, Mansour et al. 2010). Common inhalable therapies include nebulizers, metered dose inhalers, and dry powder inhalers (DPIs). Dry powder inhalation systems are preferable to traditional metered dose inhalers and nebulizers because of superior stability and ease of use for associated devices (El-Gendy and Berkland 2009). Conversely, spray drying provides the ability to reproducibly formulate dry powders consisting of microparticles that are suitable for pulmonary delivery and

offers the ability to control certain physiochemical properties of these particles by adjusting process parameters (Vanbever, Mintzes et al. 1999, Mobus, Siepmann et al. 2012, Odziomek, Sosnowski et al. 2012, Shen, Chen et al. 2012). Additionally, spray-drying allows for easy production of powders composed of multiple chemical species by simply dispersing them in the feed solvent and therefore provides a platform for formulating inhalable composites.

Here, we have formulated and characterized inhalable powders consisting of two approved ACAs for lung cancer treatment cisplatin and erlotinib. The physicochemical properties of these powders were examined by a variety of techniques and the ACA loadings were determined. The aerodynamic performance of these powders was determined with the Next Generation Impactor®. *In vitro* cell studies were used to compare the inhalable powders to their respective free form of each drug in two human lung cancer cell lines in order to evaluate the activity of the ACAs released from the powders upon dissolution.

5.2 Materials and Methods

5.2.1 Materials

Cis-diamineplatinum(II) dichloride (cisplatin) was purchased from Sigma-Aldrich (St Louis MO) and erlotinib hydrochloride salt was purchased from LC Laboratories (Woburn, MA). Chloroform, anhydrous methanol, and high performance liquid chromatography-grade methanol were purchased from Fisher Scientific (Pittsburgh, PA). Ultrahigh-purity nitrogen gas was from Scott-Gross (Lexington, KY). Human alveolar adenocarcinoma A549 cells and Human bronchioalveolar carcinoma H358 cells were

purchased from ATTC (Manassas, VA). Dulbecco's modified eagle's medium (DMEM), penicillin-streptomycin (PSTREP), Gibco® fetal bovine serum, and calcein AM were purchased from Life Technologies (Grand Island, NY). ULTRAgrade™ Solution Platinum Standards for ICP were purchased from Ultra Scientific (New Kingstown, RI).

5.2.2 Inhalable ACA systems

Four different powders were produced by spray drying with a Buchi mini spray dryer and these powders were designated MC0, ME0, MC10, and ME10. Due to the insolubility of cisplatin in alcohol the powder named MC10 was spray dried with water as the solvent and the mixture fed to the spray dryer was, by weight, 50% D-mannitol, 40% sodium chloride and 10% cisplatin in order to match the clinically administered formulation of cisplatin (1984). The MC0 and ME0 powders were composed of D-mannitol only and were spray dried with water and methanol as their solvent, respectively. For ME10, methanol was used as the spray drying solvent and the concentration of erlotinib, by weight, was 10% with the remaining solute being made up of D-mannitol. Table 5.1 summarizes the inhalable ACA systems formulated.

Table 5.1: Summary of experimental conditions for inhalable dry powders.

System	Drug Loading (wt%)	Inlet T (°C)	Outlet T (°C)	Solvent
MC0	0%	150	70	Water
ME0	0%	150	70	Methanol
MC10	10%	150	67	Water
ME10	10%	150	58	Methanol

5.2.3 Spray Drying

A Büchi Mini Spray Dryer B290 coupled with a B-295 Inert Loop and high-performance cyclone (all from Büchi Labortechnik, Flawil, Switzerland) was used to formulate inhalable ACAs using parameters previously optimized by our lab (Li and Mansour 2011, Stocke, Meenach et al. 2014). Spray drying experiments were ran in closed mode using UHP dry nitrogen gas at a flow rate of 600 L/h, an inlet temperature of 150°C, and an aspirator rate of 35 m³/h. Once the inlet temperature of 150°C was reached, pure solvent (water or methanol) was fed to the spray dryer until the outlet temperature stabilized and this temperature was recorded (Table 5.1). All experiments were carried out with a dilute solute concentration of 0.1% wt/vol. Four liters of the feed mixture were fed to the spray dryer through a stainless steel nozzle with a diameter of 0.7 mm. Experiments with methanol as the solvent were ran with the B-295 Inert Loop (Büchi Labortechnik, Flawil, Switzerland) and a pump rate of 50% (15 mL/min); those carried out with water as the spray-drying solvent utiliaed a B-296 Dehumidifier (Büchi

Labortechnik, Flawil, Switzerland) and were fed at a pump rate of 20% (5 mL/min). Powders were collected and transferred to a glass desiccator over Drierite™ and stored in the freezer at -23°C.

5.2.4 Scanning Electron Microscopy (SEM) on Inhalable Powders

A Hitachi S4300 Scanning Electron Microscope (Tokyo, Japan) was used to capture images of inhalable ACA powders in order to observe the particle size, surface roughness, shape and morphology. Double-sided adhesive carbon tabs were adhered to aluminum studs (Ted Pella, Redding, CA) and blotted on weigh paper containing a small amount of powder. These samples were coated with a thin film of a gold/palladium alloy using an Emscope SC400 sputter coating system at 20 mA for 4 minutes under argon gas. For all electron microscopy experiments at least 3 independent samples were examined and multiple images were examined for each sample.

5.2.5 Determination of ACA loading in spray dried composites

UV/vis spectrometry was used to determine the loading of erlotinib in the ME10 powders. Erlotinib standards were read by the spectrometer at erlotinib's absorption max (λ_{max}) of 346 nm to a standard curve. Subsequently, ME10 solutions at known concentration were placed in the spectrometer and the absorbance was read at 346 nm in order to calculate erlotinib loading. Additionally, a small amount (<20 mg) of erlotinib was spray dried without mannitol and read on the spectrometer to assure no changes in spectral properties. Samples containing equivalent amounts of D-mannitol were used in order to normalize findings.

Inductively coupled plasma optical emission spectroscopy was used to quantify cisplatin loading in the MC10 powders by measuring platinum levels in prepared samples and comparing them with standard curves. A Varian Vista Pro ICP-OES was used with argon gas for plasma generation at 1.2kW and 15L/min flow, and sample introduction at 0.9L/min nebulizer flow, 10 second replicate read time across 3 replicates, and 15 rpm pump rate. A 1ppm yttrium solution from CPI International was used to adjust for any physical interferences. ULTRAGrade™ Solution Platinum Standards were purchased from Ultra Scientific (New Kingstown, RI) at 1000 mg/L and used for calibration curves. A second standard stock was used as a laboratory control sample (LCS) at two different concentrations and the wavelength showing the best agreement between the LCS samples and their corresponding standard concentrations was selected for analysis. Prepared solutions of MC10 at known concentrations were diluted into the range of the standard curve. The resulting platinum concentrations were used to calculate cisplatin loading. Additionally, solutions of cisplatin were injected to confirm the validity of the concentration calculations.

5.2.6 Differential scanning calorimetry (DSC)

DSC was carried out in order to determine the thermal phase transitions of the dry powders. An Auto Q20 Differential Scanning Calorimeter equipped with an RSC-90 refrigerated cooling system (TA Instruments-Waters LLC, New Castle, DE) and Tzero™ technology was used for measurements. Approximately 2 mg of sample was weighed into a Tzero™ alodined aluminum pan that was hermetically sealed and then placed into the furnace along with an empty alodined aluminum hermetically sealed reference pan.

The temperature was initialized at 0°C and subsequently raised to 250°C at a rate of 5.00°C /min.

5.2.7 X-ray powder diffraction (XRPD)

The long range order of the inhalable ACA powders was examined with XRPD. Powders were analyzed by a D8 Discover X-ray diffractometer (Bruker, Billerica, MD) with Cu K α radiation (40 kV, 40 mA, 0.15418 nm) in order to examine their crystallinity. Scans were obtained from 5 to 60° 2 θ with step size of 0.02 and scan rate of 1 °/min.

5.2.8 Particle size analysis

ImageJ® (NIH, Bethesda, MD) was used to analyze SEM images and digitally determine the mean size and standard deviation of the geometric diameter of the inhalable ACA powders. Representative SEM images at a magnification of 5000x were analyzed by measuring the diameter of at least 100 particles per image with the ImageJ software.

5.2.9 In vitro aerosol dispersion performance with the Next Generation Impactor™ (NGITM)

The M170 Next Generation Impactor™ (MSP Corporation Shoreview, MN) was used for cascade impaction experiments in accordance with United States Pharmacopeia (USP) Chapter <601> specifications on aerosols (2006) as previously reported (Meenach, Vogt et al. 2013, Wu, Zhang et al. 2013, Stocke, Meenach et al. 2014). The NGI was equipped with a stainless steel induction port (USP throat adaptor) attachment and

specialized stainless steel NGI™ gravimetric insert cups (NGI Model 170, MSP Corporation, Shoreview, Minnesota). Type A/E glass fiber filters with diameter 55mm (Pall Corporation, NY) were placed on each stage of the impactor and weighed before and after the experiment to determine the particle mass deposited. Approximately 10 mg of powder was loaded into each clear hydroxypropyl methylcellulose, size-3 capsule (Quali-V®) (QUALICAPS, Spain) and these capsules were placed into a HandiHaler® DPI™ device (Boehringer Ingelheim Pharmaceuticals, Inc. Ridgefield, CT) attached to a customized rubber mouth piece connected to the NGI™. Three capsules were loaded and released for each sample and experiments were performed in triplicate. The total dose for each sample was approximately 30 mg. A Copley HCP5 vacuum pump (Copley Scientific, United Kingdom) and a Copley TPK 2000 critical flow controller (Copley Scientific, United Kingdom) were used to produce a flow rate (Q) of 60 L/min in order to model the flow rate in a healthy adult lung. This flow rate was adjusted before each experiment using a Copley DFM 2000 flow meter (Copley Scientific, United Kingdom).

For Q=60 L/min, the aerodynamic cutoff diameters (D_{a50}) for each stage of the impactor were given from the manufacturer as: stage 1 (8.06 μm); stage 2 (4.46 μm); stage 3 (2.82 μm); stage 4 (1.66 μm); stage 5 (0.94 μm); stage 6 (0.55 μm); and stage 7 (0.34 μm). The emitted dose (ED), respirable fraction (RF), and fine particle fraction (FPF) were calculated as follows:

$$ED \% = \frac{\text{Initial mass in capsules} - \text{Final mass in capsules}}{\text{Initial mass in capsules}} \times 100\% \quad (\text{Equation 5.1})$$

$$RF \% = \frac{\text{Mass of particles on stages 2-7}}{\text{Total particle mass on all stages}} \times 100\% \quad (\text{Equation 5.2})$$

$$FPF \% = \frac{\text{Mass of particles on stages 2-7}}{\text{Initial mass in capsules}} \times 100\% \quad (\text{Equation 5.3})$$

The mass median aerodynamic diameter (MMAD) and geometric standard deviation (GSD) for the particles were determined using a Mathematica® program written by Dr. Warren Finlay (Finlay 2008).

5.2.10 Cytotoxicity tests

Cells were cultured in 75 cm² flasks in DMEM containing 10% FBS, 5% PSTREP, and 1% Fungizone at 37°C in a humidified incubator with 5% CO₂. For viability studies, cells were seeded into 96-well plates at 10,000 cells/cm², placed in an incubator at 37°C and allowed to attach overnight. Cells were dosed cisplatin or erlotinib in raw form for 24 hours. Studies with MC10 and ME10 were carried out at equivalent cisplatin and erlotinib concentrations, respectively, as calculated from drug loading results. After exposure cells were allowed to grow in fresh media for 48 hours. At 72 hours media was removed, cells were washed twice with DPBS, and live cells were stained with calcein AM, which is hydrolyzed to the fluorescent molecule calcein by intracellular esterases. Quantification of live cells was accomplished with a Biotek Synergy Mx microplate reader (Biotek, Winooski, VT) by measuring the fluorescent intensity of calcein (ex/em 495 nm/517 nm). Relative viability was calculated as the ratio of the mean fluorescence intensity to that of the control, which contained media only.

5.2.11 Statistics

All experiments were performed in at least triplicate. The aerosolization studies were experimentally designed by Design Expert™ 8.0.7.1 software (Stat-Ease Corp., MN, USA). SigmaPlot 12.3 was used for one-way ANOVA tests and when statistically difference was observed a Holm-Sidak test was used to determine any significance in observed data. A p-value of <0.05 was considered statistically significant.

5.3 Results and Discussion

5.3.1 Physicochemical Characterization

Inhalable ACA powders obtained from spray drying experiments were examined via scanning electron microscopy (SEM) and showed spherical particle morphology and relatively uniform geometric size distribution (Figures 5.1 & 5.2). High mag images showed varying surface characteristics for the powders spray dried in water with the MC10 powder appearing to have small uniform crystals agglomerated together into the composite as opposed to MC0, which displayed fibrous looking crystals. The fibrous crystals in the MC0 powder appear tightly packed together thereby yielding a smoother surface than the MC10 particles. Additionally, the particles from the MC10 powder, although spherical, displayed more deviation in their morphology than the MC0 particles, which were extremely uniform in spherical morphology.

The ME10 and ME0 powders (spray-dried in methanol) showed more continuous/homogeneous appearing surfaces wherein the borders of individual crystals are not evident. Additionally, the spherical morphology of the particles was less consistent than particles spray dried in water and some of the particles in the ME0

powder displayed indentions in their surface. The particles in the ME10 powder do not display these indentions but their spherical morphology is even more irregular than the ME0 powder with apparent fusing together of individual particles. The difference in surface roughness, indentations, and particle morphology in mannitol based particles has been described previously (Littringer, Mescher et al. 2012, Littringer, Noisternig et al. 2013).

The geometric diameter of the inhalable dry powders systems was determined by analyzing SEM images ImageJ® and these results are reported in Table 5.2. As expected, the mean diameter of the particles in the MC0 powder ($1.10 \pm 0.58 \mu\text{m}$) were significantly larger ($p < 0.001$) than the particles in the ME0 powder ($0.63 \pm 0.29 \mu\text{m}$) due to higher surface tension of water relative to methanol. However, the addition of sodium chloride and cisplatin in the MC10 formulation lead to particles with a geometric diameter of $0.69 \pm 0.31 \mu\text{m}$, which was significantly smaller ($p < 0.001$) than the diameter of the MC0 particle. The reduction in particle size is likely due to density of sodium chloride resulting in a tighter packing of crystalline material for a given droplet from the nozzle of the spray dryer. The geometric diameter of the ME0 and ME10 powders were not statistically different.

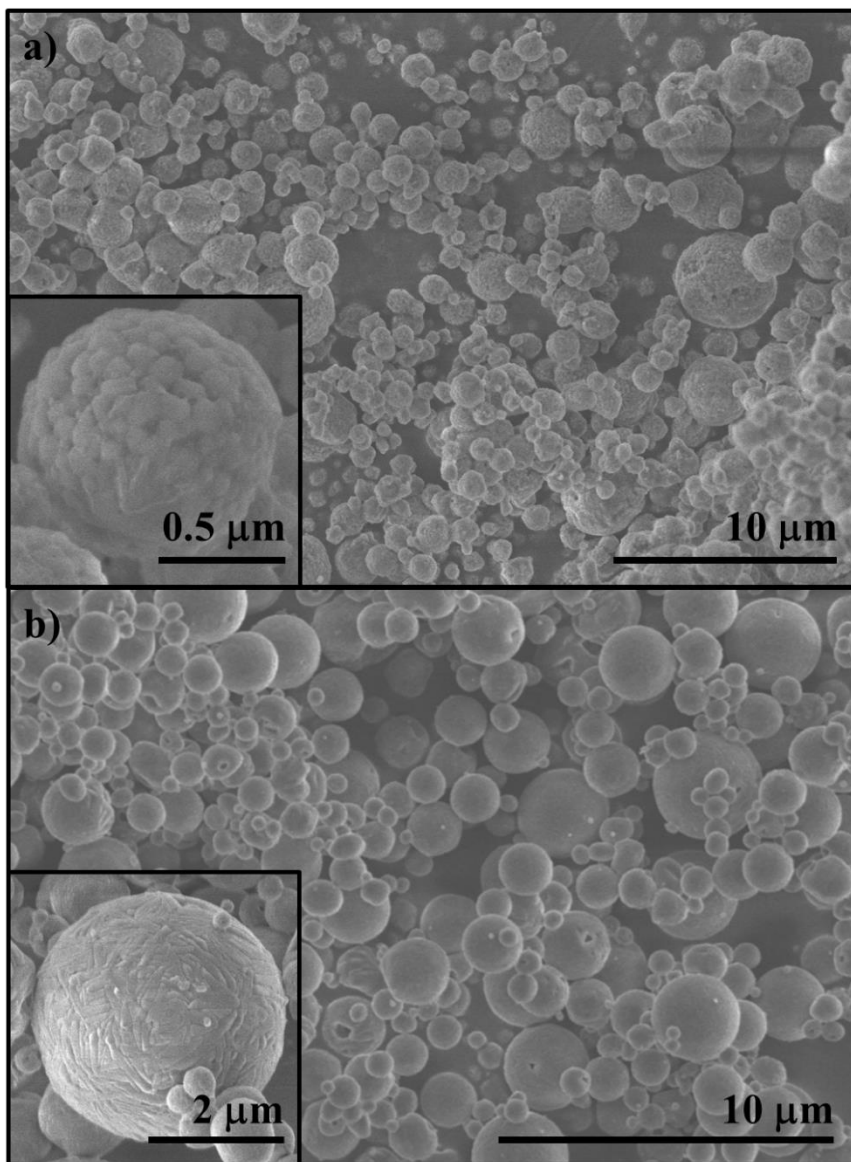


Figure 5.1: Representative SEM images of a) MC0 and b) MC10 at magnification of 5,000x with inset at 30,000x

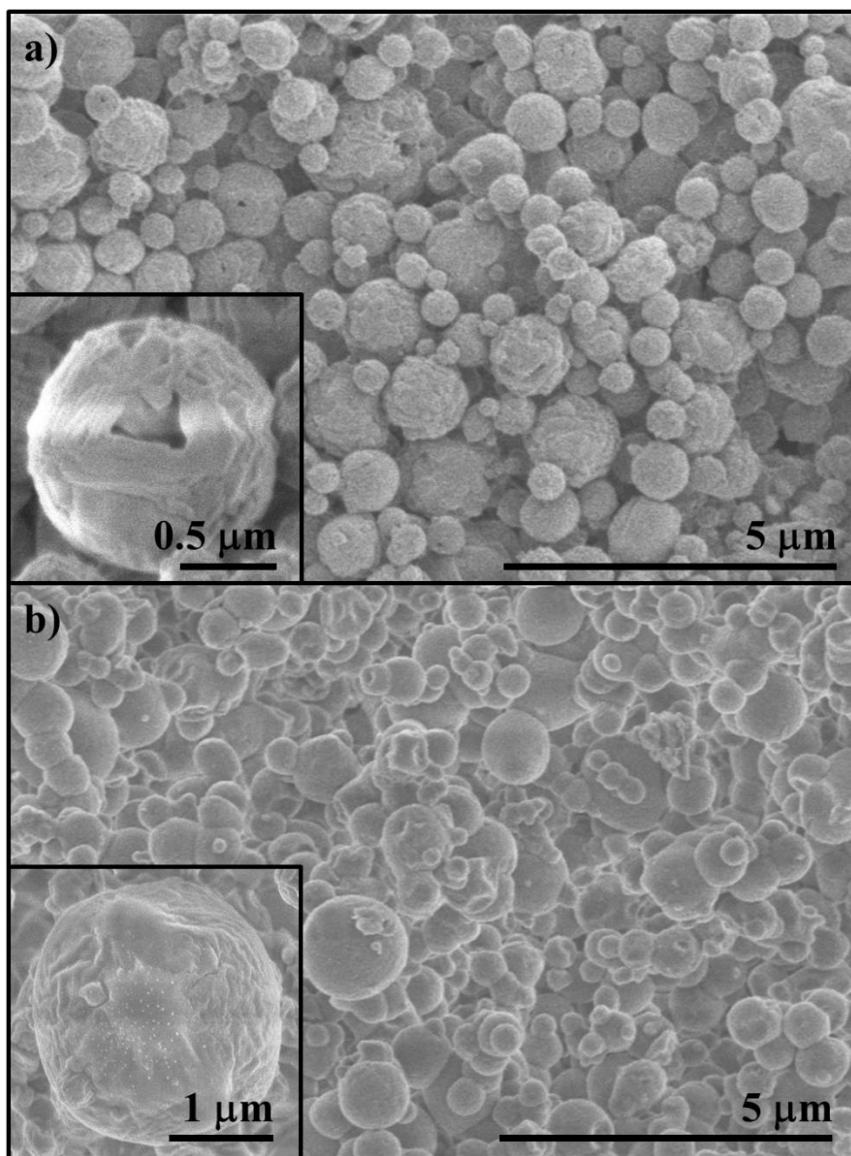


Figure 5.2: Representative SEM images of a) ME0 and b) ME10 at magnification of 5,000x with inset at 30,000x

The loading of cisplatin in the MC10 powder was determined through ICP-OES quantification of platinum in solutions of MC10. The platinum concentration, in combination with the molecular weight of cisplatin, was used to back calculate a loading of $10.0\% \pm 0.0\%$ in the MC10 powder indicating a very controllable capability for these

powders (this value is represented with n=1). The loading of erlotinib was quantified through UV/Vis spectroscopy and the results indicated a drug loading of $9.7\% \pm 0.5\%$ in the ME10 powder. These results are summarized in Table 5.2 and were utilized in determining concentrations for cell studies.

Table 5.2: Diameter from SEM and drug loading

System	Diameter (μm)	Drug_{feed} (wt%)	Drug_{actual} (wt%)
MC0	1.10 ± 0.58	0	0
MC10	0.69 ± 0.31	10	$10.0\% \pm 0.0\%$
ME0	0.63 ± 0.29	0	0
ME10	0.57 ± 0.21	10	$9.7\% \pm 0.5\%$

Figure 5.3 shows the XRD patterns for the MC0 and M10 powders and reveals long-range order in both powders. Interestingly, the diffractogram for the MC10 powder shows strong peaks associated with the structure of sodium chloride (labeled with dagger) and only a few other peaks, which match peaks from raw cisplatin (labeled with double dagger) but are relatively weak (Kondo and Adachi 2013). None of the mannitol peaks seen in M0 show up in the MC10 but it is possible that the small peaks attributed to cisplatin arise from a different polymorph of D-mannitol than that of M0 since D-mannitol has three separate polymorphs (Fronczek, Kamel et al. 2003, Zhang, Ngoc et al. 2015). These findings support our suggestion that the addition of the sodium chloride

leads to large changes in particle diameter by considerably altering the crystallinity of the particles. Conversely, the ME0 and ME10 powders have very similar patterns that closely resemble D-mannitol and erlotinib peaks (Figure 5.4).

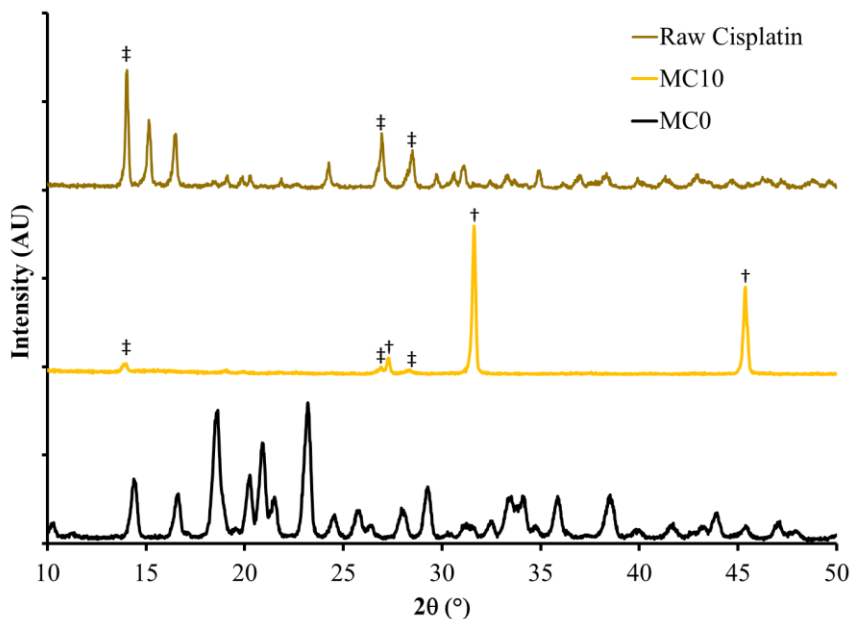


Figure 5.3: XRPD diffractograms for raw cisplatin (top), MC10 (middle) and MC0 (bottom)

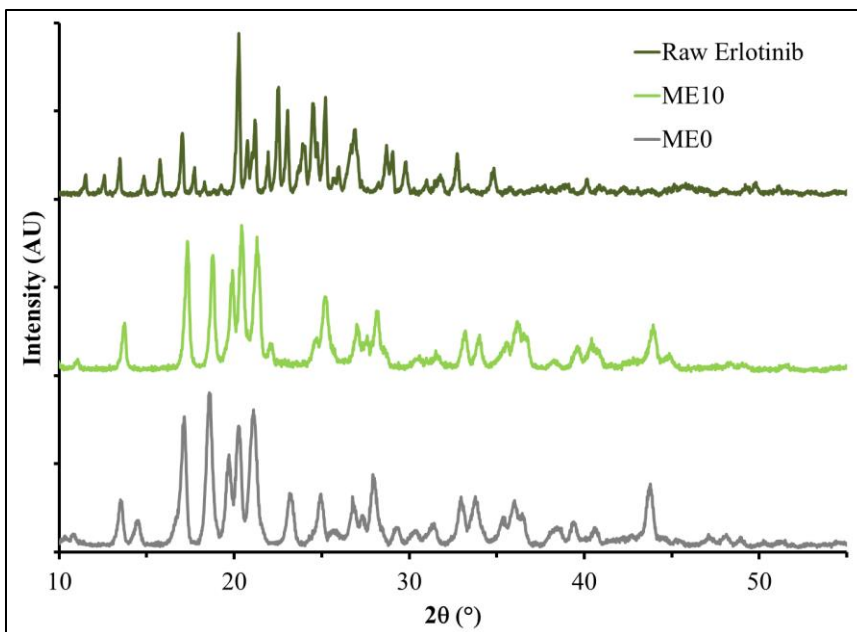


Figure 5.4: XRPD diffractograms for raw erlotinib (top), ME10 (middle) and ME0 (bottom)

The DSC thermograms for the MC0, MC10, ME0 and ME10 powders (Figure 5.5 & 5.6) reveal a large range of thermal stability as evident by no thermal phase transitions of the composites between 0°C and approximately 150 °C. The absence of a glass transition at 13 °C as well as crystallization peaks at 25 and 65 confirm that no amorphous D-mannitol is present in any of the four powders (Zhang, Ngoc et al. 2015). The MC10 powder shows a peak for the melting of D-mannitol that is shifted to a lower onset temperature relative to the control M0 and, again, suggests changes in crystallinity due to incorporation of cisplatin and sodium chloride. Interestingly this shift in the onset melting temperature results in a melting temperature that is lower than any of the three polymorphs of D-mannitol with the lowest being 155 °C for the δ form. The ME10

powder shows the same melting peak for D-mannitol at ~160°C but a shift in the peak associated with melting of erlotinib suggesting polycrystallinity.

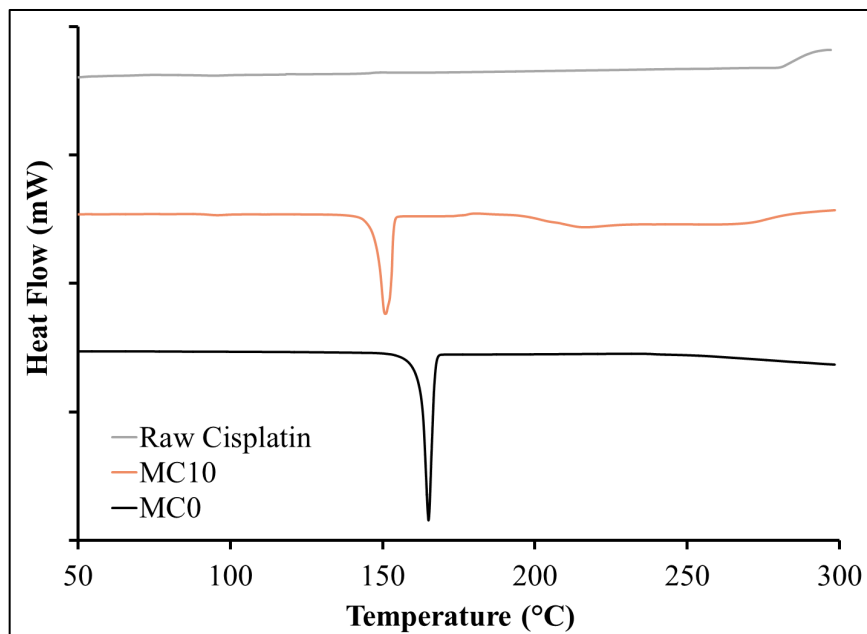


Figure 5.5: DSC thermograms for raw cisplatin, MC10, and MC10

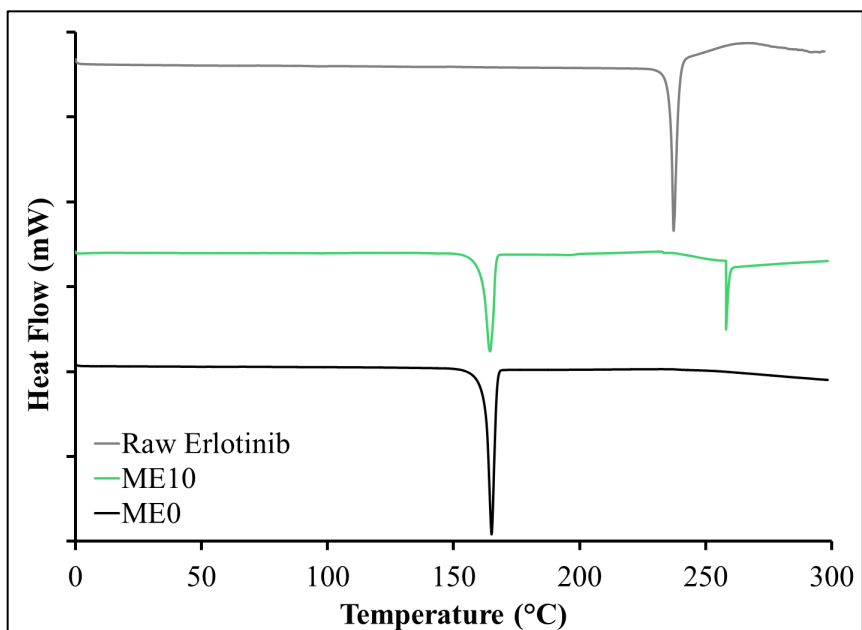


Figure 5.6: DSC thermograms for raw erlotinib, ME0, and ME10

5.3.2 Aerosol performance of inhalable powders

The aerosol performance of the inhalable ACA powders was determined with cascade impaction studies carried out using the Next Generation Impactor®. All powders showed good aerosol performance as evident by their aerosol performance properties summarized in Table 5.3. Figure 5.7 shows the deposition pattern for the MC0 and MC10 powders spray dried in water and shows good deposition of powders across all stages. These results suggest the ability of these powders to reach all areas of the lungs and indicate the potential of these materials for delivering cisplatin to the lungs in dry powder form with a composition similar to that administered clinically (1984). Additionally, the shape of these deposition patterns is typical for NGI studies and reveals primary particle agglomeration leading to high deposition on Stage 1 (and below). Surprisingly, the mass median aerodynamic diameter (MMAD) of the MC10 powder

($3.59 \pm 0.43 \mu\text{m}$) was statistically no different from that of the MC0 powder ($3.00 \pm 0.21 \mu\text{m}$) despite a large difference in geometric diameter. This can be explained by the well-known relationship shown in equation 4:

$$d_A \cong d_V \sqrt{\frac{\rho}{\chi\rho_0}} \quad (\text{Equation 5.3})$$

Where d_A is the aerodynamic diameter, d_V is the volume-equivalent diameter, ρ_0 is the particle density and χ is the dynamic shape factor. Hence, the increase in density and deviation from spherical morphology seen in the MC10 particles offset the significantly larger MC0 particles.

Figure 5.8 shows the aerosol dispersion performance plot for the ME0 and ME10 powders and reveals increased primary particle agglomeration (Figure 5.8) for these powders relative to powders spray dried in water. The increase in primary particle agglomeration contributed to larger MMAD values for the ME0 ($4.92 \pm 2.50 \mu\text{m}$) and ME10 ($5.64 \pm 1.32 \mu\text{m}$) powders although the ME0 powder is similar to previous reports from our lab group (Stocke, Meenach et al. 2014). Importantly to note, these studies were performed in the absence of a carrier (such as lactose) and many reports have shown the ability of larger carriers to improve aerosol performance of powders by allowing primary particles to bind to their surface and shear off during aerosolization thereby reducing primary agglomerates.

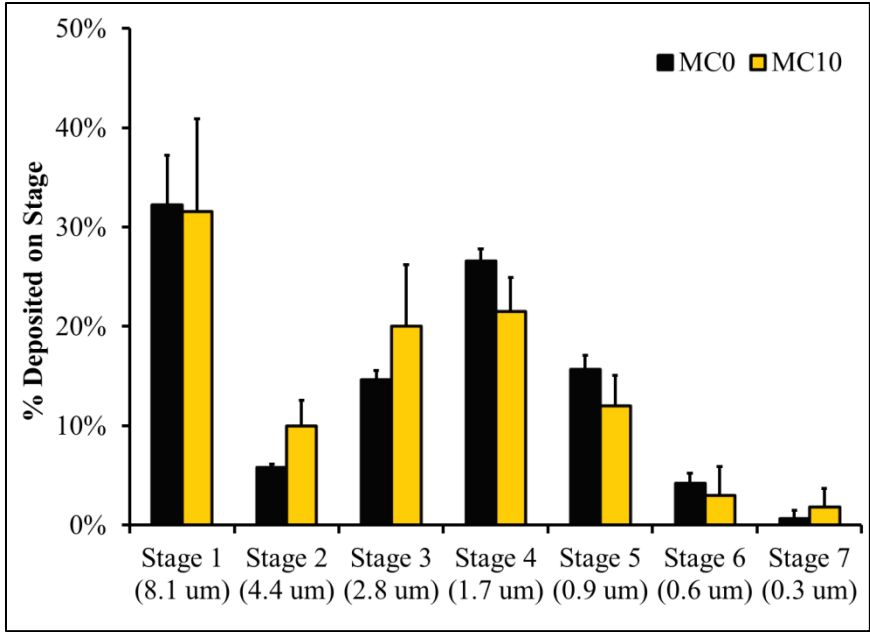


Figure 5.7: Aerosol dispersion performance plot for MC0 and MC10 powders

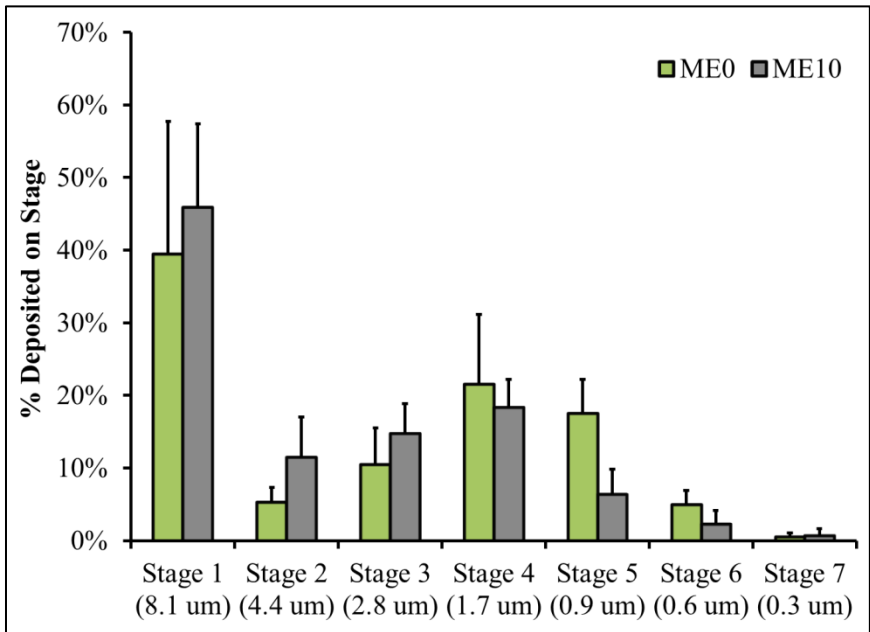


Figure 5.8: Aerosol dispersion performance plot for ME0 and ME10 powders

Table 5.3: Aerosol performance properties for inhalable MnMs (mean \pm std. dev.).

	<u>MC0</u>	<u>MC10</u>	<u>ME0</u>	<u>ME10</u>
MMAD (μm)	3.00 \pm 0.21	3.59 \pm 0.43	4.92 \pm 2.50	5.64 \pm 1.32
GSD (μm)	2.09 \pm 0.04	2.38 \pm 0.50	2.8 \pm 0.49	2.4 \pm 0.53
FPF (%)	32.3 \pm 5.7	31.1 \pm 11.4	25.7 \pm 5.0	28.0 \pm 4.6
RF (%)	65.0 \pm 9.1	56.5 \pm 9.7	67.9 \pm 6.3	61.2 \pm 10.9
ED (%)	73.5 \pm 6.9	78.8 \pm 8.1	79.3 \pm 4.4	86.9 \pm 8.8

5.3.3 *In vitro* activity of ACAs

Two human lung cancer cell lines, A549 human lung adenocarcinoma and H358 bronchioalveolar carcinoma, were used to examine the *in vitro* activity of the spray dried composites. Spray-dried ACAs were dissolved in media and the viability curves of cells exposed to inhalable ACAs for 24 hours were compared with the equivalent studies containing the raw form of the drug. Figure 5.9 shows the viability of A549 (a) and H358 (b) cells in the presence of raw cisplatin and MC10. The viability curve of cells exposed to cisplatin released from MC10 powder is the same as the cytotoxic profile for the raw form of the drug. Additionally, Figure 5.10 shows that erlotinib released from ME10 has the same activity in inhibiting growth of cells as evident by a drop in the relative viability of cells treated with erlotinib. These results confirm the hypothesis that ACAs can be spray dried into inhalable composites and upon dissolution release drugs with the same activity as their respective raw forms.

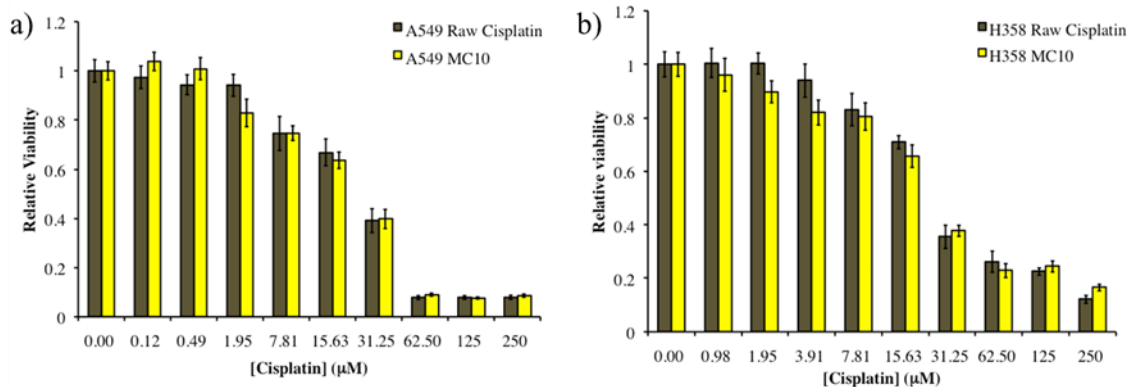


Figure 5.9: *In vitro* comparison of raw cisplatin and MC10 in human lung cancer cell lines A549 (left) and H358 (right)

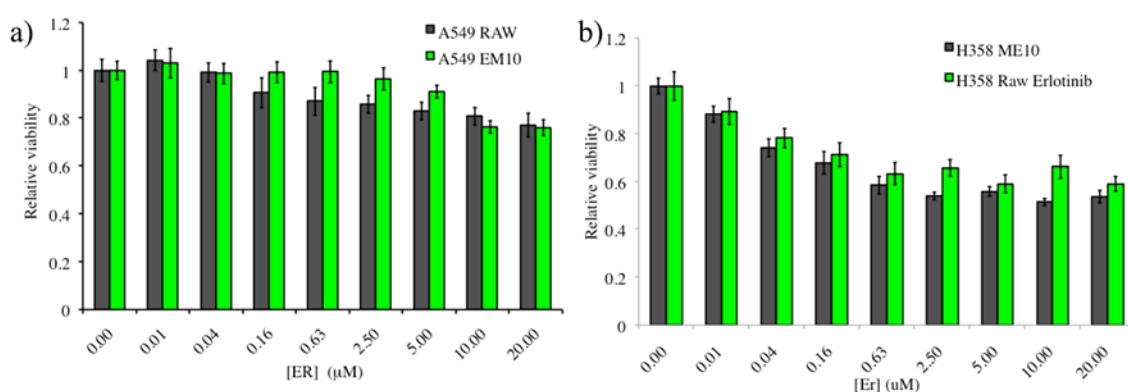


Figure 5.10: *In vitro* comparison of raw erlotinib and ME10 in human lung cancer cell lines A549 (left) and H358 (right)

Additionally, these findings suggest the potential for pulmonary delivery of agents traditionally administered systemically (cisplatin intravenously and erlotinib orally). The potential of these inhalable systems to target the delivery of ACAs to the lungs could represent a potential improvement of current treatment modalities for certain patients. Bronchioloalveolar carcinoma (BAC) is a form of adenocarcinoma that has a prevalence of about 5% among NSCLC cases and this particular neoplastic classification

has a higher likelihood of response to epidermal growth factor receptor (EGFR) tyrosine kinase inhibitors (TKIs) such as erlotinib (Jackman, Chirieac et al. 2005, Arenberg 2011). A lung tumor classified as BAC must be non-invasive with a pure lepidic spreading pattern making it a logical target for topical administration of anticancer agents ACAs through pulmonary delivery. The localization of inhalable ACAs to the affected organ through inhalation could show benefit for a large variety of lung cancers, and we recognize that BAC represents a class of tumors that potentially shows significant advantages from a treatment such as this.

5.4 Conclusions

Inhalable powders consisting of two common ACAs, cisplatin and erlotinib, were successfully formulated by spray drying. The surface roughness, morphology, and size of the particles was examined with SEM imaging and showed a significant difference in the size of mannitol spray dried in water (MC0) versus methanol (ME0). Additionally, the MC10 powder, containing 40% sodium chloride, displayed particles with rougher surfaces, smaller geometric diameter, and more irregular spherical particle morphology. The aerodynamic performance of the powders revealed good aerosol performance for the powders in absence of a lactose carrier although the ME10 powder displayed the poorest aerodynamic behavior. Cell studies with human lung cancer cell lines confirmed that the ACAs incorporated into inhalable powders retained their activity upon release into media and confirmed the potential of these systems for future development.

Chapter 6 Responsive Hydrogel Nanoparticles for Pulmonary Delivery

The chapter is taken directly or adapted from work **published** in **Stocke et al. (2015)** Copyright 2015 Elsevier B.V. Used with permission from Nathanael A Stocke, Susanne M. Arnold, and J. Zach Hilt.

6.0 Abstract

Nanoparticles represent one of the most widely studied classes of advanced drug delivery platforms in recent years due to a wide range of unique properties and capabilities that can be utilized to improve upon traditional drug administration. Conversely, hydrogel nanoparticles (HNPs) – also called nanogels – represent a unique class of materials that combine the intrinsic advantages of nanotechnology with the inherent capabilities of hydrogels. Responsive hydrogels pose a particularly interesting class of materials that can sense and respond to external stimuli and previous reports of inhalable hydrogel particles have highlighted their potential in pulmonary delivery. Here, we synthesized two different pH-responsive HNPs, designated HNP120 and HNP270, by incorporating functional monomers with a common crosslinker and characterized their physicochemical properties. One of the HNP systems was selected for incorporation into a composite dry powder by spray drying, and the aerodynamic performance of the resulting powder was evaluated. The HNP120s displayed a hydrodynamic diameter of approximately 120 nm in their fully swollen state and a minimal diameter of around 80 nm while the HNP270s were approximately 270 nm and 115 nm, respectively. Electron microscopy confirmed particle size- and morphological uniformity of the HNPs. The

HNP120s were spray dried into composite dry powders for inhalation and cascade impaction studies showed good aerosol performance with a mass median aerosol diameter (MMAD) of $4.82 \pm 0.37 \mu\text{m}$ and a fine particle fraction $> 30\%$. The HNPs released from the spray dried composites retained their responsive behavior thereby illustrating the potential for these materials as intelligent drug delivery systems that combine the advantages of nanotechnology, lung targeting through pulmonary delivery, and stimuli-responsive hydrogels.

6.1 Introduction

Over the last few decades, exhaustive efforts have focused on developing advanced drug delivery systems for improved therapeutic efficacy, enhanced patient compliance, and optimal drug safety profiles (Peer, Karp et al. 2007). Nanoparticles represent one of the most widely studied classes of advanced drug delivery platforms with more than 25,000 publications over the last 10 years (Anselmo and Mitragotri 2014). Local delivery, environmental sensing, and responsive behavior are a few properties of nanoparticulate drug delivery systems that can be utilized to improve upon traditional drug administration (Courrier, Butz et al. 2002, Brannon-Peppas and Blanchette 2004, Liu and Tang 2010, Coto-Garcia, Sotelo-Gonzalez et al. 2011, Baeza, Colilla et al. 2015). Conversely, hydrogel nanoparticles (HNPs) – also called nanogels – represent a unique class of materials that combine the intrinsic advantages of nanotechnology with the inherent capabilities of hydrogels (Hamidi, Azadi et al. 2008, Oh, Drumright et al. 2008).

Generally, hydrogels are defined as three-dimensional polymeric networks composed of hydrophilic moieties and possess the ability to imbibe large quantities of water (Peppas, Bures et al. 2000). Though traditionally made at the macroscopic scale, hydrogels possess unique characteristics that are promising for nanoformulations. The high water content of hydrogels results in materials that resemble living tissues and contributes to the success of many hydrogel applications in research and medicine (Rosiak and Yoshii 1999, Soppimath, Aminabhavi et al. 2002, Peppas, Hilt et al. 2006). While many of these applications center around gels at equilibrium (e.g. contact lenses), researchers have elicited a variety of mechanisms by which to control hydrogel behavior resulting in intelligent materials with great potential in drug delivery.

Responsive hydrogels have been examined thoroughly over the past several years and researchers have used a variety of approaches to achieve desired functionality (Gupta, Vermani et al. 2002). By incorporating various monomers, crosslinkers, and synthesis conditions one can tune the hydrogel to respond in a variety of manners including degradation of the hydrogel network or swelling/shrinking of the gel (Ghandehari, Kopeckova et al. 1997, De, Aluru et al. 2002). Additionally, the response of the hydrogel can be initiated by a variety of external stimuli such as heat, specific analytes, and changes in pH and these particles have potential in pulmonary administration, which has shown promise for nanoparticle and drug delivery to the lungs (Soppimath, Aminabhavi et al. 2002, Yang, Peters et al. 2008, Anthony J. and Mansour 2009).

Previous reports of delivering hydrogel particles to the lungs via pulmonary administration demonstrated the ability to engineer micron-sized hydrogel particles that

can be delivered to the lungs as stand-alone carriers (El-Sherbiny and Smyth 2010, Du, El-Sherbiny et al. 2014, Secret, Kelly et al. 2014). Liquid aerosols of hydrogel micro- and nanoparticle suspensions were also accomplished using metered dose inhalers and nebulizers (Farhat, Holloway et al. 2009, Selvam, El-Sherbiny et al. 2011). Additionally, the *in vivo* administration of 220 nm nanogels showed sustained release of a model peptide after pulmonary administration, thereby illustrating the potential of HNPs administered via inhalation (Lee, Lee et al. 2012).

Here, we synthesized pH-responsive HNPs and characterized some of their physicochemical properties. The responsive behavior of these HNPs was achieved by incorporating functional monomers with a common crosslinker. Specifically, pH responsive HNPs were formed by polymerizing methacrylic acid (MAA) with poly(ethylene glycol) (n=400) diacrylate (PEG400DA). Dynamic light scattering was used to examine the change in hydrodynamic diameter of two different HNP systems as a function of pH and electron microscopy confirmed particle size- and morphological uniformity. Additionally, one of the HNP systems was selected for incorporation into a composite dry powder by spray drying and the aerodynamic performance of the resulting powder was evaluated. The characteristics of the HNPs released from this inhalable powder were examined and compared to the HNPs as synthesized.

6.2 Material and methods

6.2.1 Materials

Acrylic acid (AA), poly(ethylene glycol) 400 (PEG400DA) diacrylate, 9-anthracenylmethyl methacrylate (9AM), sodium dodecyl sulfate (SDS). Hydrochloric

acid (HCL), Sodium Hydroxide (NaOH). Phosphate buffer saline (PBS) and acetic acid buffer (AAB) stock solutions were made at a concentration of 100 mM and an ionic strength of 1540 mM with sodium phosphate glacial acetic, respectfully. Ionic strength of buffers were adjusted with sodium chloride (fisher). For pH adjustments hydrochloric acid (Fisher) and sodium hydroxide were mixed with DI water to a final concentration of 0.1 M. Sigma-Aldrich (St Louis MO), Fisher Scientific (Pittsburgh, PA). Scott-Gross (Lexington, KY). ATTC (Manassas, VA). Life Technologies (Grand Island, NY).

6.2.2 Synthesis of responsive hydrogel nanoparticles

Responsive hydrogel nanoparticles were prepared with acrylic acid (AA), poly(ethylene glycol) 400 (PEG400DA) diacrylate, and 9-anthracenylmethyl methacrylate (9AM) in an aqueous solution of sodium dodecyl sulfate (SDS) . The molar ratio of AA:PEG400DA was 80:20 and 1mol% 9AM was incorporated based on total monomer weight. Briefly, Acrylic acid was weighed into a 15 mL centrifuge tube and 9AM was dissolved into this liquid monomer. Subsequently, PEG400DA was weighed into a separate 15 mL centrifuge tube. SDS was dissolved in 100 mL of DI water and added to a 500 mL round bottom flask. A mechanical stir bar and a MODEL 260 J KEM Digital Temperature Controller were used during the experiment, which was carried out for 45 mins at 100 rpm and 45°C. The reaction mixture was via dialysis for 72 hours. Two different HNP systems were synthesized by changing the SDS concentration and were labeled HNP120s and HNP270s corresponding to SDS concentrations of 3.0 mM and 1.5 mM, respectively.

6.2.3 Electron microscopy and particle sizing

Scanning electron microscopy (SEM) was performed with a Hitachi S4300 microscope (Tokyo, Japan). Three milliliters of HNP solutions were transferred to a weigh boat and allowed to evaporate under mild heating on a hot plate. Double-sided adhesive carbon tabs were adhered to aluminum studs (Ted Pella, Redding, CA) and blotted on dried HNPs. Samples were coated with a thin film of a gold/palladium alloy using an Emscope SC400 sputter coating system at 20 mA for 1 minute under argon gas. For all electron microscopy experiments at least 3 independent samples were examined and multiple images were examined for each sample. ImageJ[®] software (NIH, Bethesda, MD) was used to measure particle diameter in multiple ($n > 3$) representative images.

6.2.4 Colloidal stability of HNPs

The colloidal stability of the HNPs was determined via UV/vis spectroscopy. HNPs were dispersed in 10 mM PBS at 0.5 mg/mL and adjusted to desired pH with 0.1 M HCl or NaOH solutions. After adjusting the pH, the suspensions were transferred to a quartz cuvette and scanned from 200 nm to 800 nm in order to insure no maxima or minima occurred near desired wavelength of 600 nm, hence absorption is due to light scattering from nanoparticles. A separate quartz cuvette was filled with 10 mM PBS and used as a blank for the measurements, which were taken every 5 minutes for 12 hours at 600 nm. The stability was calculated by normalizing the absorption at time t to the initial absorption and the data were plotted in excel.

6.2.5 pH response of HNP diameter with dynamic light scattering

Dynamic light scattering was used to measure the hydrodynamic diameter of HNPs at varying pH conditions. HNPs were first dispersed in 10 mM PBS at a concentration of 0.5 mg/mL and the pH was titrated to a range of values with 0.1 M HCl and 0.1 M NaOH. At each pH value a sample of the mixture was placed in a disposable cuvette and placed into a [model] Malvern ZetaSizer®. The z-averaged diameter of these particles was recorded

6.2.6 pH response of HNP diameter with dynamic light scattering

Dynamic Light Scattering (DLS) was performed to determine the hydrodynamic diameter of the HNPs at varying pH values. Readings were performed in disposable cuvettes using a Malvern Instruments ZetaSizer® (Malvern Instruments, Malvern, United Kingdom). Aqueous dispersions were made with HNP and PBS concentrations of 200 □g/mL 10 mM, respectively and the pH was measured using a pH probe. For each measurement the pH was adjusted using 0.1 M HCl and NaOH, recorded, and then placed in ZetaSizer®.

6.2.7 Inhalable HNP composites from spray drying

Spray drying was accomplished with a Büchi Mini Spray Dryer B290 coupled with a B-295 Inert Loop and high-performance cyclone (all from Büchi Labortechnik, Flawil, Switzerland) using parameters previously optimized by our lab (Li and Mansour 2011). Spray drying experiments were carried out in closed mode using UHP dry nitrogen gas at a flow rate of 600 L/h, an inlet temperature of 150°C, and an aspirator rate

of 35 m³/h. Once the inlet temperature of 150°C was reached, pure methanol was fed to the spray dryer until the outlet temperature was stable. For feed mixtures, D-mannitol was dissolved in methanol and iron HNPs were subsequently dispersed such that the combined mass of these two components resulted in a dilute concentration of 0.1% wt/vol. The HNP concentration in the feed was 10wt% based on the combined mass of D-mannitol and HNPs. Five hundred milliliters of this mixture was fed to the spray dryer at a pump rate of 50% (15 mL/min) through a stainless steel nozzle with a diameter of 0.7 mm. Powders were collected and transferred to a glass desiccator over Drierite™ and stored in the freezer at -23°C.

6.2.8 Aerosol performance with the Next Generation Impactor™ (NGI™)

Impactor studies were carried out with a M170 Next Generation Impactor™ (MSP Corporation Shoreview, MN) in accordance with United States Pharmacopeia (USP) Chapter <601> specifications on aerosols (2006). The conditions for these experiments were previously reported (Meenach, Vogt et al. 2013, Wu, Zhang et al. 2013). The NGI was equipped with a stainless steel induction port (USP throat adaptor) attachment and specialized stainless steel NGI™ gravimetric insert cups (NGI Model 170, MSP Corporation, Shoreview, Minnesota). Type A/E glass fiber filters with diameter 55mm (Pall Corporation, NY) were placed on each stage of the impactor and weighed before and after the experiment to determine the particle mass deposited. Approximately 10 mg of powder was loaded into each clear hydroxypropyl methylcellulose, size-3 capsule (Quali-V®) (QUALICAPS, Spain) and these capsules were placed into a HandiHaler® DPI™ device (Boehringer Ingelheim Pharmaceuticals,

Inc. Ridgefield, CT) attached to a customized rubber mouth piece connected to the NGI™. Three capsules were loaded and released for each sample and experiments were performed in triplicate. The total dose for each sample was approximately 30 mg. A Copley HCP5 vacuum pump (Copley Scientific, United Kingdom) and a Copley TPK 2000 critical flow controller (Copley Scientific, United Kingdom) were used to produce a flow rate (Q) of 60 L/min in order to model the flow rate in a healthy adult lung. This flow rate was adjusted before each experiment using a Copley DFM 2000 flow meter (Copley Scientific, United Kingdom).

For Q=60 L/min, the aerodynamic cutoff diameters (D_{a50}) for each stage of the impactor were given from the manufacturer as: stage 1 (8.06 μ m); stage 2 (4.46 μ m); stage 3 (2.82 μ m); stage 4 (1.66 μ m); stage 5 (0.94 μ m); stage 6 (0.55 μ m); and stage 7 (0.34 μ m). The emitted dose (ED), respirable fraction (RF), and fine particle fraction (FPF) were calculated as follows:

$$ED \% = \frac{\text{Initial mass in capsules} - \text{Final mass in capsules}}{\text{Initial mass in capsules}} \times 100\% \quad (\text{Equation 6.1})$$

$$RF \% = \frac{\text{Mass of particles on stages 2-7}}{\text{Total particle mass on all stages}} \times 100\% \quad (\text{Equation 6.2})$$

$$FPF \% = \frac{\text{Mass of particles on stages 2-7}}{\text{Initial mass in capsules}} \times 100\% \quad (\text{Equation 6.3})$$

Additionally, the mass median aerodynamic diameter (MMAD) and geometric standard deviation (GSD) for the particles were determined using a Mathematica® program written by Dr. Warren Finlay (Finlay 2008).

6.3 Results and Discussion

Figure 6.1 includes a representation of the structure and responsive of the HNPs at varying pH conditions, and the responsive behavior of the synthesized HNPs was examined by measuring the hydrodynamic diameter of the particles as a function of pH (Figures 6.2 & 6.3). At higher pH values, the carboxylic groups in MAA along the hydrogel backbone are deprotonated providing a negative charge that stabilizes the particles and thus prevents agglomeration as illustrated in Figure 6.1. As pH is lowered the protonation of these functional groups results in less electrostatic repulsion between chains and intrastrand hydrogen bonding. Both of these mechanisms lead to the collapse, or deswelling, of the three dimensional network in the HNPs and therefore a reduction in the hydrodynamic diameter of the HNPs. Eventually, increasing the proton concentration results in a transition of particle behavior wherein interparticulate hydrogen bonds result in large agglomerates of particles leading to a massive increase in the hydrodynamic diameter of the particles. Interestingly, this behavior is reversible wherein raising the pH above the transition value thus giving these HNPs the unique ability to reversibly sense and respond to changes in their environment.

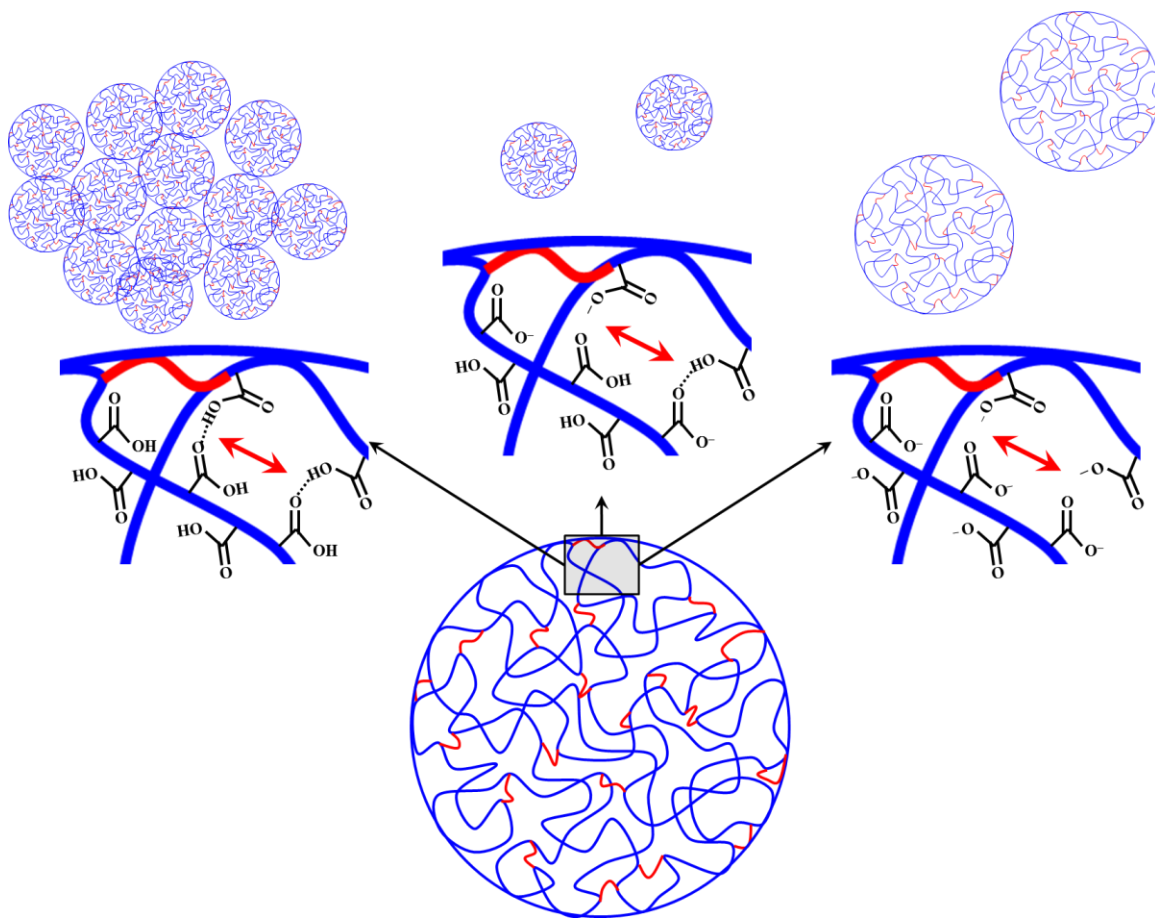


Figure 6.1: Representation of responsive hydrogel nanoparticles at varying pH conditions from low (left) to high (right).

The HNP120s (Figure 6.2) have a hydrodynamic diameter of approximately 120 nm in their fully swollen state and a minimal diameter of around 80 nm while the HNP270s (Figure 6.3) have a swollen diameter of approximately 270 nm with a minimum diameter of approximately 115 nm. Interestingly, the point at which these systems started agglomerating, the so-called transition pH, was different for the two HNPs systems as seen more clearly in Figure 6.4. The transition pH for both the HNP120 and HNP270 particles occurred near the pKa of methacrylic acid (4.65); however, the

HNP120s began to agglomerate at a higher pH than the HNP270s suggesting the ability to tune this transition based on both the monomer and the size of the HNPs. The shift in the transition pH is possibly explained by the larger ratio of surface

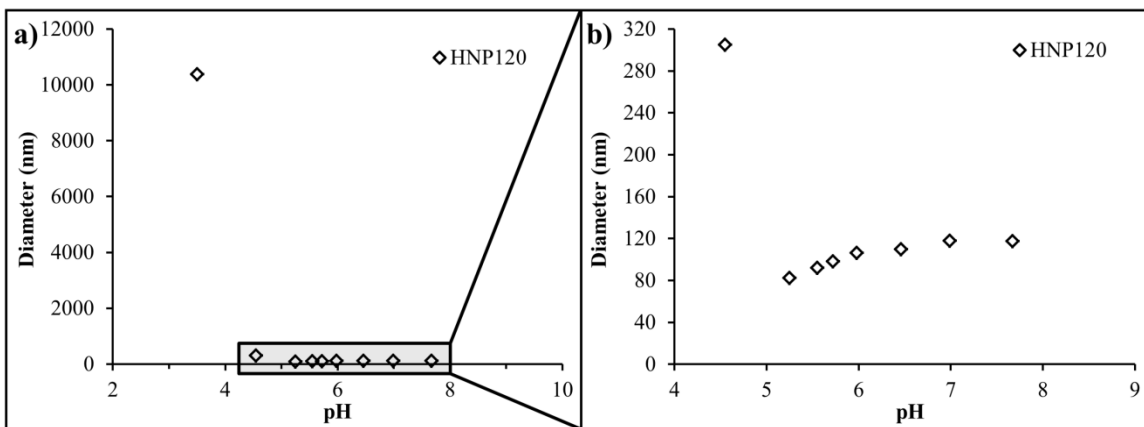


Figure 6.2: Hydrodynamic diameter of HNP120s a) over a large range of pH values and b) zoomed in above transition pH

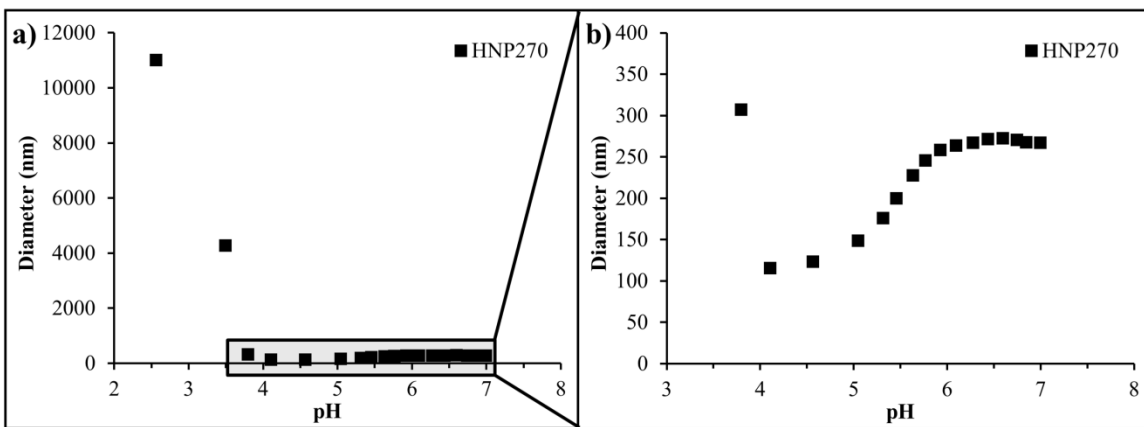


Figure 6.3: Hydrodynamic diameter of HNP270s a) over a large range of pH values and b) zoomed in above transition pH

area to volume in the HNP120s thereby making an agglomerated state more energetically favorable relative to the HNP270s. A more energetically favorable agglomerated state would result in less protonation of carboxylate groups, and therefore less interparticulate hydrogen bonding, necessary to overcome electrostatic repulsion of deprotonated carboxylic groups.

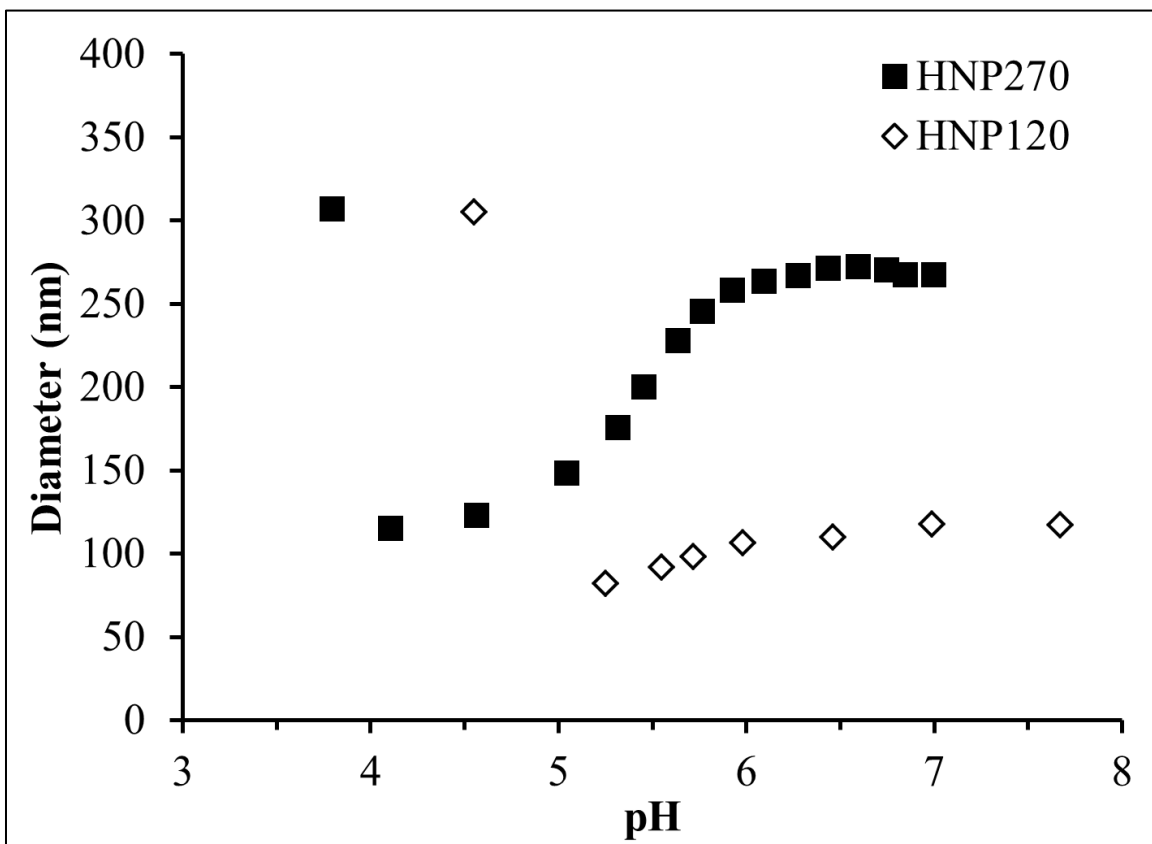


Figure 6.4: Hydrodynamic diameter of HNP120 (diamonds) and HNP270 (squares) showing difference in transition pH

Below the transition pH the HNP120 and HNP270 particles were extremely polydisperse with all of their PDI values > 0.35. These PDI values suggest agglomeration of the

particles and support our hypothesis of interparticulate hydrogen bonding as the mechanism driving agglomeration. However, above the transition pH the both HNP systems were very monodisperse with the PDI of all measurements > 0.09 . Interestingly, lowering the pH and introducing agglomerates is completely reversible by raising the pH of the system and presents a novel responsive behavior of these HNP systems that is both precise and reproducible. This reversible behavior further supports our hypothesis that the large agglomerates are indeed due to reversible and noncovalent interactions between HNPs.

Both HNP systems were examined with electron microscopy and these images confirmed their uniform size distribution (Figures 6.5 and 6.6). Figure 6.5 are representative images of individual HNPs showing a high degree of uniformity. Higher resolution SEM images (Figures 6.5b and 6.6b) show smooth surfaces on these nanoparticles and spherical particle morphology; however, upon drying the flexible HNPs pack together into large fibers causing the primary particles to slightly deviate from spherical morphology. ImageJ® was used to analyze the SEM images and measure the diameter of the HNPs in the dry state. The HNP120 and HNP270 particles displayed diameters in the dry state of $82.6 \text{ nm} \pm 4.3 \text{ nm}$ and $133.4 \text{ nm} \pm 12.2 \text{ nm}$, respectively and these values agree with the hydrodynamic diameter profiles of these systems.

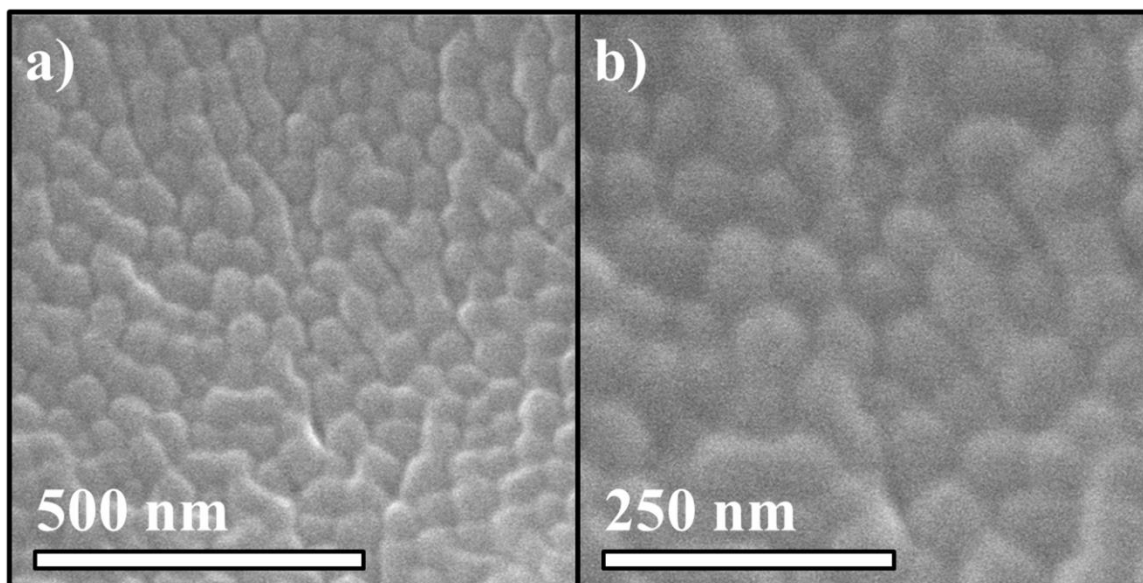


Figure 6.5: SEM images of HNP120s at a) x100k and b) x180k. ImageJ® size analysis shows $82.6 \text{ nm} \pm 4.3 \text{ nm}$

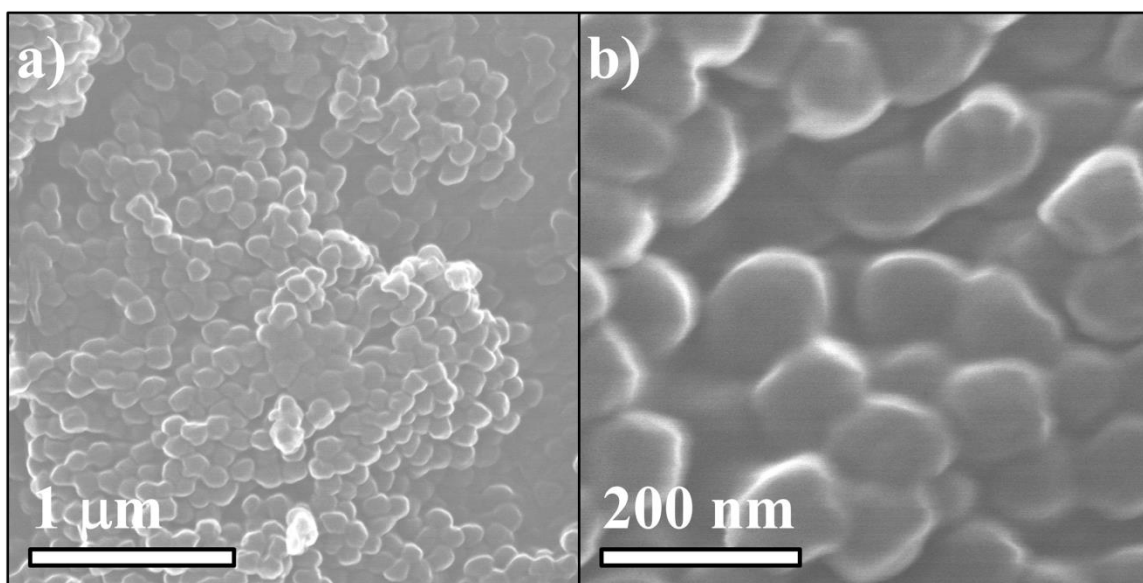


Figure 6.6: SEM images of HNP270s a) x35k and b) x150k. ImageJ® size analysis shows $133.4 \text{ nm} \pm 12.2 \text{ nm}$

After characterizing the size and responsiveness of two different HNP systems, the HNP120s were selected for incorporation into inhalable composites and were further characterized. Representative TEM images of the HNP120s (Figure 6.7) confirmed the spherical morphology of particles when allowed to attach to the TEM grid in dilute suspensions and thereby avoid morphological deformation due to surrounding particles upon drying. Additionally, high resolution TEM images (Figure 6.8) confirmed the amorphous character of these particles evident by the diffused peak in the selected area diffraction pattern (inset of Figure 6.8).

As a proof of concept, the HNP120s were loaded with a model chemotherapeutic agent, cisplatin, by imbibition with a cisplatin solution (Supplemental Figure B.1). In solution, cisplatin is solvated with water molecules and carries a slightly positive charge (1984). Hence, we hypothesized that cisplatin would accumulate in HNPs above their transition pH and not below it. Supplemental Figure B.1 shows the reduction in cisplatin concentration for HNPs at pH = 7 while no such decrease was seen at pH = 4 and the calculated loading of cisplatin $3.1\% \pm 0.2\%$ (mass cisplatin per mass of HNPs) for the HNP120s at pH =7. These data indicate that cisplatin selectively accumulates in these composites based on pH and suggests that this is due to electrostatic interactions. Additionally, these findings illustrate the potential for triggered drug release by reducing the pH and thereby eliminating the electrostatic interaction between cisplatin and the HNPs although these studies have not yet been performed.

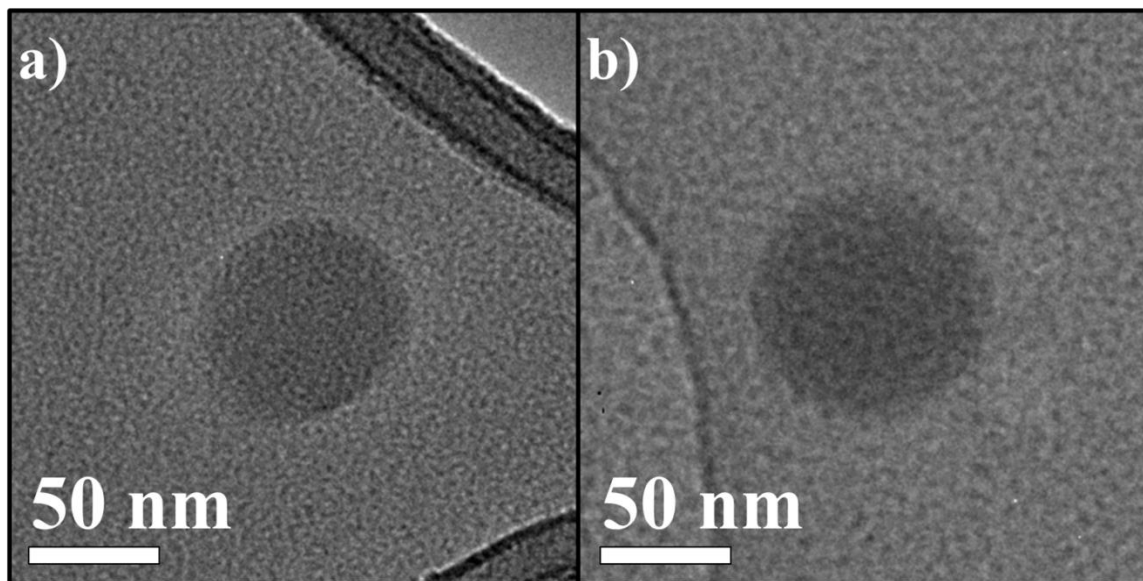


Figure 6.7: Representative TEM images of representative HNP120s on copper TEM grid illustrating spherical morphology and size uniformity. The diameters of two representative particles are: a) 80.7 nm and b) 88.7 nm

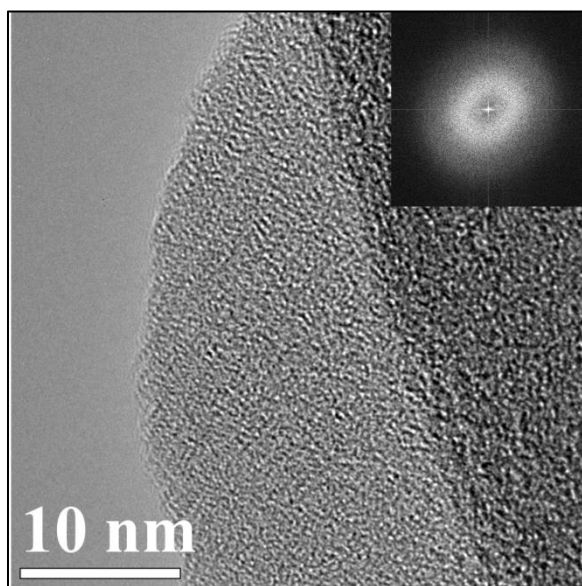


Figure 6.8: High mag (x500k) TEM image of individual HNP120 with fast Fourier Transform inset showing amorphous character of HNPs

The colloidal stability of these HNPs was examined above and below their transition pH in 10 mM PBS at an ionic strength of 154 mM, which is physiologically relevant (Stein, Whitlock et al. 1979). The data are presented in Figure 6.9 and show that above the transition pH the HNPs display excellent colloidal stability with no significant change in their relative absorption. Below the transition pH the HNP suspension is a relatively opaque and chalky mixture that continues to get more opaque with HNP agglomerate. This leads to an increase in relative absorption for approximately 2 hours. Eventually, these agglomerates become too large to remain in suspension and begin to crash out of suspension at approximately 120 mins.

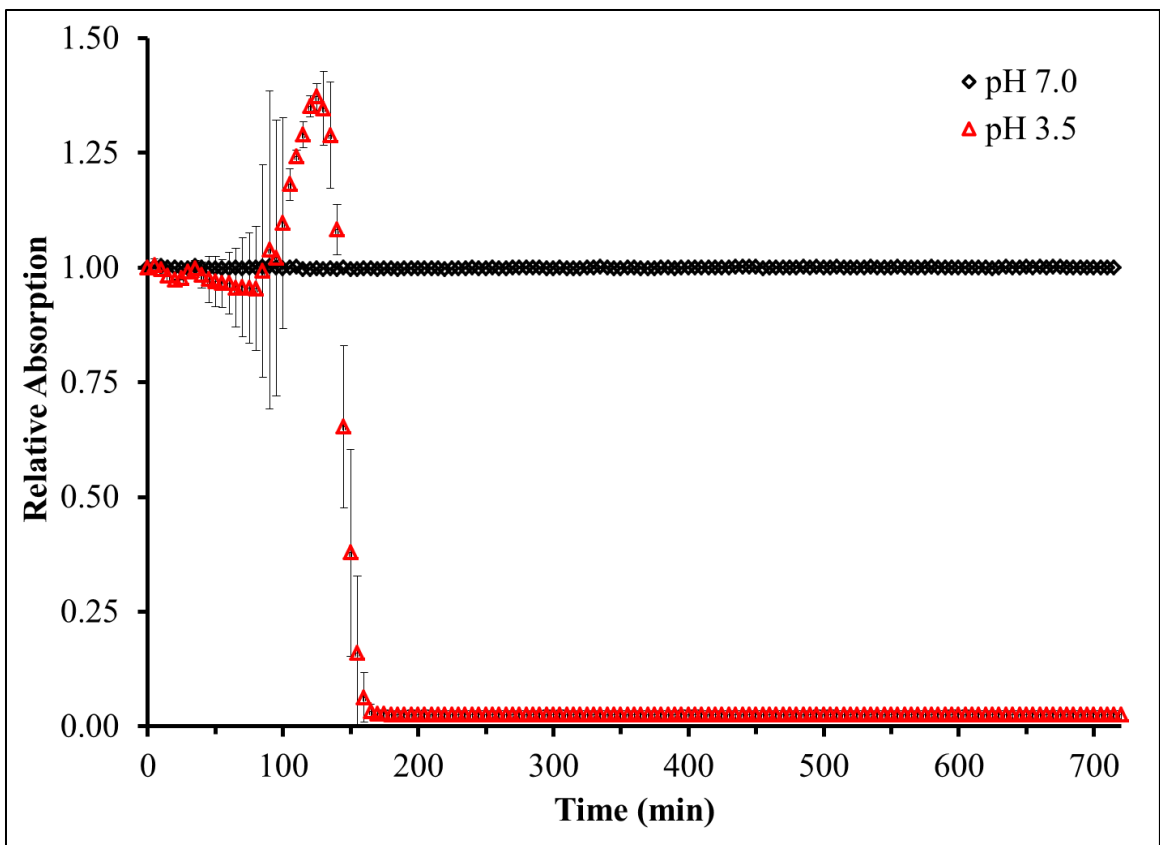


Figure 6.9: Stability of HNP120s above and below transition pH

After characterizing the size, responsiveness, and stability of the HNP120s, these particles were spray dried (SD) into a composite powder for inhalable purposes and this powder was designated SD HNP120. Figure 6.10 shows representative SEM images of these composites. The SD HNP120 composites exhibited spherical particle morphology and relatively uniform size distribution. The inset of an individual particle illustrates a relatively rough surface for these particles that could potentially affect the aerodynamic performance of this powder.

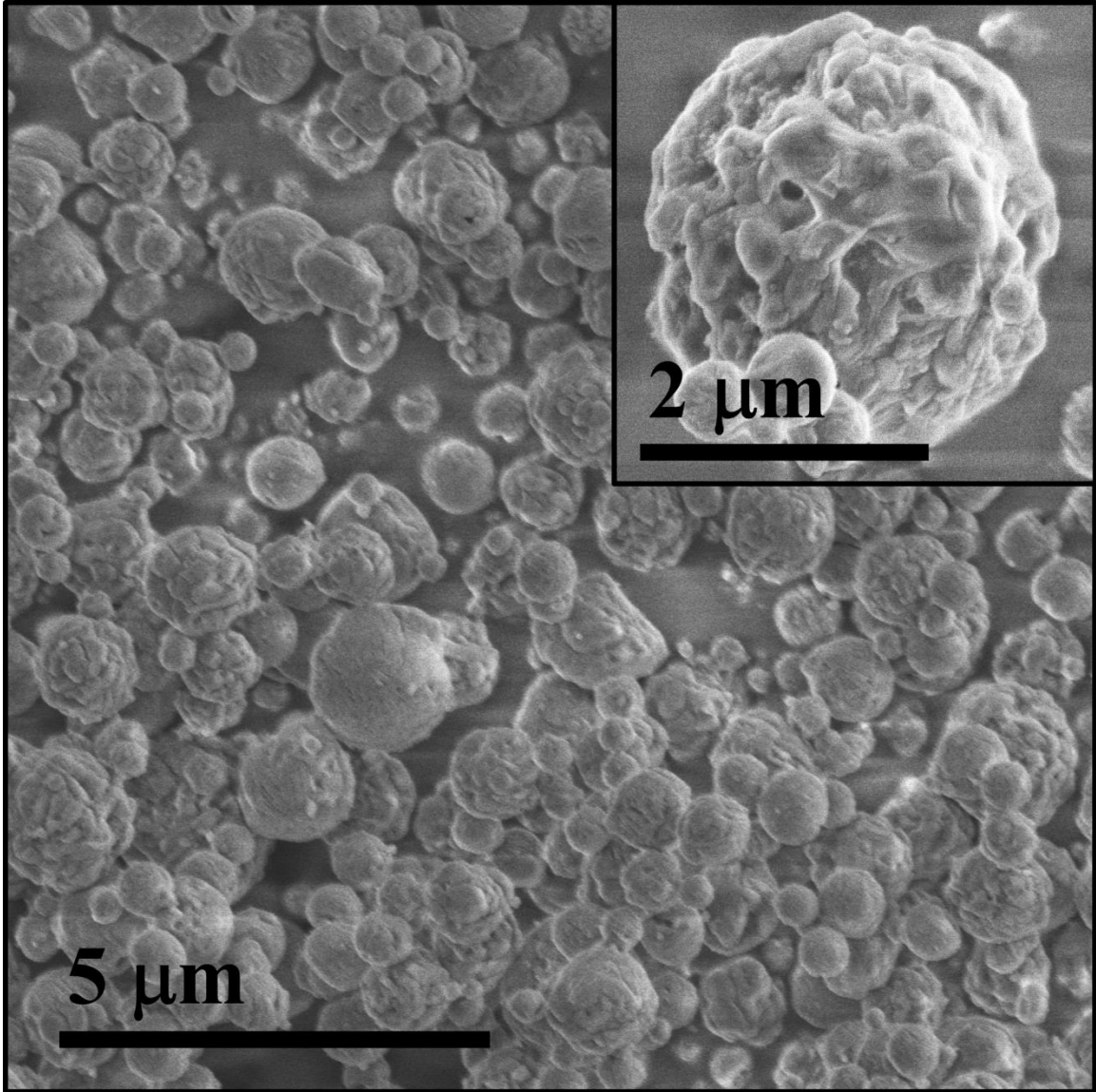


Figure 6.10: SEM image of SD HNP120 composite dry powder with individual particle shown in top right corner inset.

Cascade impaction studies were used to evaluate the aerodynamic performance of the HNP composite powders using the Next Generation Impactor[®]. Initial attempts at spray drying these composites in purely aqueous systems resulted in powders dissolving in the collection vial presumably due to diffusion of water still retained within the HNPs after

spray drying. Hence, the HNPs were dispersed in methanol and the resulting powders showed no sign of dissolution in the collection vial. The aerosol dispersion performance of the HNP composites (Figure 6.11) shows deposition of particles on all stages of the impactor and illustrates the potential of these materials to reach all regions of the lungs, even to the deepest alveolar region. The mass median aerodynamic diameter (MMAD) of the composite HNPs was $4.82 \mu\text{m} \pm 0.37 \mu\text{m}$, which falls within the generally accepted range of $1\text{-}5 \mu\text{m}$ for optimal aerodynamic performance. These values along with other aerodynamic performance parameters are reported in Table 6.1.

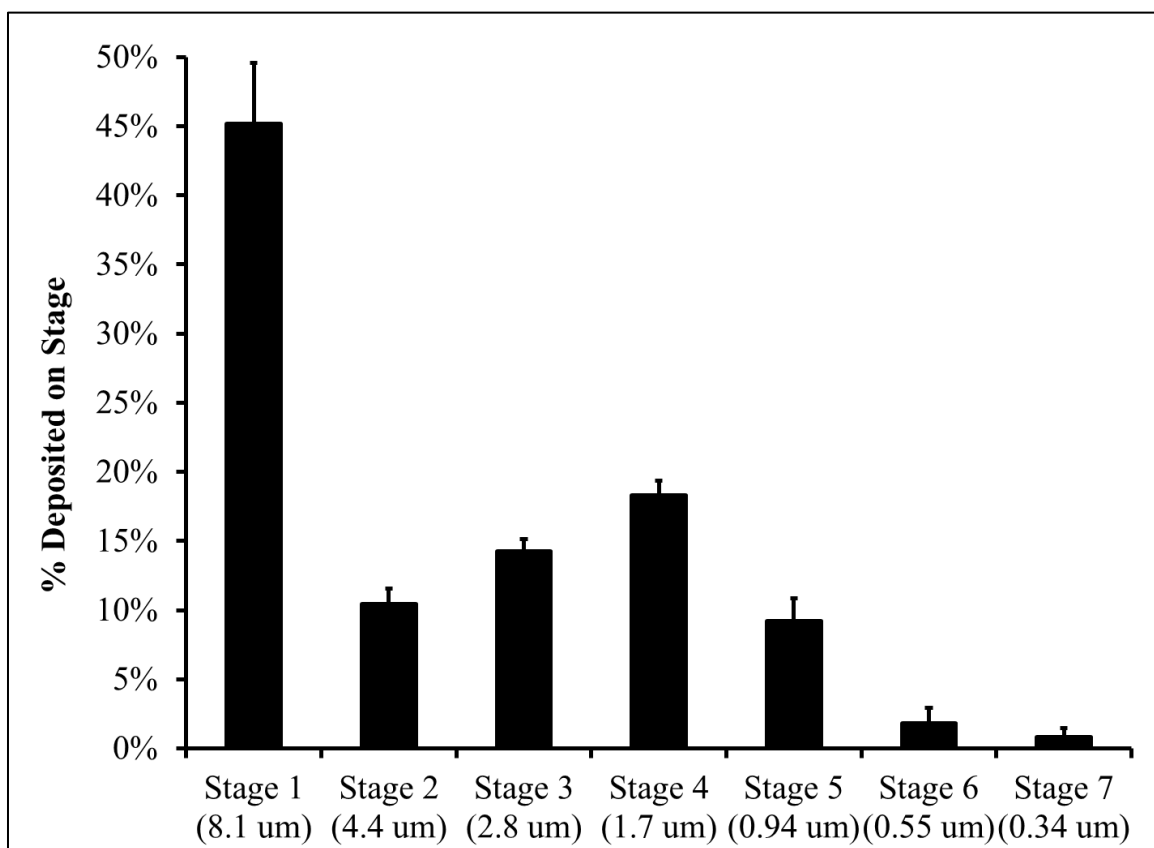


Figure 6.11: Aerosol dispersion performance plot for inhalable responsive HNPs.

Table 6.1: Aerosol performance of HNP composites for inhalation (mean \pm std. dev.).

	MMAD (μm)	GSD (μm)	FPF (%)	RF (%)	ED (%)
HNPs	4.82 ± 0.37	2.51 ± 0.18	31.7 ± 6.8	54.8 ± 4.4	78.5 ± 5.3

The responsiveness of the HNPs released from the composite HNP powders was examined by again measuring their hydrodynamic diameter as a function of pH. Figure 6.12 shows a slight increase in the z-averaged diameter of the HNPs released from the spray dried composites. This increase in z-averaged diameter is accompanied by an increase of the PDI of these particles. For all measurements above the transition pH the PDI varied between 0.1-0.2 indicating a slightly more polydisperse system relative to the HNPs before spray drying. Importantly, the HNPs released from inhalable composites still respond to environmental changes in pH and these responses continue to be reversible. The increase in z-averaged diameter and PDI suggested a population of particles that are in a permanently agglomerated state so we examined their colloidal stability.

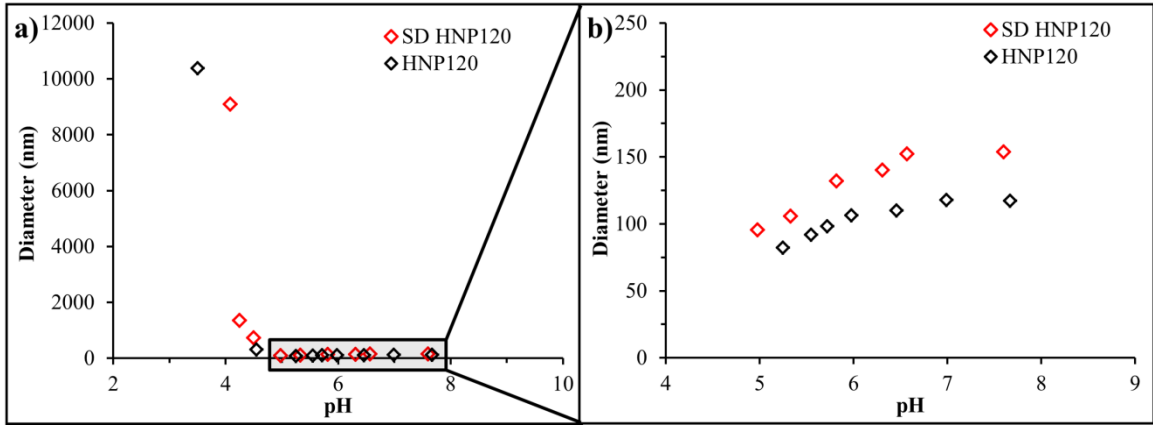


Figure 6.12: Hydrodynamic diameter of HNP120s and SD HNP120s a) over a large range of pH values and b) zoomed above transition pH

Figure 6.13 compares the stability of the HNP120s to those released from the SD HNP120 composites. The HNPs released from the spray dried composites have a subpopulation of particles that fall out of suspension with time. This fraction of particles likely represents permanent agglomerates that were introduced during the spray drying process but only represents approximately 12.6% +/- 0.3% of the HNPs (assuming Beer's law).

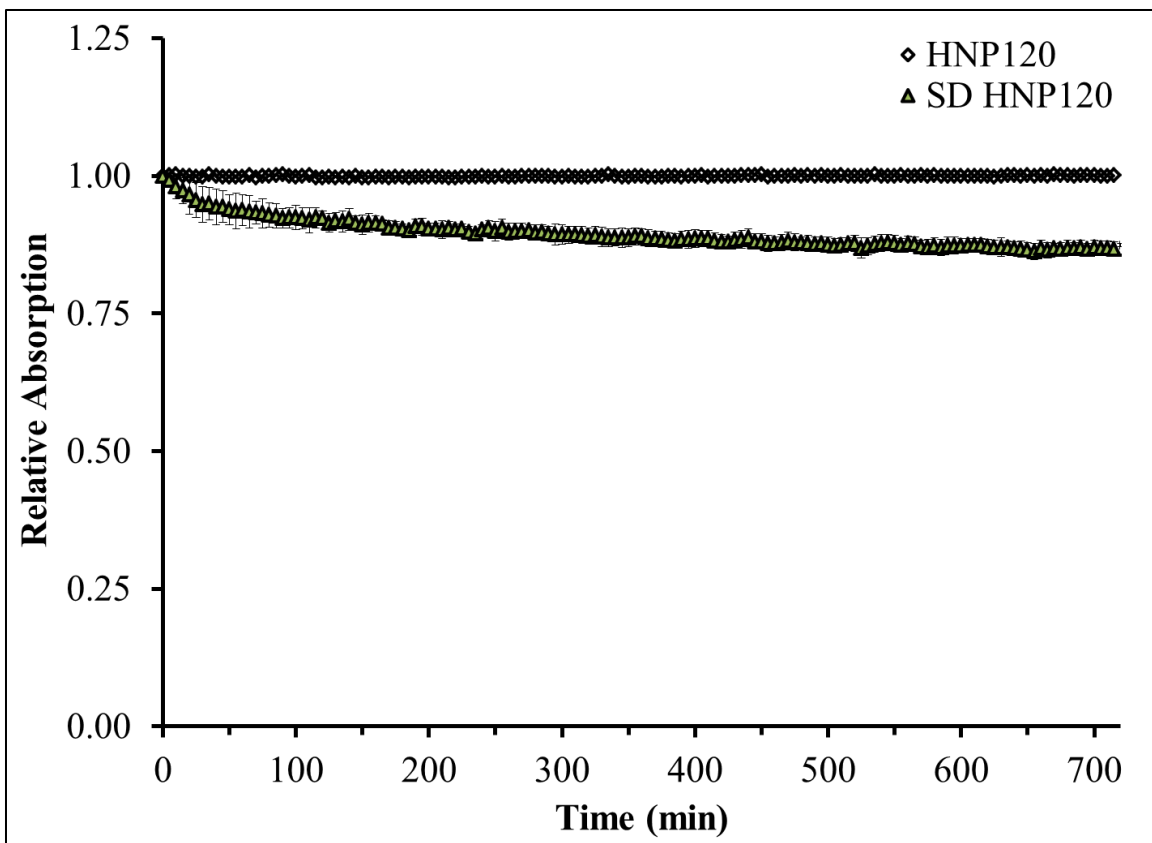


Figure 6.13: Stability of HNP120s and SD HNP120s above transition pH shows population of SD HNP120s that fall out of suspension

To our knowledge, this is the first report of dry powders for inhalation that contain pH-responsive hydrogel nanoparticles. These materials have great potential in diseased states that display local changes in pH such as the reduced pH in the microtumor environment due to increased formative metabolism and poor perfusion (Tannock and Rotin 1989, Estrella, Chen et al. 2013). The evidence of cisplatin loading in these particles and the ability to alter the transition pH indicates the potential to develop intelligent drug delivery vehicles that can be targeted to the lungs via pulmonary delivery of aerodynamically sufficient dry powders.

6.4 Conclusions

Responsive HNPs were successfully synthesized by incorporating MAA as a functional monomer and PEG400DA as a crosslinker. DLS showed a reduction in hydrodynamic diameter of the HNPS due to protonation of the carboxylic acids groups in MAA with decreasing pH. The transition pH of these materials can be altered by changes in the particle synthesis conditions suggesting the ability to tune this value even for a given monomeric system. HNPs were successfully incorporated into inhalable composites and retained their nanometer size as well as their responsive behavior. These findings highlight the great potential for these materials as intelligent drug delivery systems that combine the advantages of nanotechnology, lung targeting through pulmonary delivery, and stimuli-responsive hydrogels.

Acknowledgements

This work would not have been possible without the efforts of Marjorie L. Guy and financial support from the National Institute of Health's National Cancer Institute on grant number R25CA153954.

Chapter 7 Conclusions

Over the last several decades, survival rates of lung cancer patients have shown only minimal improvements. This disease represents an area in oncology where much progress is needed and alternative treatment modalities must be considered. Encouraging progress in personalized therapy is opening doors of opportunity in oncology by discovering genetically targeted moieties for individualized care. Additionally, the modern progress of nanotechnology suggests impending success in cancer applications and the combination with personalized anticancer agents could provide unique therapeutic options. However, new therapies will require innovative drug-delivery platforms in order to maximize their potential therapeutic advantages; pulmonary delivery represents a promising approach for targeting novel cancer therapies and treating primary and secondary lung malignancies.

In this dissertation, pulmonary delivery was investigated as a viable treatment modality for delivering unique nanoparticles and anticancer agents directly to the lungs. We began by examining the possibility of noninvasively administering magnetic nanoparticles to the lungs, via inhalation, for their application as remote-controlled thermal therapy agents. To accomplish this, we successfully formulated dry powder composites consisting of iron oxide MNPs – so-called magnetic nanocomposite microparticles – through advanced spray drying techniques. The physicochemical characterization of these composites revealed their potential and aerosol performance studies demonstrated favorable aerodynamic properties. Heating studies illustrated that

these materials retain excellent remote-heating capability after formulation and *in vitro* cytotoxicity studies showed only moderate toxicity on human lung A549 cells.

To further examine the therapeutic potential of these materials, we utilized an advanced *in vitro* model of metastatic triple negative breast cancer TNBC. This model consisted of spheroids – so called TM analogs – composed of 4T1 breast cancer cells, (ER-, PR-, and HER2-), MEF fibroblast cells, and C166 endothelial cells and represented secondary lung malignancies that could be targeted with inhalable composites. TM analogs were exposed to our MnMs and no measureable adverse effects were observed in the absence of AMF-exposure. Conversely, remote-controlled thermal therapy on TM analogs was accomplished with a custom alternating magnetic field (AMF) and showed a statistically significant increase in cellular death for the higher MNP dose. These findings highlighted the potential of these inhalable MnM composites for future development as a targeted thermal treatment of lung cancer.

The next part of this dissertation examined feasibility of inhalable chemotherapy wherein two anticancer agents (ACAs) commonly administered in the clinic were formulated into dry powder composites for pulmonary delivery. Inhalable powders consisting of cisplatin and erlotinib were successfully formulated by spray drying and their physicochemical properties were evaluated. The aerodynamic diameter of these powders revealed good aerosol performance even in absence of a lactose carrier although the ME10 powder displayed the poorest aerodynamic behavior. Finally, cell studies with human lung cancer cell lines confirmed that the ACAs incorporated into inhalable powders retained their activity upon release into media and confirmed the potential of these systems for future development.

Lastly, we examined responsive hydrogel nanoparticles (HNPs) for their potential in drug delivery as it pertains to pulmonary delivery. The HNPs were synthesized with methacrylic acid and poly(ethylene glycol) as the crosslinker. The carboxylic groups in methacrylic acid provided pH-responsive behavior of these particles wherein their diameter was dependent the protonation of this functional group. Dynamic light scattering showed a reduction in hydrodynamic diameter of the HNPs due to protonation of the carboxylic acids groups in MAA with decreasing pH. Below a certain pH, the particles would aggregate and form large agglomerations due to interparticulate hydrogen bonding. Additionally, this transition pH can be altered by changes in the particle synthesis conditions suggesting the ability to tune this value for a given chemical composition. The HNPs were then successfully incorporated into inhalable composites and retained their nanoscale diameter as well as their responsive behavior. These findings highlight the great potential for these materials as intelligent drug delivery systems that combine the advantages of nanotechnology, lung targeting through pulmonary delivery, and stimuli-responsive hydrogels.

7.1 Significant Findings

This dissertation generated significant results that contribute to the scientific community's understanding of advanced inhalable composites for inhalable lung cancer treatment applications. Although the focus here was on application in lung cancer therapy the fundamental concepts are ubiquitous for diseases involving the lungs. The specific conclusions and relevance of this work is presented below.

- MNPs can be embedded into dry powder composites via spray drying and the resulting powders can be formulated such that good aerodynamic performance is achievable
- The loading of MNPs can be varied in dry powder composites without adversely affecting the aerosol behavior of the materials
- MNPs incorporated to dry-powder composites release upon dissolution and show no signs of agglomeration as evident by consistent hydrodynamic diameter
- Upon release from inhalable composites, MNPs retain their ability to remotely heat in the presence of an alternating magnetic field although this performance is slightly reduced as evident by a small reduction in the SAR value
- Metastatic triple negative breast cancer spheroids (TM analogs) show no signs of mechanical detrition as a result of MNP exposure for 24 hours at MNP concentrations as high as 1.0 mg/mL
- MNPs are presumably non-toxic in TM analogs for concentrations up to 1.0 mg/mL as evidence by no reduction in dead cell count measured through SYTOX[®] Blue staining and fluorescence quantification
- Remote-controlled thermal treatment of TM analogs exposed to MNPs results in mechanical deterioration of the spheroids and results in a statistically significant increase in dead cell count as measured through SYTOX[®] Blue staining and fluorescence quantification

- Cisplatin and erlotinib can be formulated into inhalable dry powder composites with acceptable aerodynamic performance
- These composites show identical cytotoxic profiles in the human lung cancer cell lines H358 and A549 thereby suggesting the released drugs retain their physiological activity
- Hydrogel nanoparticles (HNPs) respond to pH with changes in their hydrodynamic diameter and exhibit a transition pH below which they form large agglomerates, which are presumable due to interparticulate hydrogen bonding
- The incorporation of HNPs into inhalable drug delivery platforms is possible and the release HNPs retain their responsive behavior despite a small increase in their hydrodynamic diameter, which is likely due to an agglomerated subpopulation as suggested by stability studies

Appendix A Transport in PEG-Based Hydrogels: Role of Water Content and Crosslinker Molecular Weight

A.0 ABSTRACT

Polyethylene glycol (PEG) hydrogels are hydrophilic, high water content, polymeric networks that represent excellent candidates as engineering biomaterials for applications ranging from tissue engineering to drug and gene delivery. A key challenge for many biomedical applications is the control of transport properties of small particles within the resulting 3D crosslinked gels. In this work, we investigated the swelling characteristics of a series of PEG-hydrogels as a function of both the water content at synthesis and the molecular weight of the crosslinker used. Using Rhodamine 110 (R110) as a model probe molecule, we examined the transport properties within the resulting PEG-hydrogels by fluorescence correlation spectroscopy (FCS) measurements. We determined a linear relationship between the R110 translational diffusion coefficients, D and the volumetric swelling ratio of the formed hydrogels. Both increasing the water content at synthesis and increasing crosslinker molecular weight are tunable parameters resulting in more open hydrogel microstructures and increased transport of probe molecules through the gel networks.

A.1 INTRODUCTION

Poly(ethylene glycol) (PEG) is one of the most commonly used polymers in biomedicine because of its biocompatibility and has been approved for a wide range of biomedical applications.^[1] Despite a few reports claiming that PEG can result in an

immune response,^[2] most studies have referred to PEG as a stealth polymer due to its ability to avoid eliciting an immune response inside the body.^[3] A wide range of materials utilizing PEG have been extensively studied including PEG coatings on particle systems or devices,^[4, 5] PEG-linked proteins for enhanced performance,^[6, 7] micelle and liposome carriers,^[8, 9] and intelligent hydrogels for drug delivery.^[1, 10, 11]

Hydrogels represent an important and versatile class of biomedical materials proving to be excellent candidates for a wide range of applications ranging from contact lenses to tissue engineering.^[12, 13] Hydrogels consist of three dimensional networks formed by crosslinking hydrophilic polymers and are capable of immobilizing a large amount of water in their interior through capillary forces and surface tension.^[14, 15] Crosslinks in hydrogels can be either physical or chemical in nature, and both have implications on the performance of the material.^[16-18] The amount of water a hydrogel imbibes, among other factors, impacts the microenvironment within the gel. Control of the gel microenvironment directly impacts the suitability of the resulting materials for its intended application.

The microenvironment of a hydrogel is characterized by a variety of parameters. One of the most important parameters is the volume fraction in the swollen state ($v_{2,s}$) or its reciprocal which is the volumetric swelling ratio (Q). These parameters are determined by examining the swelling properties of a given hydrogel system and provide insight into the microenvironment within the hydrogel. A greater swelling capacity implies a less crowded microenvironment. The “crowdedness” of the microenvironment is quantified by another important parameter called the mesh size (ξ), which reports the average distance between polymer chains with a network system. A variety of factors are known

to affect the mesh size of a hydrogel including: composition, charge, molecular weight of the crosslinker, and crosslinking density.^[11] Hydrogels with higher crosslinking density have less capacity to swell due to more tether points that restrict the movement within the gel. These tie points can be covalent bonds, physical entanglements, ionic interactions, or specific affinities between complementary moieties such as ligand-receptor interactions.^[16, 19] Ultimately, the crosslinking of a hydrogel is what determines its three-dimensional structure, and the number and nature of these crosslinks dramatically affects the performance of the hydrogel by altering the mechanical properties, swelling characteristics, and mesh sizes of the network. For applications that require transport of small molecules through the hydrogels, such as drug delivery, dynamics within the hydrogel are highly dependent on the mesh size which controls the mean free path of diffusion.^[20]

Fluorescence correlation spectroscopy (FCS) has been previously shown effective to measure transport properties of small molecules in various polymeric systems.^[21-24] This includes the use of FCS to examine the diffusion of probe molecules in hydrogels.^[17, 25-29] It has been shown that higher molar ratios of chemical crosslinkers lead to slower diffusion of probe molecules.^[30] Less studied are the effects of water content during hydrogel synthesis and the molecular weight of the crosslinker on the transport properties of probe molecules.

In this work, we examined the role of final water content and crosslinker molecular weight on both the swelling characteristics and the resulting diffusivity of probe molecules within the PEG-hydrogels. An array of PEG-based hydrogels was synthesized with varied solvent content during synthesis as well as varying the molecular

weight of the crosslinker. The two crosslinkers used in this study, poly(ethylene glycol) 400 diacrylate (PEG400DA) and poly(ethylene glycol) 4000 diacrylate (PEG4000DA), are identical in chemical composition but differ by an order of magnitude in the average molecular weight of the ethylene glycol chain. To examine nanoparticle transport properties within the hydrogels, gels were washed, lyophilized, and subsequently imbibed with a model fluorescent probe, rhodamine 110 (R110), at nanomolar concentrations. We used FCS to measure the translational diffusion coefficient of R110 in the resulting PEG-hydrogels. Additionally, the swelling characteristics of these gels were measured, and the correlation between swelling and diffusion was examined (Figure A.1). We show that increasing the solvent content during hydrogel synthesis leads to a microenvironment consisting of fewer physical crosslinks and, therefore, less crowded hydrogels. Additionally, we demonstrate that changing the molecular weight of the crosslinker has a dramatic effect on the transport of probe molecules within the hydrogel due to increased mesh sizes. Lastly, we determined an approximately linear relationship between the translational diffusion coefficient, D , of a probe molecule and the volumetric swelling ratio of the formed hydrogels.

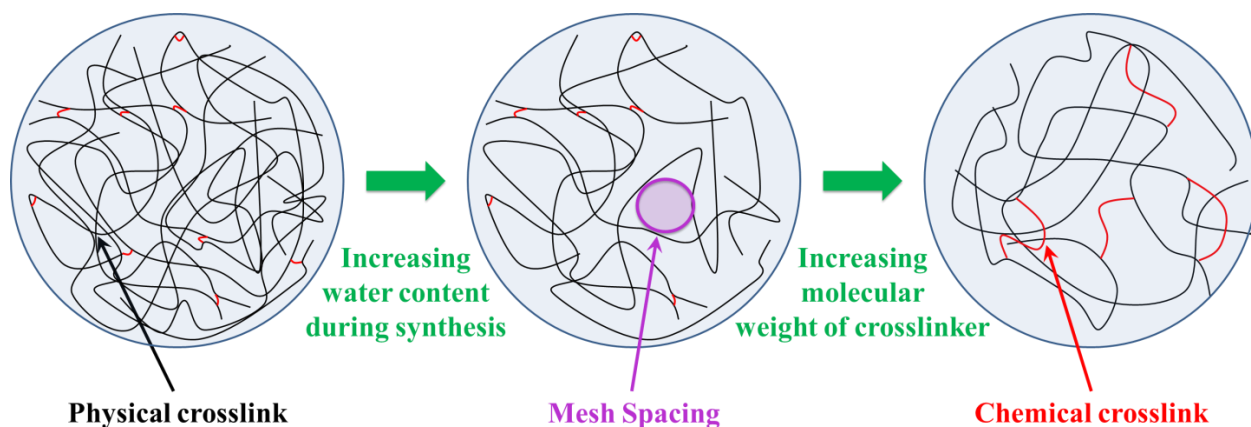


Figure A.1: Schematic representation of changes in hydrogel network properties due to changes in solvent content and molecular weight of crosslinker.

A.2 Material and methods

A.2.1 Materials

PEG200 monomethyl ether monomethacrylate (PEG200MMA), PEG400 diacrylate (PEG400DA), and PEG4000 diacrylate (PEG4000DA) were purchased from Polysciences, Inc. (Warrington, PA. USA). Irgacure 2959 (I-2959) was purchased from BASF (Ludwigshfen, Germany). Rhodamine 110 (R110) and Thermo Scientific Nunc Lab-Tek chambered coverglass 8-well chambers were purchased from Fisher Scientific (Pittsburgh, PA).

A.2.2 Synthesis of hydrogels through UV polymerization

Hydrogels were synthesized at room temperature through UV polymerization using methods similar to those previously reported.(Meenach, Anderson et al. 2009, Yakacki, Satarkar et al. 2009, Yu, Luo et al. 2010, Hawkins, Puleo et al. 2011, Hawkins,

Tolbert et al. 2013) Briefly, acrylated PEG moieties were weighed out and mixed with the water-soluble photoinitiator I-2959 (1 wt%). The water content during synthesis was varied between 0-85 wt% based on the total mass of the system. This mixture was pipetted between two glass plates containing a 1mm Teflon® spacer and held together with binder clips. The plate was then exposed to 365 nm UV light for five minutes using a Lesco Cure Max UV flood source (American ultraviolet, Torranc, CA) operating at ~10-11 mW/cm². After polymerization, gels were punched into 4mm discs and washed in DI water for 1 week. For measurement of probe diffusion by fluorescence correlation spectroscopy (FCS), hydrogels were washed in DI water for 1 week then imbibed overnight with R110 at a concentration of 10 nM. Gels were subsequently removed and placed into NUNC LabTek 8-well microscopy chambers (Nalgene Nunc International) and measured directly by FCS.

A.2.3 Conversion of hydrogels through Fourier Transform Infrared Spectroscopy (FTIR) analysis

In order to determine the conversion of the hydrogel systems, an attenuated total refractive FTIR (ATR-FTIR) was used to ratio the intensity of the carbon-carbon double bond at ~1647 cm⁻¹ relative to the carbon-oxygen double bond in the carbonyl group (~1725 cm⁻¹), which should remain constant. A small amount of the prepolymerized mixture was placed on the liquid sample holder and a kinetic measurement was made while the gel was polymerized on the FTIR stage using an EXFO OmniCure™ Series 2000 Spot Curing System (Lumen Dynamics Group, Mississauga, ON, Canada).

A.2.4 Swelling studies

Discs cut from hydrogels were allowed to soak in DI water for 1 week. During this time, the water was exchanged periodically to ensure an adequate sink. After 1 week, gels appeared to have swollen to their equilibrium state and were subsequently weighed in air and in heptane using a Mettler Toledo Density Accessory Kit (Mettler Toledo, Columbus, OH). After being weighed, the gels were placed in a freezer overnight at -20°C. Once frozen, the gels were lyophilized by transferring them to a FreeZone Plus (Labconco, Kansas City, MO) for 24 hours. Once dried, the gels were weighed in air and water again and the volumetric swelling ratio, Q , was calculated through the following equation:

$$Q = \frac{m_{s,a} - m_{s,h}}{m_{d,a} - m_{d,h}} \quad (\text{Equation A.1})$$

where $m_{s,a}$, $m_{s,h}$, $m_{d,a}$, and $m_{d,h}$ represent the mass of a given disc swollen in air, swollen in heptane, dry in air and dry in heptane, respectively.

A.2.5 FCS setup

Fluorescence correlation spectroscopy (FCS) experiments are made using the ISS Alba confocal fluorescence fluctuation system coupled to a Nikon Ti-U microscope equipped with a 60x/1.2 NA water immersion objective lens. The illumination source is a continuous wave 488 nm laser diode passed through a 514 nm long pass edge filter before detection. Emission signal was recorded by photomultiplier tubes (PMTs) in each channel. All FCS measurements were performed in NUNC LabTek 8-well microscopy chambers (Nalgene Nunc International) with a final volume of ~500 μ L. Determination

of the focal volume was established via calibration against an aqueous solution of Rhodamine 110 with known diffusion coefficient ($D = 440 \mu\text{m}^2 \text{s}^{-1}$). (Gendron, Avaltroni et al. 2008) Diffusion coefficients reported are calculated from an average of at least 10 FCS measurements, taken at various positions within the hydrogel, performed at room temperature on a sample. Typical sampling times of ~30 seconds were used. All results are expressed as mean values +/- the standard deviation of the recorded diffusion coefficient. All FCS measurements were analyzed using VistaVision 4.0 Software.

A.2.6 FCS Data Analysis

As the basic principles of FCS have been described elsewhere, (Elson and Magde 1974, Hess, Huang et al. 2002) here we will give only a brief overview. FCS measures the fluorescence fluctuations emitted from labelled molecules moving in and out of a small confocal volume (~1 fL). The size of the effective illumination volume is fixed by the confocal detection optics and the excitation profile of the focused laser beam and characterized by measurements against a standard of a known diffusion constant. As labeled particles diffuse through the detection volume, a signal $I(t)$ is generated with fluctuations around a mean value. The average intensity fluctuation is $\langle I(t) \rangle = I(t) - \delta I(t)$ where $\delta I(t)$ donates the spontaneous deviation of the measured intensity around the average intensity. For monodisperse particles diffusing by ideal Brownian motion, dynamic information can be determined from the intensity fluctuations by means of a time autocorrelation given by

$$G(\tau) = 1 + \frac{1}{N} \cdot \left(\frac{1}{1 + \frac{\tau}{\tau_D}} \right) \cdot \frac{1}{\sqrt{1 + \frac{r_0^2}{z_0^2} \cdot \frac{\tau}{\tau_D}}} \quad (\text{Equation A. 2})$$

Here, N is the average number of particles in the illumination volume. The structure parameters r_0 and z_0 are the axial and radial dimensions of excitation beam respectively and are determined by calibration measurements. Experimental autocorrelations are fitted to equation 2 with τ_D and N as fitting parameters. The autocorrelation can be normalized by

$$G_{Norm}(\tau) = \frac{G(\tau) - 1}{G(0) - 1} \quad (\text{Equation A. 3})$$

The characteristic diffusion time τ_D is related to the translational diffusion coefficient D by the simple relationship

$$\tau_D = \frac{r_0^2}{4D} \quad (\text{Equation A. 4})$$

where D denotes the translational diffusion coefficient of the molecule and is calculated from the lateral width of the focused incident beam and the experimentally determined τ_D .

A.3 Results and Discussion

A.3.1. Hydrogel synthesis

Three different hydrogel systems were used, and the water content during synthesis was varied for each system. Table A.1 summarizes the hydrogel systems that were synthesized. All but two hydrogel systems were successfully synthesized with UV polymerization. The P400-95/5 with 85 wt% water and the P4000-100

with 70 wt% water never formed mechanically stable gels resulting in discs that fell apart upon handling. Fragments of the P4000-100 gel with 70% water gel were still suitable for FCS measurements as small sample size could be utilized in these studies.

Table A.1: Summary of hydrogel systems synthesized

System ID	PEG200MMA (mol%)	PEG400DA (mol%)	PEG4000DA (mol%)	Water (wt%)
P400-100	-	100	-	0,15,30,50,70,85
P400-50/50	50	50	-	0,15,30,50,70,85
P400-95/5	95	5	-	0,15,30,50,70,85*
P4000-100	-	-	100	50,70
P4000-50/50	50	-	50	50,70
P4000-95/5	95	-	5	50,70*

*Denotes gels that did not form

The lack of mechanical stability indicates that both the molecular weight of the crosslinker and the water content during synthesis have a large effect on microenvironment of the resulting PEG-based hydrogels. FTIR analysis was used to examine the percent conversion of the hydrogel formulations by observing the disappearance of the carbon-carbon double bond at $\sim 1630\text{cm}^{-1}$ (Figure A.2). Normalizing this peak to the carbonyl peak ($\sim 1710\text{cm}^{-1}$) allows us to quantify conversion of greater than 90% for the P400 gels, and these data confirm that differences in gel properties are a result of changes in microenvironments as opposed to low

conversion due to dilute conditions. Due to lack of material, the conversion for the P4000 gels was not measured.

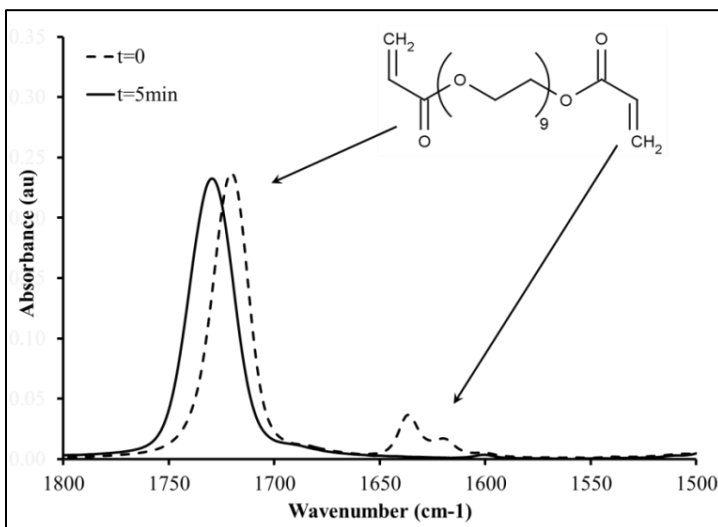


Figure A.2: Representative FTIR spectra of a P400 gel before ($t=0$) and after ($t=5\text{min}$) UV irradiation.

A.3.2 Swelling studies

Figure A.3 shows the equilibrium volumetric swelling ratio, Q , for P400-100, P400-50/50, and P400-95/5 gels plotted as a function of water content during synthesis. The resulting hydrogels all show an increase in Q with increasing water content during synthesis. For all three P400 systems, the increase in Q with water content was greater than 2-fold showing relatively large change in swelling by changing synthesis conditions for the shorter MW PEG crosslinker.

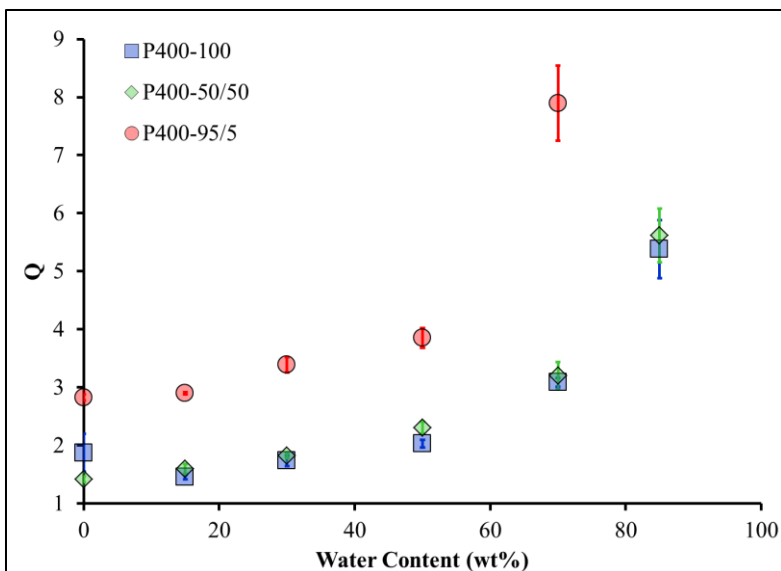


Figure A.3: Equilibrium volumetric swelling ratio, Q , as a function of water content during synthesis for P400-100 (blue squares), P400-50/50 (Green diamonds), and P400-95/5 (red circles) gels.

This increase in swelling ratio is most likely due to a microenvironment containing fewer restrictions in the form of entangled polymer chains (i.e. fewer physical crosslinks). By synthesizing in more dilute conditions, entanglement is less likely, and therefore, the gel swells to a greater extent. Interestingly, P400-100 and P400-50/50 gels showed no difference in their swelling properties for the same water content indicating there may exist a critical crosslinking density above which the swelling is controlled predominately by physical crosslinks. Although it is widely known that increasing the crosslinking density reduces swelling, our data suggests that, for these PEG-hydrogels, there is a threshold above which the crosslinking density has no effect on the equilibrium swelling characteristics of the gels.

We also examined the extent of post-synthesis swelling by plotting the water content (wt%) of the swollen gel as a function of the water content during synthesis as shown in Figure A.4. The line $y = x$ serves as a reference for how much the gels were able to swell after synthesis where no deviation from this line indicates the gel did not swell beyond their relaxed state as synthesized. Dilute systems containing hydrogels with high crosslinking densities were synthesized in their swollen state as the water content during synthesis was equal to that at equilibrium after 1 week of swelling.

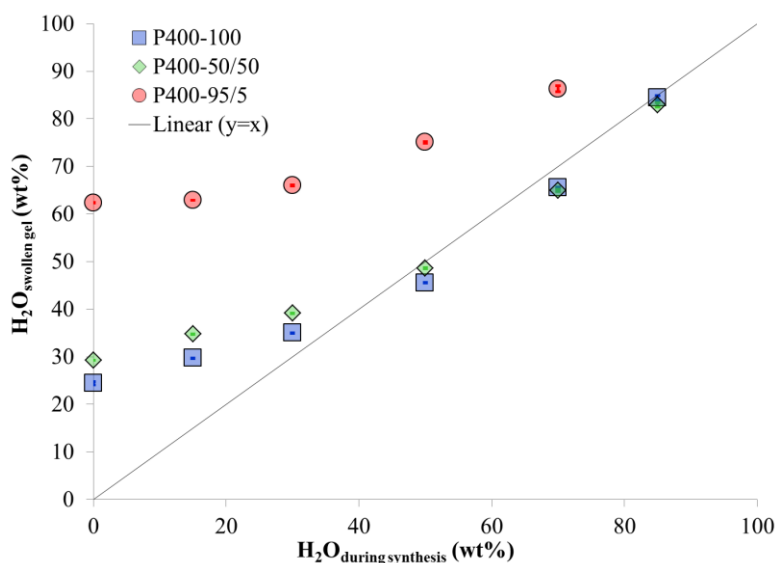


Figure A.4: Water content (wt%) of the swollen gel ($H_2O_{\text{swollen gel}}$) as a function of the water content during synthesis ($H_2O_{\text{during synthesis}}$).

Next, we examined the effects of changing the molecular weight of the crosslinker on the swelling properties of these PEG-based hydrogels. Representative images of two hydrogel discs synthesized at the same water content (50 wt%) with pure crosslinker of different molecular weights are shown in Figure A.5. P400 and

P4000 represent the molecular weight of the PEG crosslinker molecule as 400 and 4000 kDa, respectively. Both discs were cut at 4mm directly after synthesis and allowed to swell to equilibrium for 1 week. There are clear differences in the swelling capacity for these two systems demonstrating a strong dependence of the swelling with the molecular weight of the crosslinker. P4000 hydrogel was able to swell to a much larger size than the P400 at the same 50% water content. The volumetric swelling ratio for a variety of P400 and P4000 gels with both 50% and 70% water content, are shown in Figure A.6. At a given water content, we observe greater swelling for all P4000 gel formulations indicating that both the molecular weight of the crosslinker and the water content during synthesis play a key role in the swelling properties of these PEG-hydrogels..

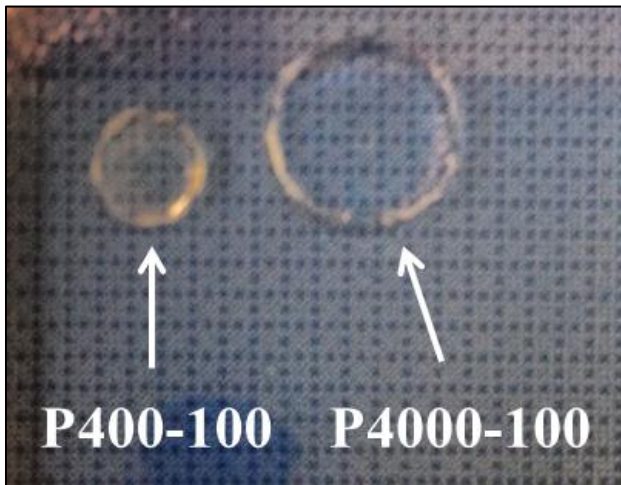


Figure A.5: Picture of P400-100 (left) and P4000-100 (right) gels synthesized with 50 wt% water. These gels were cut to 4mm discs after synthesis then allowed to swell to equilibrium for 1 week and photographed.

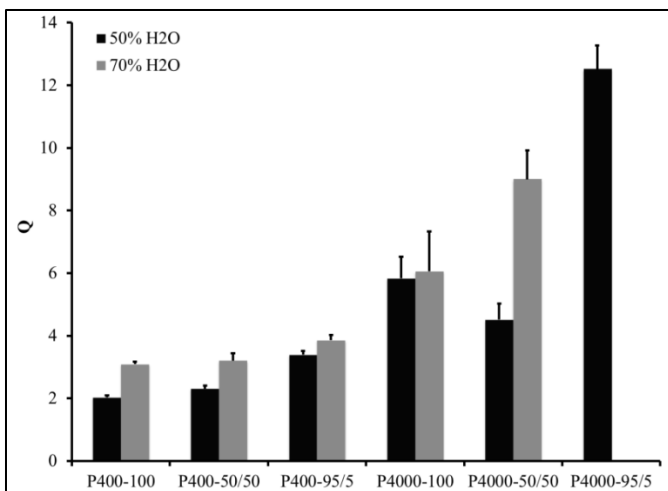


Figure A.6. Volumetric swelling ratios for the P4000 gels and P400 gels with varying water content during synthesis.

A.3.2 Probe diffusion in PEG hydrogels

Prior to FCS measurements, DI washed hydrogels were imbibed overnight with rhodamine 110 (R110) at a concentration of 10 nM to ensure equilibrated distribution of the probe molecule throughout the gel. Measurements were performed at various spots in the hydrogel and averaged to obtain average translation diffusion coefficients D of R110 within the synthesized hydrogels. Normalized autocorrelation functions for R110 diffusing in hydrogels are shown in Figure A.7 with different amounts of PEG400 and PEG4000 crosslinkers. Three different sets of representative experiments are shown. Figure A.7A shows R110 diffusion in PEG400 hydrogels with varying amounts of the PEG200MMA.

All autocorrelation functions can be well described by a single mean passage time as given in Equation 2 and 3. Our results suggest similar characteristic diffusion times τ_D for R110 with P400-100 and P400-50/50 hydrogels, but a significant shift to shorter τ_D ,

in the P400-95/5 hydrogels where only 5% of the gel composition included the difunctional PEG400 crosslinker resulting in gels with significantly lower crosslink density. Decreasing \square_D is equivalent to increasing translational diffusion coefficients D as determined from equation 4. Our results reveal the low crosslink density allows for faster diffusion of R110 probe molecules in the PEG hydrogels.

Figure A.7B shows normalized autocorrelation functions for both P400-100 and P4000-100 hydrogels formed at 50 and 70 wt% water content during synthesis. The increased water content at synthesis also results in hydrogels with decreased crosslink density as evidenced by the decreased characteristic times of R110 at 70% water content as compared to 50% in both PEG hydrogel systems. In addition, in Figure A.7B, you can see that the larger P4000 crosslinker (triangles/diamonds) resulted in significantly smaller diffusion times for R110 compared to hydrogels synthesized at the same water content with the shorter P400 crosslinker (circles/squares). Figure A.7C shows the normalized autocorrelation functions measured by FCS for P400-100 hydrogels continues to shift to shorter \square_D as the water content at synthesis is increased further. These results are also consistent with a more open microenvironment within the PEG400-100 hydrogels within increased water content at synthesis allowing for faster particle transport through the polymeric network.

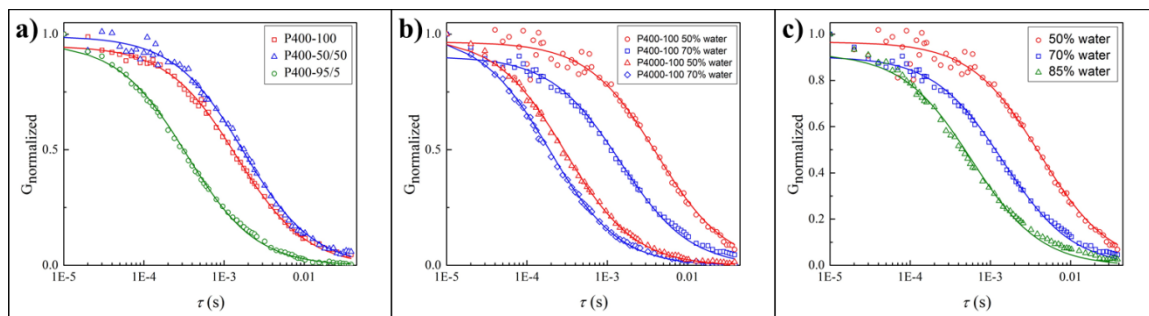


Figure A.7. Normalized FCS autocorrelation curves of (a) P400 gels with 50% water content and varying crosslinking density, (b) P400-100 and P4000-100 gels with varying water content at synthesis, and (c) P400-100 gels with 50, 70%, and 85% water content at synthesis.

Figure A.8 shows the translational diffusion coefficients calculated from equation 4 for P400 hydrogels as a function of the water content during synthesis. Three P400 systems are plotted with varying amounts of the monofunctional PEG200-MMA. Larger translational diffusion coefficients are observed for all three systems with increasing water content, where we anticipate fewer crosslinks being formed. At low water content, hydrogels with high crosslink densities are synthesized and rhodamine diffusion is significantly slowed in these systems.

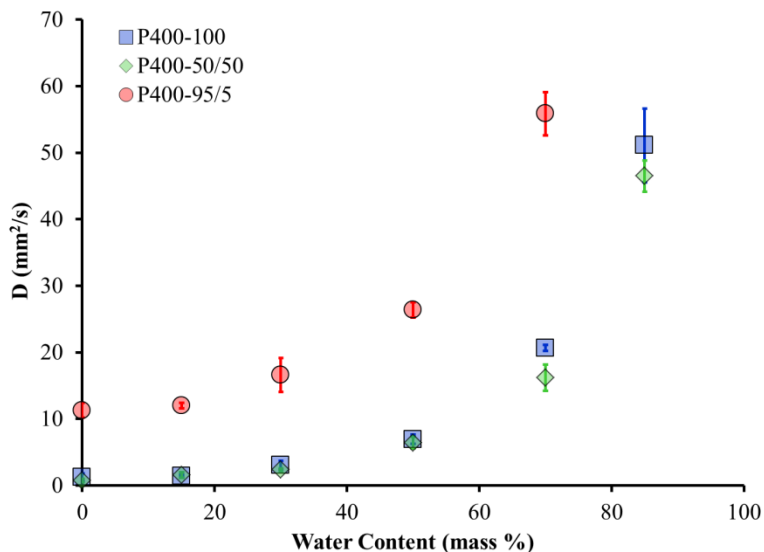


Figure A.8. Diffusion coefficient of R110 as a function of the water content during synthesis for gels containing PEG400DA.

Hydrogels composed of pure crosslinker and 50% crosslinker are observed to have very similar transport properties of R110. These trends closely resemble the observed trends for Q as a function of water content shown in Figure A.3. Only the P400-95/5 gels, with 95% monofunctional PEG200MMA incorporated into the hydrogel, shows significantly increased diffusion coefficients for the R110 probe molecules. Hence, we also examined the relationship between the diffusion coefficient of R110 and the swelling behaviour of our P400 hydrogels and saw an approximately linear relationship between these variables (Figure A.9). The r-squared value for each of these systems was >0.97 indicating a linear trend is appropriate for these data. Our results suggest that for these PEG-hydrogel systems, the swelling properties have a direct relationship to the crosslinker species within the hydrogel.

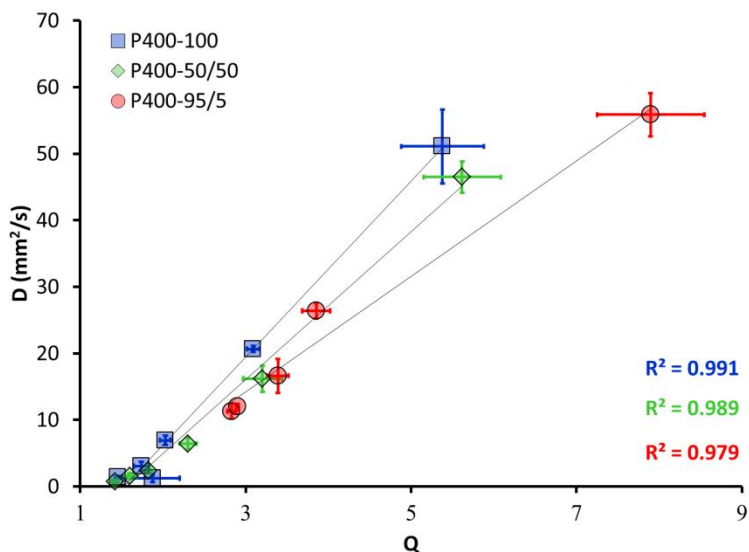


Figure A.9. Linear relationship between the diffusion coefficient, D , of R110 and the swelling ratio, Q , where a given point has the same water content during synthesis.

Lastly, the translational diffusion coefficients of R110 in various P400 and P4000 gels at 50% and 70% water content at synthesis were determined and are plotted in Figure A.10. These data illustrate that probe molecule transport in P4000 has a dramatically larger diffusion coefficient when compared to the corresponding P400 gel due presumably to larger gel correlation lengths formed when using the longer PEG crosslinker. As with P400 gels, R110 displayed almost identical translational diffusion coefficients in the P4000-100 and P4000-50/50 gels suggesting that there may exist a critical crosslinking density above which physical crosslinks dominate the effects of the microenvironment on the transport of small molecules. Interestingly, comparing the P400 and P4000 gels with high crosslinking density (50 or 100%) we see that the ratio of molecular weight between the crosslinkers (MWPEG400DA:MWPEG4000DA), 10.0, was almost the same as the ratio of diffusion coefficients (DPEG400DA: DPEG4000DA), which was 11.2 ± 2.4 and 9.7 ± 0.7 for the systems with 50 and 100% crosslinking density, respectively. To our knowledge, this is the first report of FCS being used to directly correlate the diffusion coefficient of a molecular probe with the molecular weight of a crosslinker. Control of the properties of synthesized hydrogels is critical to the engineering of these biocompatible materials for various applications. Taken together, our results suggest controlling the swelling ratio through molecular weight of the crosslinks or varying water content at synthesis are viable means to

vary the transport properties of molecules within PEG-hydrogels.

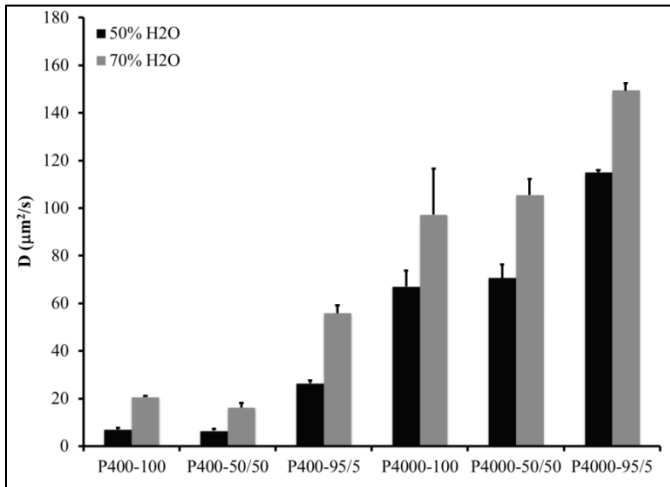


Figure A.10. Diffusion coefficients for the P4000 gels and P400 gels with varying water content during synthesis.

A.4 Conclusions

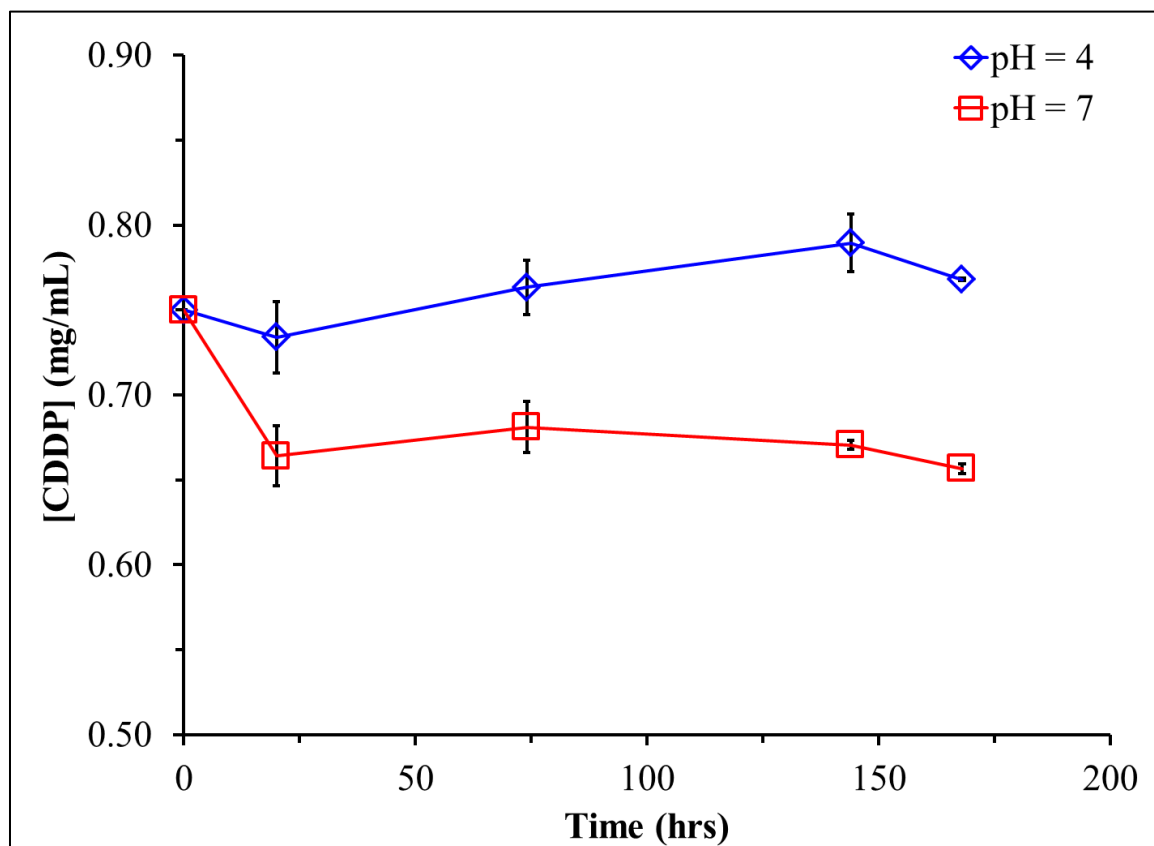
We successfully synthesized an array of PEG-based hydrogels in order to study the effects of water content and crosslinker molecular weight on transport properties of a model probe molecule. The swelling properties of these gels showed that, as predicted, more dilute synthesis conditions lead to hydrogels with a greater swelling capacity. This larger swelling capacity indicates less restriction within the synthesized hydrogels, which we attribute to a lower number of physical crosslinks formed. Using FCS, we determined the translational diffusion coefficient of a probe molecule (rhodamine 110, R110) inside the synthesized hydrogels and determined a linear relationship with the volumetric swelling ratio of the gels. The effect of changing the molecular weight of the crosslinker molecule used in synthesis was also examined on both the swelling characteristics

of the gel and transport of R110 inside the formed hydrogels. For all cases, P4000 hydrogels displayed greater swelling capacity and increased transport properties of R110 as compared to the corresponding P400 gels. These results illustrate that the water content during synthesis and the molecular weight of the crosslinker have a dramatic impact on the microenvironment of these hydrogels and have significant implications for engineering tunable hydrogels for specific biomedical applications.

Acknowledgements:

NAS acknowledges the financial support from a NCI-CNTC pre-doctoral traineeship and XZ acknowledge financial support from the University of Kentucky Research Challenge Trust Fund (RCTF) Fellowship for Biochemistry. The project described was supported by Grant Number 5R25CA153954 from the National Cancer Institute and start-up funds from the University of Kentucky.

Appendix B Supplemental Figures



Supplemental Figure B.1: Loading of cisplatin in HNPs at pH of 7 and 4

References

(1984). "ANALYTICAL PROFILES OF DRUG SUBSTANCES - FOLEY,K." Journal of the American Chemical Society **106**(4): 1173-1173.

(2006). <601> Aerosols, Nasal Sprays, Metered-Dose Inhalers, and Dry Powder Inhalers Monograph. USP 29-NF 24 The United States Pharmacopoeia and The National Formulary: The Official Compendia of Standards. Rockville, MD, The United States Pharmacopeial Convention, Inc. **29/24**: 2617-2636.

(!!! INVALID CITATION !!!).

Ally, J., A. Amirfazli and W. Roa (2006). "Factors affecting magnetic retention of particles in the upper airways: An in vitro and ex vivo study." Journal of Aerosol Medicine-Deposition Clearance and Effects in the Lung **19**(4): 491-509.

Ally, J., B. Martin, M. B. Khamesee, W. Roa and A. Amirfazli (2005). "Magnetic targeting of aerosol particles for cancer therapy." Journal of Magnetism and Magnetic Materials **293**(1): 442-449.

Andre, F. and C. C. Zielinski (2012). "Optimal strategies for the treatment of metastatic triple-negative breast cancer with currently approved agents." Annals of Oncology **23**: 46-51.

Anselmo, A. C. and S. Mitragotri (2014). "An overview of clinical and commercial impact of drug delivery systems." Journal of Controlled Release **190**: 15-28.

Anthony J., H. and H. M. Mansour (2009). Delivery of Drugs by the Pulmonary Route. Modern Pharmaceutics Volume 2: Applications and Advances. A. Florence and J. Siepmann. New York, Taylor & Francis. **2**: 191-219.

Arenberg, D. (2011). "Bronchioloalveolar Carcinoma." Seminars in Respiratory and Critical Care Medicine **32**(1): 52-61.

Azarmi, S., W. H. Roa and R. Loebenberg (2008). "Targeted delivery of nanoparticles for the treatment of lung diseases." Advanced Drug Delivery Reviews **60**(8): 863-875.

Azarmi, S., X. Tao, H. Chen, Z. L. Wang, W. H. Finlay, R. Lobenberg and W. H. Roa (2006). "Formulation and cytotoxicity of doxorubicin nanoparticles carried by dry powder aerosol particles." International Journal of Pharmaceutics **319**(1-2): 155-161.

Babincova, M., V. Altanero, C. Altaner, C. Bergemann and P. Babinec (2008). "In vitro analysis of cisplatin functionalized magnetic nanoparticles in combined cancer chemotherapy and electromagnetic hyperthermia." Ieee Transactions on Nanobioscience **7**(1): 15-19.

Baeza, A., M. Colilla and M. Vallet-Regi (2015). "Advances in mesoporous silica nanoparticles for targeted stimuli-responsive drug delivery." Expert Opinion on Drug Delivery **12**(2): 319-337.

Bates, R. C., N. S. Edwards and J. D. Yates (2000). "Spheroids and cell survival." Critical Reviews in Oncology Hematology **36**(2-3): 61-74.

Bonomi, M., S. Pilotto, M. Milella, F. Massari, S. Cingarlini, M. Brunelli, M. Chilosi, G. Tortora and E. Bria (2011). "Adjuvant chemotherapy for resected non-small-cell lung cancer: future perspectives for clinical research." Journal of Experimental & Clinical Cancer Research **30**.

Brannon-Peppas, L. and J. O. Blanchette (2004). "Nanoparticle and targeted systems for cancer therapy." Advanced Drug Delivery Reviews **56**(11): 1649-1659.

Burger, A., J. O. Henck, S. Hetz, J. M. Rollinger, A. A. Weissnicht and H. Stottner (2000). "Energy/temperature diagram and compression behavior of the polymorphs of D-mannitol." Journal of Pharmaceutical Sciences **89**(4): 457-468.

Carpenter, J. F., M. J. Pikal, B. S. Chang and T. W. Randolph (1997). "Rational design of stable lyophilized protein formulations: Some practical advice." Pharmaceutical Research **14**(8): 969-975.

Carvalho, T. C., S. R. Carvalho and J. T. McConville (2011). "Formulations for Pulmonary Administration of Anticancer Agents to Treat Lung Malignancies." Journal of Aerosol Medicine and Pulmonary Drug Delivery **24**(2): 61-80.

Chen, M. C., K. Sonaje, K. J. Chen and H. W. Sung (2011). "A review of the prospects for polymeric nanoparticle platforms in oral insulin delivery." Biomaterials **32**(36): 9826-9838.

Cho, K. J., X. Wang, S. M. Nie, Z. Chen and D. M. Shin (2008). "Therapeutic nanoparticles for drug delivery in cancer." Clinical Cancer Research **14**(5): 1310-1316.

Cho, W. S., M. J. Cho, S. R. Kim, M. Choi, J. Y. Lee, B. S. Han, S. N. Park, M. K. Yu, S. Jon and J. Jeong (2009). "Pulmonary toxicity and kinetic study of Cy5.5-conjugated superparamagnetic iron oxide nanoparticles by optical imaging." Toxicology and Applied Pharmacology **239**(1): 106-115.

Choi, S. J., J. M. Oh and J. H. Choy (2009). "Toxicological effects of inorganic nanoparticles on human lung cancer A549 cells." Journal of Inorganic Biochemistry **103**(3): 463-471.

Chou, A. J., M. D. Bell, C. Mackinson, R. Gupta, P. A. Meyers and R. Gorlick (2007). Phase Ib/IIa study of sustained release lipid inhalation targeting cisplatin by inhalation in the treatment of patients with relapsed/progressive osteosarcoma metastatic to the lung. Journal of Clinical Oncology, American Society of Clinical Oncology. **25**: 9525.

- Chow, A. H. L., H. H. Y. Tong, P. Chattopadhyay and B. Y. Shekunov (2007). "Particle engineering for pulmonary drug delivery." Pharmaceutical Research **24**(3): 411-437.
- Colombo, M., S. Carregal-Romero, M. F. Casula, L. Gutierrez, M. P. Morales, I. B. Bohm, J. T. Heverhagen, D. Prospero and W. J. Parak (2012). "Biological applications of magnetic nanoparticles." Chemical Society Reviews **41**(11): 4306-4334.
- Cone, R. A. (2009). "Barrier properties of mucus." Advanced Drug Delivery Reviews **61**(2): 75-85.
- Coto-Garcia, A. M., E. Sotelo-Gonzalez, M. Fernandez-Arguelles, R. Pereiro, J. M. Costa-Fernandez and A. Sanz-Medel (2011). "Nanoparticles as fluorescent labels for optical imaging and sensing in genomics and proteomics." Analytical and Bioanalytical Chemistry **399**(1): 29-42.
- Courrier, H. M., N. Butz and T. F. Vandamme (2002). "Pulmonary drug delivery systems: Recent developments and prospects." Critical Reviews in Therapeutic Drug Carrier Systems **19**(4-5): 425-498.
- Crino, L., W. Weder, J. van Meerbeek, E. Felip and E. G. W. Grp (2010). "Early stage and locally advanced (non-metastatic) non-small-cell lung cancer: ESMO Clinical Practice Guidelines for diagnosis, treatment and follow-up." Annals of Oncology **21**: v103-v115.
- Dames, P., B. Gleich, A. Flemmer, K. Hajek, N. Seidl, F. Wiekhorst, D. Eberbeck, I. Bittmann, C. Bergemann, T. Weyh, L. Trahms, J. Rosenecker and C. Rudolph (2007). "Targeted delivery of magnetic aerosol droplets to the lung." Nature Nanotechnology **2**(8): 495-499.
- Daniher, D. I. and J. Zhu (2008). "Dry powder platform for pulmonary drug delivery." Particuology **6**(4): 225-238.
- De, S. K., N. R. Aluru, B. Johnson, W. C. Crone, D. J. Beebe and J. Moore (2002). "Equilibrium swelling and kinetics of pH-responsive hydrogels: Models, experiments, and simulations." Journal of Microelectromechanical Systems **11**(5): 544-555.
- DeSantis, C., J. M. Ma, L. Bryan and A. Jemal (2014). "Breast Cancer Statistics, 2013." Ca-a Cancer Journal for Clinicians **64**(1): 52-62.
- Dobson, J. (2006). "Magnetic micro- and nano-particle-based targeting for drug and gene delivery." Nanomedicine **1**(1): 31-37.
- Dolovich, M. B., R. C. Ahrens, D. R. Hess, P. Anderson, R. Dhand, J. L. Rau, G. C. Smaldone and G. Guyatt (2005). "Device selection and outcomes of aerosol therapy: Evidence-based guidelines." Chest **127**(1): 335-371.

- Driscoll, C. F., R. M. Morris, A. E. Senyei, K. J. Widder and G. S. Heller (1984). "MAGNETIC TARGETING OF MICROSPHERES IN BLOOD-FLOW." Microvascular Research **27**(3): 353-369.
- Du, J., I. M. El-Sherbiny and H. D. Smyth (2014). "Swellable Ciprofloxacin-Loaded Nano-in-Micro Hydrogel Particles for Local Lung Drug Delivery." Aaps Pharmscitech **15**(6): 1535-1544.
- Eberhard, D. A., B. E. Johnson, L. C. Amler, A. D. Goddard, S. L. Heldens, R. S. Herbst, W. L. Ince, P. A. Janne, T. Januario, D. H. Johnson, P. Klein, V. A. Miller, M. A. Ostland, D. A. Ramies, D. Sebisanovic, J. A. Stinson, Y. R. Zhang, S. Seshagiri and K. J. Hillan (2005). "Mutations in the epidermal growth factor receptor and in KRAS are predictive and prognostic indicators in patients with non-small-cell lung cancer treated with chemotherapy alone and in combination with erlotinib." Journal of Clinical Oncology **23**(25): 5900-5909.
- El-Gendy, N. and C. Berkland (2009). "Combination Chemotherapeutic Dry Powder Aerosols via Controlled Nanoparticle Agglomeration." Pharmaceutical Research **26**(7): 1752-1763.
- El-Sherbiny, I. M. and H. D. C. Smyth (2010). "Novel cryomilled physically cross-linked biodegradable hydrogel microparticles as carriers for inhalation therapy." Journal of Microencapsulation **27**(8): 657-668.
- Elson, E. L. and D. Magde (1974). "Fluorescence Correlation Spectroscopy. 1. Conceptual Basis and Theory." Biopolymers **13**(1): 1-27.
- Estrella, V., T. Chen, M. Lloyd, J. Wojtkowiak, H. H. Cornnell, A. Ibrahim-Hashim, K. Bailey, Y. Balagurunathan, J. M. Rothberg, B. F. Sloane, J. Johnson, R. A. Gatenby and R. J. Gillies (2013). "Acidity Generated by the Tumor Microenvironment Drives Local Invasion." Cancer Research **73**(5): 1524-1535.
- Farhat, A., Y. Holloway, T. Jones, S. Taylor, S. Britland and D. Eagland (2009). "Towards improved pulmonary delivery of budesonide using a nebulisable nanoparticulate hydrogel." Journal of Pharmacy and Pharmacology **61**: A43-A44.
- Fathi, A. and J. Brahmer (2008). "Chemotherapy for Advanced Stage Non-Small Cell Lung Cancer." Seminars in thoracic and cardiovascular surgery **20**: 210-216.
- Ferlay, J., I. Soerjomataram, M. Ervik, R. Dikshit, S. Eser, C. Mathers, M. Rebelo, D. Parkin, D. Forman and F. Bray. (2013). "GLOBOCAN 2012 v1.0, Cancer Incidence and Mortality Worldwide: IARC CancerBase No. 11 [Internet]." Retrieved 6/30/14, 2014, from <http://globocan.iarc.fr>.
- Ferrari, M. (2005). "Cancer nanotechnology: Opportunities and challenges." Nature Reviews Cancer **5**(3): 161-171.

- Finlay, W. (2008). "The ARLA Respiratory Deposition Calculator." Retrieved 2008, from http://www.mece.ualberta.ca/arla/impactor_mmad_calculator.html.
- Frimpong, R. A., J. Dou, M. Pechan and J. Z. Hilt (2010). "Enhancing remote controlled heating characteristics in hydrophilic magnetite nanoparticles via facile co-precipitation." Journal of Magnetism and Magnetic Materials **322**(3): 326-331.
- Frimpong, R. A., S. Fraser and J. Z. Hilt (2007). "Synthesis and temperature response analysis of magnetic-hydrogel nanocomposites." Journal of Biomedical Materials Research Part A **80A**(1): 1-6.
- Frimpong, R. A. and J. Z. Hilt (2010). "Magnetic nanoparticles in biomedicine: synthesis, functionalization and applications." Nanomedicine **5**(9): 1401-1414.
- Fronczek, F. R., H. N. Kamel and M. Slattery (2003). "Three polymorphs (alpha, beta and delta) of D-mannitol at 100 K." Acta Crystallographica Section C-Crystal Structure Communications **59**: O567-O570.
- Galluzzi, L., M. C. Maiuri, I. Vitale, H. Zischka, M. Castedo, L. Zitvogel and G. Kroemer (2007). "Cell death modalities: classification and pathophysiological implications." Cell Death and Differentiation **14**(7): 1237-1243.
- Ganapathy, V., N. Gupta and R. Martindale (2006). Protein digestion and absorption. Physiology of the gastrointestinal tract, Burlington: Academic Press. **II**: 1667-1692.
- Gatzemeier, U., A. Pluzanska, A. Szczesna, E. Kaukel, J. Roubec, F. De Rosa, J. Milanowski, H. Karnicka-Mlodkowski, M. Pesek, P. Serwatowski, R. Ramlau, T. Janaskova, J. Vansteenkiste, J. Strausz, G. M. Manikhas and J. Von Pawel (2007). "Phase III study of erlotinib in combination with cisplatin and gemcitabine in advanced non-small-cell lung cancer: The Tarceva Lung Cancer Investigation Trial." Journal of Clinical Oncology **25**(12): 1545-1552.
- Gendron, P. O., F. Avaltroni and K. J. Wilkinson (2008). "Diffusion Coefficients of Several Rhodamine Derivatives as Determined by Pulsed Field Gradient-Nuclear Magnetic Resonance and Fluorescence Correlation Spectroscopy." Journal of Fluorescence **18**(6): 1093-1101.
- Gerratana, L., V. Fanotto, M. Bonotto, S. Bolzonello, A. M. Minisini, G. Fasola and F. Puglisi (2015). "Pattern of metastasis and outcome in patients with breast cancer." Clinical & Experimental Metastasis **32**(2): 125-133.
- Ghandehari, H., P. Kopeckova and J. Kopecek (1997). "In vitro degradation of pH-sensitive hydrogels containing aromatic azo bonds." Biomaterials **18**(12): 861-872.
- Gjoerup, J., O. Hilberg and E. Bendstrup (2012). "Inhaled mannitol in the treatment of non-cystic fibrosis bronchiectasis in adults." Respirology **17**(6): 927-932.

Gupta, P., K. Vermani and S. Garg (2002). "Hydrogels: from controlled release to pH-responsive drug delivery." Drug Discovery Today **7**(10): 569-579.

Hamidi, M., A. Azadi and P. Rafiei (2008). "Hydrogel nanoparticles in drug delivery." Advanced Drug Delivery Reviews **60**(15): 1638-1649.

Hao, R., R. J. Xing, Z. C. Xu, Y. L. Hou, S. Gao and S. H. Sun (2010). "Synthesis, Functionalization, and Biomedical Applications of Multifunctional Magnetic Nanoparticles." Advanced Materials **22**(25): 2729-2742.

Hasenpusch, G., J. Geiger, K. Wagner, O. Mykhaylyk, F. Wiekhorst, L. Trahms, A. Heidsieck, B. Gleich, C. Bergemann, M. K. Aneja and C. Rudolph (2012). "Magnetized Aerosols Comprising Superparamagnetic Iron Oxide Nanoparticles Improve Targeted Drug and Gene Delivery to the Lung." Pharmaceutical Research **29**(5): 1308-1318.

Hawkins, A. M., C. E. Bottom, Z. Liang, D. A. Puleo and J. Z. Hilt (2012). "Magnetic Nanocomposite Sol-Gel Systems for Remote Controlled Drug Release." Advanced Healthcare Materials **1**(1): 96-100.

Hawkins, A. M., D. A. Puleo and J. Z. Hilt (2011). "Effect of Macromer Synthesis Time on the Properties of the Resulting Poly(beta-amino ester) Degradable Hydrogel." Journal of Applied Polymer Science **122**(2): 1420-1426.

Hawkins, A. M., M. E. Tolbert, B. Newton, T. A. Milbrandt, D. A. Puleo and J. Z. Hilt (2013). "Tuning biodegradable hydrogel properties via synthesis procedure." Polymer **54**(17): 4422-4426.

He, H. N., A. David, B. Chertok, A. Cole, K. Lee, J. Zhang, J. X. Wang, Y. Z. Huang and V. C. Yang (2013). "Magnetic Nanoparticles for Tumor Imaging and Therapy: A So-Called Theranostic System." Pharmaceutical Research **30**(10): 2445-2458.

Health, N. I. o. (2015). "Estimates of Funding for Various Research, Condition, and Disease Categories (RCDC)." Retrieved 4/22/15, 2015, from http://report.nih.gov/categorical_spending.aspx.

Hess, S. T., S. Huang, A. A. Heikal and W. W. Webb (2002). "Biological and chemical applications of fluorescence correlation spectroscopy: a review." Biochemistry **41**(3): 697-705.

Hickey, A. J., H. M. Mansour, M. J. Telko, Z. Xu, H. D. C. Smyth, T. Mulder, R. McLean, J. Langridge and D. Papadopoulos (2007). "Physical characterization of component particles included in dry powder inhalers. I. Strategy review and static characteristics." Journal of Pharmaceutical Sciences **96**(5): 1282-1301.

- Hirte, H. W. (2013). "Profile of erlotinib and its potential in the treatment of advanced ovarian carcinoma." Oncotargets and Therapy **6**.
- Horsman, M. R. and J. Overgaard (2007). "Hyperthermia: a potent enhancer of radiotherapy." Clinical Oncology **19**(6): 418-426.
- Hudis, C. A. and L. Gianni (2011). "Triple-Negative Breast Cancer: An Unmet Medical Need." Oncologist **16**: 1-11.
- Iacono, D., R. Chiari, G. Metro, C. Bennati, G. Bellezza, M. Cenci, B. Ricciuti, A. Sidoni, S. Baglivo, V. Minotti and L. Crino (2015). "Future options for ALK-positive non-small cell lung cancer." Lung Cancer **87**(3): 211-219.
- Institute, N. C. (2015). "Non-Small Cell Lung Cancer Treatment (PDQ®)." Retrieved 4-21-15, 2015, from <http://www.cancer.gov/cancertopics/pdq/treatment/non-small-cell-lung/Patient>.
- Issels, R. D. (2008). "Hyperthermia adds to chemotherapy." European Journal of Cancer **44**(17): 2546-2554.
- Jackman, D. M., L. R. Chirieac and P. A. Janne (2005). "Bronchioloalveolar carcinoma: A review of the epidemiology, pathology, and treatment." Seminars in Respiratory and Critical Care Medicine **26**(3): 342-352.
- Johannsen, M., B. Thiesen, P. Wust and A. Jordan (2010). "Magnetic nanoparticle hyperthermia for prostate cancer." International Journal of Hyperthermia **26**(8): 790-795.
- Jordan, A., R. Scholz, K. Maier-Hauff, M. Johannsen, P. Wust, J. Nadobny, H. Schirra, H. Schmidt, S. Deger, S. Loening, W. Lanksch and R. Felix (2001). "Presentation of a new magnetic field therapy system for the treatment of human solid tumors with magnetic fluid hyperthermia." Journal of Magnetism and Magnetic Materials **225**(1-2): 118-126.
- Jordan, A., R. Scholz, K. Maier-Hauff, F. K. H. van Landeghem, N. Waldoefner, U. Teichgraeber, J. Pinkernelle, H. Bruhn, F. Neumann, B. Thiesen, A. von Deimling and R. Felix (2006). "The effect of thermotherapy using magnetic nanoparticles on rat malignant glioma." Journal of Neuro-Oncology **78**(1): 7-14.
- Jordan, A., R. Scholz, P. Wust, H. Fahling and R. Felix (1999). "Magnetic fluid hyperthermia (MFH): Cancer treatment with AC magnetic field induced excitation of biocompatible superparamagnetic nanoparticles." Journal of Magnetism and Magnetic Materials **201**: 413-419.
- Kanthala, S., S. Pallerla and S. Jois (2015). "Current and future targeted therapies for non-small-cell lung cancers with aberrant EGF receptors." Future Oncology **11**(5): 865-878.

- Kassam, F., K. Enright, R. Dent, G. Dranitsaris, J. Myers, C. Flynn, M. Fralick, R. Kumar and M. Clemons (2009). "Survival Outcomes for Patients with Metastatic Triple-Negative Breast Cancer: Implications for Clinical Practice and Trial Design." Clinical Breast Cancer **9**(1): 29-33.
- Kau, P., G. M. Nagaraja, H. Zheng, D. Gizachew, M. Galukande, S. Krishnan and A. Asea (2012). "A mouse model for triple-negative breast cancer tumor-initiating cells (TNBC-TICs) exhibits similar aggressive phenotype to the human disease." Bmc Cancer **12**.
- Knecht, L. D., N. Ali, Y. N. Wei, J. Z. Hilt and S. Daunert (2012). "Nanoparticle-Mediated Remote Control of Enzymatic Activity." Acs Nano **6**(10): 9079-9086.
- Kondo, M. and S. Adachi (2013). "Optical Properties of NaCl:Sn²⁺ Phosphor Synthesized from Aqueous NaCl/SnCl₂/HCl Solution." Ecs Journal of Solid State Science and Technology **2**(1): R9-R15.
- Kopecek, J. (2009). "Hydrogels: From Soft Contact Lenses and Implants to Self-Assembled Nanomaterials." Journal of Polymer Science Part a-Polymer Chemistry **47**(22): 5929-5946.
- Kruse, A. M., S. A. Meenach, K. W. Anderson and J. Z. Hilt (2014). "Synthesis and characterization of CREKA-conjugated iron oxide nanoparticles for hyperthermia applications." Acta Biomaterialia **10**(6): 2622-2629.
- Kunz-Schughart, L. A., M. Kreutz and R. Knuechel (1998). "Multicellular spheroids: a three-dimensional in vitro culture system to study tumour biology." International Journal of Experimental Pathology **79**(1): 1-23.
- Kwon, J. T., D. S. Kim, A. Minai-Tehrani, S. K. Hwang, S. H. Chang, E. S. Lee, C. X. Xu, H. T. Lim, J. E. Kim, B. I. Yoon, G. H. An, K. H. Lee, J. K. Lee and M. H. Cho (2009). "Inhaled Fluorescent Magnetic Nanoparticles Induced Extramedullary Hematopoiesis in the Spleen of Mice." Journal of Occupational Health **51**(5): 423-431.
- Lai, S. K., D. E. O'Hanlon, S. Harrold, S. T. Man, Y. Y. Wang, R. Cone and J. Hanes (2007). "Rapid transport of large polymeric nanoparticles in fresh undiluted human mucus." Proceedings of the National Academy of Sciences of the United States of America **104**(5): 1482-1487.
- Lai, S. K., Y. Y. Wang and J. Hanes (2009). "Mucus-penetrating nanoparticles for drug and gene delivery to mucosal tissues." Advanced Drug Delivery Reviews **61**(2): 158-171.
- Lai, S. K., Y. Y. Wang, D. Wirtz and J. Hanes (2009). "Micro- and macrorheology of mucus." Advanced Drug Delivery Reviews **61**(2): 86-100.
- Lee, J., C. Lee, T. H. Kim, E. S. Lee, B. S. Shin, S. C. Chi, E. S. Park, K. C. Lee and Y. S. Youn (2012). "Self-assembled glycol chitosan nanogels containing palmityl-acylated

exendin-4 peptide as a long-acting anti-diabetic inhalation system." Journal of Controlled Release **161**(3): 728-734.

Li, L., T. L. M. ten Hagen, M. Hossann, R. Suss, G. C. van Rhoon, A. M. M. Eggermont, D. Haemmerich and G. A. Koning (2013). "Mild hyperthermia triggered doxorubicin release from optimized stealth thermosensitive liposomes improves intratumoral drug delivery and efficacy." Journal of Controlled Release **168**(2): 142-150.

Li, T. H., H. J. Kung, P. C. Mack and D. R. Gandara (2013). "Genotyping and Genomic Profiling of Non-Small-Cell Lung Cancer: Implications for Current and Future Therapies." Journal of Clinical Oncology **31**(8): 1039-1049.

Li, X. J. and H. M. Mansour (2011). "Physicochemical Characterization and Water Vapor Sorption of Organic Solution Advanced Spray-Dried Inhalable Trehalose Microparticles and Nanoparticles for Targeted Dry Powder Pulmonary Inhalation Delivery." Aaps Pharmscitech **12**(4): 1420-1430.

Li, Z. H., R. J. Zhao, X. H. Wu, Y. Sun, M. Yao, J. J. Li, Y. H. Xu and J. R. Gu (2005). "Identification and characterization of a novel peptide ligand of epidermal growth factor receptor for targeted delivery of therapeutics." Faseb Journal **19**(14): 1978-1985.

Littringer, E. M., A. Mescher, H. Schroettner, L. Achelis, P. Walzel and N. A. Urbanetz (2012). "Spray dried mannitol carrier particles with tailored surface properties - The influence of carrier surface roughness and shape." European Journal of Pharmaceutics and Biopharmaceutics **82**(1): 194-204.

Littringer, E. M., M. F. Noisternig, A. Mescher, H. Schroettner, P. Walzel, U. J. Griesser and N. A. Urbanetz (2013). "The morphology and various densities of spray dried mannitol." Powder Technology **246**: 193-200.

Liu, S. Q. and Z. Y. Tang (2010). "Nanoparticle assemblies for biological and chemical sensing." Journal of Materials Chemistry **20**(1): 24-35.

Lubner, M. G., C. L. Brace, J. L. Hinshaw and F. T. Lee (2010). "Microwave Tumor Ablation: Mechanism of Action, Clinical Results, and Devices." Journal of Vascular and Interventional Radiology **21**(8): S192-S203.

Mahmoudi, M., S. Sant, B. Wang, S. Laurent and T. Sen (2011). "Superparamagnetic iron oxide nanoparticles (SPIONs): Development, surface modification and applications in chemotherapy." Advanced Drug Delivery Reviews **63**(1-2): 24-46.

Mansour, H. M., Y. S. Rhee and X. A. Wu (2009). "Nanomedicine in pulmonary delivery." International Journal of Nanomedicine **4**: 299-319.

Mar, N., J. J. Vredenburgh and J. S. Wasser (2015). "Targeting HER2 in the treatment of non-small cell lung cancer." Lung Cancer **87**(3): 220-225.

- Martin, A. R. and W. H. Finlay (2008). "Magnetic Alignment of Aerosol Particles for Targeted Pulmonary Drug Delivery: Comparison of Magnetic and Aerodynamic Torques." Journal of Computational and Theoretical Nanoscience **5**(10): 2067-2070.
- Mazzone, P. and T. Mekhail (2012). "Current and emerging medical treatments for non-small cell lung cancer: A primer for pulmonologists." Respiratory Medicine **106**(4): 473-492.
- McBride, A. A., D. N. Price, L. R. Lamoureux, A. A. Elmaoued, J. M. Vargas, N. L. Adolphi and P. Muttill (2013). "Preparation and Characterization of Novel Magnetic Nano-in-Microparticles for Site-Specific Pulmonary Drug Delivery." Molecular Pharmaceutics **10**(10): 3574-3581.
- McGill, S. L., C. L. Cuylear, N. L. Adolphi, M. Osinski and H. D. C. Smyth (2009). "Magnetically Responsive Nanoparticles for Drug Delivery Applications Using Low Magnetic Field Strengths." Ieee Transactions on Nanobioscience **8**(1): 33-42.
- Meenach, S. A., A. A. Anderson, M. Suthar, K. W. Anderson and J. Z. Hilt (2009). "Biocompatibility analysis of magnetic hydrogel nanocomposites based on poly(N-isopropylacrylamide) and iron oxide." Journal of Biomedical Materials Research Part A **91A**(3): 903-909.
- Meenach, S. A., J. Z. Hilt and K. W. Anderson (2010). "Poly(ethylene glycol)-based magnetic hydrogel nanocomposites for hyperthermia cancer therapy." Acta Biomaterialia **6**(3): 1039-1046.
- Meenach, S. A., F. G. Vogt, K. W. Anderson, J. Z. Hilt, R. C. McGarry and H. M. Mansour (2013). "Design, Physicochemical Characterization, and Optimization of Organic Solution Advanced Spray-Dried Inhalable DPPC and DPPC:DPPE-PEG Microparticles and Nanoparticles for Targeted Respiratory Nanomedicine Delivery as Dry Powder Inhalation Aerosols." Internation Journal of Nanomedicine **8**: 275-293.
- Mellas, N., O. Elmesbahi, O. Masbah and H. Errihani (2010). "Neoadjuvant chemotherapy in non-small cell lung cancer: current state and future." Bulletin Du Cancer **97**(2): 211-223.
- Mobus, K., J. Siepmann and R. Bodmeier (2012). "Zinc-alginate microparticles for controlled pulmonary delivery of proteins prepared by spray-drying." European Journal of Pharmaceutics and Biopharmaceutics **81**(1): 121-130.
- Molina, J. R., P. G. Yang, S. D. Cassivi, S. E. Schild and A. A. Adjei (2008). "Non-small cell lung cancer: Epidemiology, risk factors, treatment, and survivorship." Mayo Clinic Proceedings **83**(5): 584-594.

- Mosbach, K. and U. Schroder (1979). "PREPARATION AND APPLICATION OF MAGNETIC POLYMERS FOR TARGETING OF DRUGS." Febs Letters **102**(1): 112-116.
- Muller, G. (2011). "Oral Delivery of Protein Drugs: Driver for Personalized Medicine?" Current Issues in Molecular Biology **13**: 13-24.
- Nahar, K., S. Absar, B. Patel and F. Ahsan (2014). "Starch-coated magnetic liposomes as an inhalable carrier for accumulation of fasudil in the pulmonary vasculature." International Journal of Pharmaceutics **464**(1-2): 185-195.
- Oakes, J. M., M. Scadeng, E. C. Breen, G. K. Prisk and C. Darquenne (2013). "Regional Distribution of Aerosol Deposition in Rat Lungs Using Magnetic Resonance Imaging." Annals of Biomedical Engineering **41**(5): 967-978.
- Odziomek, M., T. R. Sosnowski and L. Gradon (2012). "Conception, preparation and properties of functional carrier particles for pulmonary drug delivery." International Journal of Pharmaceutics **433**(1-2): 51-59.
- Oh, J. K., R. Drumright, D. J. Siegwart and K. Matyjaszewski (2008). "The development of microgels/nanogels for drug delivery applications." Progress in Polymer Science **33**(4): 448-477.
- Ohguri, T., H. Imada, K. Yahara, S. D. Moon, S. Yamaguchi, K. Yatera, H. Mukae, T. Hanagiri, F. Tanaka and Y. Korogi (2012). "Re-irradiation plus regional hyperthermia for recurrent non-small cell lung cancer: A potential modality for inducing long-term survival in selected patients." Lung Cancer **77**(1): 140-145.
- Olmsted, S. S., J. L. Padgett, A. I. Yudin, K. J. Whaley, T. R. Moench and R. A. Cone (2001). "Diffusion of macromolecules and virus-like particles in human cervical mucus." Biophysical Journal **81**(4): 1930-1937.
- Otterson, G. A., M. A. Villalona-Calero, W. Hicks, X. L. Pan, J. A. Ellerton, S. N. Gettinger and J. R. Murren (2010). "Phase I/II Study of Inhaled Doxorubicin Combined with Platinum-Based Therapy for Advanced Non-Small Cell Lung Cancer." Clinical Cancer Research **16**(8): 2466-2473.
- Otterson, G. A., M. A. Villalona-Calero, S. Sharma, M. G. Kris, A. Imondi, M. Gerber, D. A. White, M. J. Ratain, J. H. Schiller, A. Sandler, M. Kraut, S. Mani and J. R. Murren (2007). "Phase I study of inhaled doxorubicin for patients with metastatic tumors to the lungs." Clinical Cancer Research **13**(4): 1246-1252.
- Oxnard, G. R., A. Binder and P. A. Janne (2013). "New Targetable Oncogenes in Non-Small-Cell Lung Cancer." Journal of Clinical Oncology **31**(8): 1097-1104.

- Pankhurst, Q. A., J. Connolly, S. K. Jones and J. Dobson (2003). "Applications of magnetic nanoparticles in biomedicine." Journal of Physics D-Applied Physics **36**(13): R167-R181.
- Pao, W. and N. Girard (2011). "New driver mutations in non-small-cell lung cancer." Lancet Oncology **12**(2): 175-180.
- Patton, J. S. and P. R. Byron (2007). "Inhaling medicines: delivering drugs to the body through the lungs." Nature Reviews Drug Discovery **6**(1): 67-74.
- Peer, D., J. M. Karp, S. Hong, O. C. FaroKhzad, R. Margalit and R. Langer (2007). "Nanocarriers as an emerging platform for cancer therapy." Nature Nanotechnology **2**(12): 751-760.
- Pena, M. A., Y. Daali, J. Barra and P. Bustamante (2000). "Partial solubility parameters of lactose, mannitol and saccharose using the modified extended Hansen method and evaporation light scattering detection." Chemical & Pharmaceutical Bulletin **48**(2): 179-183.
- Peppas, N. A., P. Bures, W. Leobandung and H. Ichikawa (2000). "Hydrogels in pharmaceutical formulations." European Journal of Pharmaceutics and Biopharmaceutics **50**(1): 27-46.
- Peppas, N. A., J. Z. Hilt, A. Khademhosseini and R. Langer (2006). "Hydrogels in biology and medicine: From molecular principles to bionanotechnology." Advanced Materials **18**(11): 1345-1360.
- Peppas, N. A., K. B. Keys, M. Torres-Lugo and A. M. Lowman (1999). "Poly(ethylene glycol)-containing hydrogels in drug delivery." Journal of Controlled Release **62**(1-2): 81-87.
- Pisters, K. M. W., W. K. Evans, C. G. Azzoli, M. G. Kris, C. A. Smith, C. E. Desch, M. R. Somerfield, M. C. Brouwers, G. Darling, P. M. Ellis, L. E. Gaspar, H. I. Pass, D. R. Spiegel, J. R. Strawn, Y. C. Ung and F. A. Shepherd (2007). "Cancer care Ontario and American society of clinical oncology adjuvant chemotherapy and adjuvant radiation therapy for stages I-IIIa resectable non-small-cell lung cancer guideline." Journal of Clinical Oncology **25**(34): 5506-5518.
- Ragab, D. M. and S. Rohani (2013). "Cubic Magnetically Guided Nanoaggregates for Inhalable Drug Delivery: In Vitro Magnetic Aerosol Deposition Study." Aaps Pharmscitech **14**(3): 977-993.
- Ragab, D. M., S. Rohani and S. Consta (2012). "Controlled release of 5-fluorouracil and progesterone from magnetic nanoaggregates." International Journal of Nanomedicine **7**: 3167-3189.

Rahimpour, Y., M. Kouhsoltani and H. Hamishehkar (2014). "Alternative carriers in dry powder inhaler formulations." Drug Discovery Today **19**(5): 618-626.

Ranaldi, G., I. Marigliano, I. Vespignani, G. Perozzi and Y. Sambuy (2002). "The effect of chitosan and other polycations on tight junction permeability in the human intestinal Caco-2 cell line." Journal of Nutritional Biochemistry **13**(3): 157-167.

Reddy, L. H., J. L. Arias, J. Nicolas and P. Couvreur (2012). "Magnetic Nanoparticles: Design and Characterization, Toxicity and Biocompatibility, Pharmaceutical and Biomedical Applications." Chemical Reviews **112**(11): 5818-5878.

Redman, G. E. S., A. R. Martin, P. Waszak, R. B. Thompson, P. Y. Cheung, B. Thebaud and W. H. Finlay (2011). "Pilot Study of Inhaled Aerosols Targeted via Magnetic Alignment of High Aspect Ratio Particles in Rabbits." Journal of Nanomaterials: 7.

Robinson, L. A., J. C. Ruckdeschel, H. Wagner and C. W. Stevens (2007). "Treatment of non-small cell lung cancer-stage IIIA - ACCP evidence-based clinical practice guidelines (2nd edition)." Chest **132**(3): 243S-265S.

Rosell, R., E. Carcereny, R. Gervais, A. Vergnenegre, B. Massuti, E. Felip, R. Palmero, R. Garcia-Gomez, C. Pallares, J. M. Sanchez, R. Porta, M. Cobo, P. Garrido, F. Longo, T. Moran, A. Insa, F. De Marinis, R. Corre, I. Bover, A. Illiano, E. Dansin, J. de Castro, M. Milella, N. Reguart, G. Altavilla, U. Jimenez, M. Provencio, M. A. Moreno, J. Terrasa, J. Munoz-Langa, J. Valdivia, D. Isla, M. Domine, O. Molinier, J. Mazieres, N. Baize, R. Garcia-Campelo, G. Robinet, D. Rodriguez-Abreu, G. Lopez-Vivanco, V. Gebbia, L. Ferrera-Delgado, P. Bombaron, R. Bernabe, A. Bearz, A. Artal, E. Cortesi, C. Rolfo, M. Sanchez-Ronco, A. Drozdowskyj, C. Queralt, I. de Aguirre, J. L. Ramirez, J. J. Sanchez, M. A. Molina, M. Taron, L. Paz-Ares, P. Grp Francais and T. Assoc Italiana Oncologia (2012). "Erlotinib versus standard chemotherapy as first-line treatment for European patients with advanced EGFR mutation-positive non-small-cell lung cancer (EURTAC): a multicentre, open-label, randomised phase 3 trial." Lancet Oncology **13**(3): 239-246.

Rosenberg, B. (1985). "FUNDAMENTAL-STUDIES WITH CISPLATIN." Cancer **55**(10): 2303-2316.

Rosiak, J. M. and F. Yoshii (1999). "Hydrogels and their medical applications." Nuclear Instruments & Methods in Physics Research Section B-Beam Interactions with Materials and Atoms **151**(1-4): 56-64.

Sadhukha, T., T. S. Wiedmann and J. Panyam (2013). "Inhalable magnetic nanoparticles for targeted hyperthermia in lung cancer therapy." Biomaterials **34**(21): 5163-5171.

Sahlin, J. J. and N. A. Peppas (1997). "Enhanced hydrogel adhesion by polymer interdiffusion: Use of linear poly(ethylene glycol) as an adhesion promoter." Journal of Biomaterials Science-Polymer Edition **8**(6): 421-436.

- Satarkar, N. S., D. Biswal and J. Z. Hilt (2010). "Hydrogel nanocomposites: a review of applications as remote controlled biomaterials." Soft Matter **6**(11): 2364-2371.
- Satarkar, N. S. and J. Z. Hilt (2008). "Hydrogel nanocomposites as remote-controlled biomaterials." Acta Biomaterialia **4**(1): 11-16.
- Satarkar, N. S. and J. Z. Hilt (2008). "Magnetic hydrogel nanocomposites for remote controlled pulsatile drug release." Journal of Controlled Release **130**(3): 246-251.
- Satarkar, N. S., S. A. Meenach, K. W. Anderson and J. Z. Hilt (2011). "Remote Actuation of Hydrogel Nanocomposites: Heating Analysis, Modeling, and Simulations." Aiche Journal **57**(4): 852-860.
- Scott, W. J., J. Howington, S. Feigenberg, B. Movsas and K. Pisters (2007). "Treatment of non-small cell lung cancer stage I and stage II - ACCP evidence-based clinical practice guidelines (2nd edition)." Chest **132**(3): 234S-242S.
- Secret, E., S. J. Kelly, K. E. Crannell and J. S. Andrew (2014). "Enzyme-Responsive Hydrogel Microparticles for Pulmonary Drug Delivery." Acs Applied Materials & Interfaces **6**(13): 10313-10321.
- Selvam, P., I. M. El-Sherbiny and H. D. C. Smyth (2011). "Swellable Hydrogel Particles for Controlled Release Pulmonary Administration Using Propellant-Driven Metered Dose Inhalers." Journal of Aerosol Medicine and Pulmonary Drug Delivery **24**(1): 25-34.
- Sheehan, J. K., S. Kirkham, M. Howard, P. Woodman, S. Kutay, C. Brazeau, J. Buckley and D. J. Thornton (2004). "Identification of molecular intermediates in the assembly pathway of the MUC5AC mucin." Journal of Biological Chemistry **279**(15): 15698-15705.
- Shen, Z. G., W. H. Chen, N. Jugade, L. Y. Gao, W. Glover, J. Y. Shen, J. Yun and J. F. Chen (2012). "Fabrication of inhalable spore like pharmaceutical particles for deep lung deposition." International Journal of Pharmaceutics **430**(1-2): 98-103.
- Shepherd, F. A., J. R. Pereira, T. Ciuleanu, E. H. Tan, V. Hirsh, S. Thongprasert, D. Campos, S. Maoleekoonpiroj, M. Smylie, R. Martins, M. van Kooten, M. Dediu, B. Findlay, D. S. Tu, D. Johnston, A. Bezjak, G. Clark, P. Santabarbara, L. Seymour and T. Natl Canc Inst Canada Clin (2005). "Erlotinib in previously treated non-small-cell lung cancer." New England Journal of Medicine **353**(2): 123-132.
- Siegel, R., D. Naishadham and A. Jemal (2012). "Cancer Statistics, 2012." Ca-a Cancer Journal for Clinicians **62**(1): 10-29.
- Silva, A. K. A., E. L. Silva, A. S. Carrico and E. S. T. Egito (2007). "Magnetic carriers: A promising device for targeting drugs into the human body." Current Pharmaceutical Design **13**(11): 1179-1185.

- Smith, J. (2005). "Erlotinib: Small-molecule targeted therapy in the treatment of non-small-cell lung cancer." Clinical Therapeutics **27**(10): 1513-1534.
- Son, Y. J. and J. T. McConville (2008). "Advancements in dry powder delivery to the lung." Drug Development and Industrial Pharmacy **34**(9): 948-959.
- Sonaje, K., K. J. Lin, J. J. Wang, F. L. Mi, C. T. Chen, J. H. Juang and H. W. Sung (2010). "Self-Assembled pH-Sensitive Nanoparticles: A Platform for Oral Delivery of Protein Drugs." Advanced Functional Materials **20**(21): 3695-3700.
- Sonaje, K., Y. H. Lin, J. H. Juang, S. P. Wey, C. T. Chen and H. W. Sung (2009). "In vivo evaluation of safety and efficacy of self-assembled nanoparticles for oral insulin delivery." Biomaterials **30**(12): 2329-2339.
- Soppimath, K. S., T. M. Aminabhavi, A. M. Dave, S. G. Kumbar and W. E. Rudzinski (2002). "Stimulus-responsive "smart" hydrogels as novel drug delivery systems." Drug Development and Industrial Pharmacy **28**(8): 957-974.
- Srinivas, A., P. J. Rao, G. Selvam, A. Goparaju, P. B. Murthy and P. N. Reddy (2012). "Oxidative stress and inflammatory responses of rat following acute inhalation exposure to iron oxide nanoparticles." Human & Experimental Toxicology **31**(11): 1113-1131.
- Stein, A., J. P. Whitlock and M. Bina (1979). "ACIDIC POLYPEPTIDES CAN ASSEMBLE BOTH HISTONES AND CHROMATIN INVITRO AT PHYSIOLOGICAL IONIC-STRENGTH." Proceedings of the National Academy of Sciences of the United States of America **76**(10): 5000-5004.
- Stocke, N. A., S. A. Meenach, S. M. Arnold, H. M. Mansour and J. Z. Hilt (2014). "Formulation and characterization of inhalable magnetic nanocomposite microparticles (MnMs) for targeted pulmonary delivery via spray drying." Int J Pharm **479**(2): 320-328.
- Stocke, N. A., S. A. Meenach, S. M. Arnold, H. M. Mansour and J. Z. Hilt (2015). "Formulation and characterization of inhalable magnetic nanocomposite microparticles (MnMs) for targeted pulmonary delivery via spray drying." Int J Pharm **479**(2): 320-328.
- Stocke, N. A., S. A. Meenach, S. M. Arnold, H. M. Mansour and J. Z. Hilt (2015). "Formulation and characterization of inhalable magnetic nanocomposite microparticles (MnMs) for targeted pulmonary delivery via spray drying." International Journal of Pharmaceutics **479**(2): 320-328.
- Suarez, S. and A. J. Hickey (2000). "Drug properties affecting aerosol behavior." Respir Care **45**(6): 652-666.
- Szalay, B., E. Tatrai, G. Nyiro, T. Vezer and G. Dura (2012). "Potential toxic effects of iron oxide nanoparticles in in vivo and in vitro experiments." Journal of Applied Toxicology **32**(6): 446-453.

- Tannock, I. F. and D. Rotin (1989). "ACID PH IN TUMORS AND ITS POTENTIAL FOR THERAPEUTIC EXPLOITATION." Cancer Research **49**(16): 4373-4384.
- Tewes, F., C. Ehrhardt and A. M. Healy (2014). "Superparamagnetic iron oxide nanoparticles (SPIONs)-loaded Trojan microparticles for targeted aerosol delivery to the lung." European Journal of Pharmaceutics and Biopharmaceutics **86**(1): 98-104.
- Thiesen, B. and A. Jordan (2008). "Clinical applications of magnetic nanoparticles for hyperthermia." International Journal of Hyperthermia **24**(6): 467-474.
- Timsina, M. P., G. P. Martin, C. Marriott, D. Ganderton and M. Yianneskis (1994). "DRUG-DELIVERY TO THE RESPIRATORY-TRACT USING DRY POWDER INHALERS." International Journal of Pharmaceutics **101**(1-2): 1-13.
- Todo, H., H. Okamoto, K. Iida and K. Danjo (2001). "Effect of additives on insulin absorption from intratracheally administered dry powders in rats." International Journal of Pharmaceutics **220**(1-2): 101-110.
- Tucker, Z. C. G., B. A. Laguna, E. Moon and S. Singhal (2012). "Adjuvant immunotherapy for non-small cell lung cancer." Cancer Treatment Reviews **38**(6): 650-661.
- Upreti, M., A. Jamshidi-Parsian, N. A. Koonce, J. S. Webber, S. K. Sharma, A. A. A. Asea, M. J. Mader and R. J. Griffin (2011). "Tumor-Endothelial Cell Three-dimensional Spheroids: New Aspects to Enhance Radiation and Drug Therapeutics." Translational Oncology **4**(6): 365-U138.
- Valeriete, F. and H. Lin (1975). "SYNERGISTIC INTERACTION OF ANTICANCER AGENTS - CELLULAR PERSPECTIVE." Cancer Chemotherapy Reports Part 1 **59**(5): 895-900.
- Vanbever, R., J. D. Mintzes, J. Wang, J. Nice, D. H. Chen, R. Batycky, R. Langer and D. A. Edwards (1999). "Formulation and physical characterization of large porous particles for inhalation." Pharmaceutical Research **16**(11): 1735-1742.
- Vaughn, J. M., J. T. McConville, D. Burgess, J. I. Peters, K. P. Johnston, R. L. Talbert and R. O. Williams (2006). "Single dose and multiple dose studies of itraconazole nanoparticles." European Journal of Pharmaceutics and Biopharmaceutics **63**(2): 95-102.
- Vehring, R. (2008). "Pharmaceutical particle engineering via spray drying." Pharmaceutical Research **25**(5): 999-1022.
- Verma, N. K., K. Crosbie-Staunton, A. Satti, S. Gallagher, K. B. Ryan, T. Doody, C. McAtamney, R. MacLoughlin, P. Galvin, C. S. Burke, Y. Volkov and Y. K. Gun'ko (2013). "Magnetic core-shell nanoparticles for drug delivery by nebulization." Journal of Nanobiotechnology **11**: 12.

Vernon, C. C., J. W. Hand, S. B. Field, D. Machin, J. B. Whaley, J. vanderZee, W. L. J. vanPutten, G. C. vanRhoon, J. D. P. vanDijk, D. G. Gonzalez, F. F. Liu, P. Goodman and M. Sherar (1996). "Radiotherapy with or without hyperthermia in the treatment of superficial localized breast cancer: Results from five randomized controlled trials." International Journal of Radiation Oncology Biology Physics **35**(4): 731-744.

Vertrees, R. A., A. Leeth, M. Girouard, J. D. Roach and J. B. Zwischenberger (2002). "Whole-body hyperthermia: a review of theory, design and application." Perfusion-Uk **17**(4): 279-290.

Wada, A. and H. Nakamura (1981). "NATURE OF THE CHARGE-DISTRIBUTION IN PROTEINS." Nature **293**(5835): 757-758.

Wagner, P. L., N. Kitabayashi, Y. T. Chen and A. Saqi (2009). "Combined Small Cell Lung Carcinomas Genotypic and Immunophenotypic Analysis of the Separate Morphologic Components." American Journal of Clinical Pathology **131**(3): 376-382.

Wallace, A. S., M. Arya, S. R. Frazier, S. Westgate, Z. Y. Wang and D. Doll (2014). "Combined small-cell lung carcinoma: An institutional experience." Thoracic Cancer **5**(1): 57-62.

Wang, Y. Y., S. K. Lai, J. S. Suk, A. Pace, R. Cone and J. Hanes (2008). "Addressing the PEG Mucoadhesivity Paradox to Engineer Nanoparticles that "Slip" through the Human Mucus Barrier." Angewandte Chemie-International Edition **47**(50): 9726-9729.

Widder, K. J. and A. E. Senyei (1983). "MAGNETIC MICROSPHERES - A VEHICLE FOR SELECTIVE TARGETING OF DRUGS." Pharmacology & Therapeutics **20**(3): 377-395.

Wittgen, B. P. H., P. W. A. Kunst, K. van der Born, A. W. van Wijk, W. Perkins, F. G. Pilkiewicz, R. Perez-Soler, S. Nicholson, G. J. Peters and P. E. Postmus (2007). "Phase I study of aerosolized SLIT cisplatin in the treatment of patients with carcinoma of the lung." Clinical Cancer Research **13**(8): 2414-2421.

Wu, X., W. Zhang, D. J. Hayes and H. M. Mansour (2013). "Physicochemical Characterization and Aerosol Dispersion Performance of Organic Solution Advanced Spray-Dried Cyclosporine A Multifunctional Particles for Dry Powder Inhalation Aerosol Delivery." International Journal of Nanomedicine **8**: 1-15.

Wust, P., B. Hildebrandt, G. Sreenivasa, B. Rau, J. Gellermann, H. Riess, R. Felix and P. M. Schlag (2002). "Hyperthermia in combined treatment of cancer." Lancet Oncology **3**(8): 487-497.

Wydra, R. J., A. M. Kruse, Y. Bae, K. W. Anderson and J. Z. Hilt (2013). "Synthesis and characterization of PEG-iron oxide core-shell composite nanoparticles for thermal

therapy." Materials Science & Engineering C-Materials for Biological Applications **33**(8): 4660-4666.

Xie, Y. Y., P. Y. Zeng, R. A. Siegel, T. S. Wiedmann, B. E. Hammer and P. W. Longest (2010). "Magnetic Deposition of Aerosols Composed of Aggregated Superparamagnetic Nanoparticles." Pharmaceutical Research **27**(5): 855-865.

Xu, Y., A. Karmakar, W. E. Heberlein, T. Mustafa, A. R. Biris and A. S. Biris (2012). "Multifunctional Magnetic Nanoparticles for Synergistic Enhancement of Cancer Treatment by Combinatorial Radio Frequency Thermolysis and Drug Delivery." Advanced Healthcare Materials **1**(4): 493-501.

Xu, Z., H. M. Mansour, T. Mulder, R. McLean, J. Langridge and A. J. Hickey (2010). "Dry Powder Aerosols Generated by Standardized Entrainment Tubes From Drug Blends With Lactose Monohydrate: 1. Albuterol Sulfate and Disodium Cromoglycate." Journal of Pharmaceutical Sciences **99**(8): 3398-3414.

Yakacki, C. M., N. S. Satarkar, K. Gall, R. Likos and J. Z. Hilt (2009). "Shape-Memory Polymer Networks with Fe₃O₄ Nanoparticles for Remote Activation." Journal of Applied Polymer Science **112**(5): 3166-3176.

Yang, W., J. I. Peters and R. O. Williams (2008). "Inhaled nanoparticles - A current review." International Journal of Pharmaceutics **356**(1-2): 239-247.

Yu, S. A., A. Q. Luo, D. Biswal, J. Z. Hilt and D. A. Puleo (2010). "Lysozyme-imprinted polymer synthesized using UV free-radical polymerization." Talanta **83**(1): 156-161.

Zarogoulidis, K., P. Zarogoulidis, K. Darwiche, E. Boutsikou, N. Machairiotis, K. Tsakiridis, N. Katsikogiannis, I. Kougioumtzi, I. Karapantzos, H. D. Huang and D. Spyrtos (2013). "Treatment of non-small cell lung cancer (NSCLC)." Journal of Thoracic Disease **5**: S389-S396.

Zarogoulidis, P., E. Eleftheriadou, I. Sapardanis, V. Zarogoulidou, H. Lithoxopoulou, T. Kontakiotis, N. Karamanos, G. Zachariadis, M. Mabroudi, A. Zisimopoulos and K. Zarogoulidis (2012). "Feasibility and effectiveness of inhaled carboplatin in NSCLC patients." Investigational New Drugs **30**(4): 1628-1640.

Zhang, F. Y., N. T. Q. Ngoc, B. H. Tay, A. Mendyk, Y. H. Shao and R. Lau (2015). "Roughness-Controlled Self-Assembly of Mannitol/LB Agar Microparticles by Polymorphic Transformation for Pulmonary Drug Delivery." Molecular Pharmaceutics **12**(1): 223-231.

Vita

PERSONAL INFORMATION

Place of Birth: Owensboro, Kentucky, United States of America

EDUCATION

University of Kentucky, Lexington, Kentucky, May 2010

B.S. Chemical Engineering

RESEARCH EXPERIENCE

National Science Foundation IGERT Graduate Trainee

University of Kentucky, Lexington, KY, January 2010 – January 2013

Advisors: Dr. J. Z. Hilt, Chemical & Materials Engineering, Dr. Heidi M. Mansour
Pharmaceutical Sciences

National Institute of Health's National Cancer Institute CNTC Graduate Trainee

University of Kentucky, Lexington, KY, January 2013 – January 2015

Advisors: Dr. J. Z. Hilt, Chemical & Materials Engineering, Dr. Susanne Arnold, Internal
Medicine, Dr. Heidi M. Mansour Pharmaceutical Sciences

Undergraduate Research Assistant

University of Kentucky, Lexington, KY August 2008 – December 2008

Advisor: Dr. J. Z. Hilt, Chemical & Materials Engineering

Alltech Inc. Research Internship 05/10-08/10,

Alltech Inc., Nicholasville, KY May 2010 – August 2010

Supervisor: Alexandros Yiannikouris

Awards/Honors:

- NSF-IGERT Fellow (January 2013 – January 2015)
- NIH/NCI-CNTC Fellow (January 2013 – January 2015)
- 2014 GPEN Meeting, Helsinki, Finland, 1st Poster Presentation (August 2014)
- Markey Cancer Center Research Day, Lexington KY, 1st Place Poster Presentation (May 2013)
- Graduate Certificate in Bioactive Interfaces and Devices (December 2013)

Publications:

- Nathanael A. Stocke, Melissa Prado, Laura Codonnier, Thomas Dziubla, J. Zach Hilt, Glucose-Initiated Accelerated Degradation of Poly(Beta-Amino Ester) (PBAE) Biohybrid Hydrogels. In preparation for submission.
- Nathanael A. Stocke, Pallavi Sethi, Amar Jyoti, Susanne Arnold, J. Zach Hilt, Meenakshi Upreti, Remote controlled thermal therapy with magnetic nanocomposite microparticles induces cell death in triple negative breast cancer micrometastatic tumor tissue analogs. In preparation for submission.
- Nathanael A. Stocke, Xiaolu Zhang, J. Zach Hilt, Jason DeRouchey, Transport in PEG-Based Hydrogels: Role of Water Content and Crosslinker Molecular Weight, *Macromolecular Materials and Engineering* . Wiley, 2015. Submitted.
- Nathanael A. Stocke, Susanne Arnold, J. Zach Hilt, Responsive Hydrogel Nanoparticles for Pulmonary Delivery, *Journal of Drug Delivery Science and Technology*. Elsevier, 2015. Submitted.

- Nathanael A. Stocke, Shuo Tang, Marjorie Guy, Susanne Arnold, Heidi M. Mansour, J. Zach Hilt, Inhalable Anticancer Agents for Targeted Pulmonary Delivery and Lung Cancer Therapy, *Pharmaceutical Research*, 2015. Submitted.
- Nathanael A. Stocke, Samantha A. Meenach, Susanne Arnold, Heidi M. Mansour, J. Zach Hilt, Formulation and Characterization of Inhalable Magnetic Nanocomposite Microparticles (MnMs) for Targeted Pulmonary Delivery via Spray Drying, *International Journal of Pharmaceutics*, 479, 320-328, 2015.

Professional Conference Presentations (Poster/Oral):

- Nathanael A. Stocke, Samantha A. Meenach, Susanne Arnold, Heidi M. Mansour, J. Zach Hilt. Inhalable Nanocomposites for Lung Cancer Treatment. *2014 American Institute of Chemical Engineers Annual Meeting*, Atlanta, GA, November 16-21, 2013
- Nathanael A. Stocke, Samantha A. Meenach, Susanne Arnold, Heidi M. Mansour, J. Zach Hilt. Inhalable Nanocomposites for Lung Cancer Treatment. *2014 Globalization of Pharmaceutics Education Network (GPEN)*, Helsinki, Finland, August 27-30, 2014. **(Received first place poster presentation award).**
- Nathanael A. Stocke, Samantha A. Meenach, Susanne Arnold, Heidi M. Mansour, J. Zach Hilt. Inhalable Dry Powder Composites for Lung Cancer Treatment. *2014 Society For Biomaterials Annual Meeting*, Denver, CO, April 16-19, 2014
- Nathanael A. Stocke, Samantha A. Meenach, Susanne Arnold, Heidi M. Mansour, J. Zach Hilt. Inhalable Dry Powder Composites for Lung Cancer Treatment. *2013 American Institute of Chemical Engineers Annual Meeting*, San Francisco, CA, November 3-8, 2013
- Nathanael A. Stocke, Samantha A. Meenach, Susanne Arnold, Heidi M. Mansour, J. Zach Hilt. Formulation and Characterization of Inhalable Magnetic Nanocomposite Microparticles (MnMs). *2013 Annual Principle Investigators Meeting NCI Alliance for Nanotechnology in Cancer*, Bethesda, MD (NIH Headquarters), September 17-19, 2013
- Nathanael A. Stocke, Samantha A. Meenach, Susanne Arnold, Heidi M. Mansour, J. Zach Hilt. Formulation and Characterization of Inhalable Magnetic Nanocomposite Microparticles (MnMs). *2013 Controlled Release Society (CRS) Annual Meeting*, Honolulu, HI, July 21-24, 2013
- Nathanael A. Stocke, Samantha Meenach, Susanne Arnold, Heidi Mansour, J. Zach Hilt. Formulation and Characterization of Inhalable Magnetic Nanocomposite Microparticles

(MnMs). *2013 Markey Cancer Center Research Day*, Lexington, KY, May 22, 2013.
(Received first place poster presentation award).

- Nathanael A. Stocke, Samantha Meenach, Susanne Arnold, Heidi M. Mansour, J. Zach Hilt. Inhalable Magnetic Nanocomposite Microparticles for Lung Cancer. *2012 American Institute of Chemical Engineers Annual Meeting*, Pittsburgh, PA, October 28-November 2, 2012
- Nathanael A. Stocke, Xiaolu Zhang, Jason DeRouchey, Heidi M. Mansour, J. Zach Hilt. Probe Diffusion in PEG Hydrogels. *2012 American Institute of Chemical Engineers Annual Meeting*, Pittsburgh, PA, October 28-November 2, 2012
- Nathanael A. Stocke, Heidi M. Mansour, J. Zach Hilt. Enhanced Transport of PEG-based Nanocomposites in Artificial Mucus Barriers. *2011 American Institute of Chemical Engineers Annual Meeting*, Minneapolis, MN, October 16-21, 2011
- David Spencer, Ashley M. Hawkins, **Nathanael A. Stocke**, David A. Puleo, J. Zach Hilt. Multiple Macromer Hydrogels for Multiphase Drug Release. *2012 American Institute of Chemical Engineers Annual Meeting Undergraduate Poster Presentations*, Pittsburgh, PA, October 28-November 2, 2012
- Melissa Prado, **Nathanael A. Stocke**, J. Zach Hilt. Glucose-initiated Accelerated Degradation of Poly(β -amino Ester) Hydrogels for Drug Delivery. *2013 American Institute of Chemical Engineers Annual Meeting Undergraduate Poster Presentations*, San Francisco, CA, November 4, 2013
- Shuo Tang, **Nathanael A. Stocke**, J. Zach Hilt. In Vitro Study of Inhalable Cisplatin and Erlotinib Nanocomposites for the Treatment of Lung Cancer. *2013 American Institute of Chemical Engineers Annual Meeting Undergraduate Poster Presentations*, San Francisco, CA, November 4, 2013
- Marjorie Guy, **Nathanael A. Stocke**, J. Zach Hilt. Formulation and Characterization of Inhalable Spray Dried Powders with Magnetic Nanoparticles and Anticancer Agents for Lung Cancer Treatment. *2014 NCUR National Conference on Undergraduate Research*, Lexington, KY, April 4, 2014
- Shuo Tang, **Nathanael A. Stocke**, J. Zach Hilt. In Vitro Study of Inhalable Anti-Tumor Nanocomposites for the Treatment of Lung Cancer. *2014 NCUR National Conference on Undergraduate Research*, Lexington, KY, April 4, 2014

Professional Organizations:

- American Institute of Chemical Engineers (AIChE)
- Society For Biomaterials (SFB)
- Vice President of the Great Lakes student chapter of the International Society for Pharmaceutical Engineers (ISPE) 08/09-12/09
- Member of Tau Beta Pi engineering honors fraternity (TBP)
- International Society For Pharmaceutical Engineering (ISPE)
- Omega Chi Epsilon chemical engineering honors fraternity (Ω XE)